Redox Reactions at Solid-Liquid Interfaces and Implications for Sustainability

By

Austin Henry Henke

A dissertation submitted in partial fulfillment of

the requirements for the degree of

Doctor of Philosophy

(Chemistry)

at the

UNIVERSITY OF WISCONSIN-MADISON

2021

Date of final oral examination: 05/13/2021

The dissertation is approved by the following members of the Final Oral Committee:
Robert J. Hamers, Professor, Chemistry
Joel A. Pedersen, Professor, Soil Science
Christy K. Remucal, Associate Professor, Civil and Environmental Engineering
Z. Vivian Feng, Associate Professor, Augsburg University, Chemistry

Redox Reactions at Solid-Liquid Interfaces and Implications for Sustainability

Austin Henry Henke

Under the Supervision of Professor Robert J. Hamers

University of Wisconsin-Madison

Abstract

Electron-transfer reactions at surfaces play important roles in numerous environmentally and technologically relevant processes, such as energy storage, catalysis, water purification, biochemical pathways, and mineral weathering. These diverse fields have in common that reduction-oxidation (redox) reactions between solid and liquid phases drive chemical transformations. Redox transformations at solid-liquid interfaces have potential for great societal benefit or environmental harm. Therefore, it is necessary to understand the mechanisms of these chemical reactions. In this thesis, I present two collaborative projects centered around this idea. The first is to understand the oxidation of water to generate hydroxyl radicals (·OH) on diamond surfaces for application in water purification, and to increase the efficiency of this reaction. The second is to understand the reciprocal redox transformations between small biomolecules NADH and glutathione with the nano-scale battery cathode material $LiCoO_2$ to assess the environmental toxicity of metal oxide nanomaterials.

Electrochemical formation of high-energy species such as hydroxyl radicals in aqueous media is inefficient because oxidation of H_2O to form O_2 is a more thermodynamically favorable reaction. Boron-doped diamond (BDD) is widely used as an electrode material for generating ·OH radicals because it has a very large kinetic overpotential for O_2 production, thus increasing electrochemical efficiency for ·OH production. Yet, the underlying mechanisms of O_2 and ·OH production at diamond electrodes are not well understood. We demonstrate that boron-doped diamond surfaces functionalized with a hydrophobic, polyfluorinated molecular ligands (PF-BDD) have significantly higher electrochemical efficiency for ·OH production compared with hydrogen-terminated (H-BDD), oxidized (O-BDD), or polyethylene ether-functionalized (E-BDD) boron-doped diamond samples. Our measurements show that ·OH production is nearly independent of surface functionalization and pH (pH = 7.4 vs. 9.2), indicating that ·OH is produced by oxidation of H_2O in an outer-sphere electron-transfer process. In contrast, the total electrochemical current, which primarily produces O_2, differs strongly between samples with different surface functionalization, indicating an inner-sphere electron-transfer process. X-ray photoelectron spectroscopy measurements show that while both H-BDD and PF-BDD electrodes are oxidized over time, PF-BDD showed longer stability (≈ 24 hr of use) than H-BDD. This work demonstrates that increasing surface hydrophobicity using perfluorinated ligands selectively inhibits inner-sphere oxidation to O_2 and therefore provides a pathway to increased efficiency for formation of ·OH via an outer-sphere process. The use of hydrophobic electrodes may be a general approach to increasing selectivity toward outer-sphere electron-transfer processes in aqueous media.

Among high-valence metal oxides, $LiCoO_2$ and related materials are of environmental importance because of the rapidly increasing use of these materials as cathodes in lithium ion batteries. Understanding the impact of these materials on aqueous environments relies on understanding their redox chemistry because Co release depends on oxidation state. Despite the critical role that redox chemistry plays in cellular homeostasis, the influence of specific biologically relevant electron transporters such as nicotinamide adenine dinucleotide (NADH) and glutathione (GSH) on the transformation of engineered nanoparticles has not been widely considered previously. Here we report an investigation of the interaction of $LiCoO_2$ nanoparticles with NADH and GSH. Measurements of Co release using inductively coupled plasma-mass spectrometry (ICP-MS) show that exposing $LiCoO_2$ nanoparticles to either NADH or GSH increases solubilization of cobalt, while corresponding spectroscopic measurements show that NADH is concurrently oxidized to NAD^+. To demonstrate that these effects are a consequence the high-valence Co(III) in $LiCoO_2$ nanoparticles, we performed control experiments using Co(II)-containing $Co(OH)_2$ and $LiCoPO_4$, and dissolved Co^{2+}/Li^+ ions. Additional experiments using molecules of similar structure to NADH and GSH, but that are not reducing agents, confirm that these transformations are driven by redox reactions and not by chelation effects. Our data show that interaction of $LiCoO_2$ with NADH and GSH induces release Co^{2+}

ions and alters the redox state of these biologically important transporters. Observation of NADH binding to $LiCoO_2$ using x-ray photoelectron spectroscopy (XPS) suggests a surface catalyzed reaction. The reciprocal reduction of $LiCoO_2$ to enable release of Co^{2+} and corresponding oxidation of NADH and GSH as model redox-active biomolecules has implications for understanding the biological impacts of high-valence metal oxide nanomaterials and the redox-driven weathering of such minerals.

Despite our work showing the reciprocal redox interaction of $LiCoO_2$ and NADH, the mechanism for such a reaction is not well understood. To investigate this further, we performed dissolution experiments with $LiCoO_2$ and control compounds exposed to NADH and several of its component molecules: ribose 5-phosphate ("Ribo") and 1-methylnicotinamide ("Nico"). We hypothesized that if phosphate was responsible for surface attachment, Ribo would reproduce the binding observed from NADH, and that if the nicotinamide group was responsible for redox reaction, Nico would reproduce the enhanced Co release seen with NADH. If both binding and reducing strength are needed in the same molecule to see an effect, these experiments would show that NADH alone reacts with $LiCoO_2$. Furthermore, we tested particles exposed to both Nico and Ribo to see if there were synergistic effects to recapture what is seen with NADH. Our surprising results show that Ribo, not Nico, replicates the enhancement of $LiCoO_2$ dissolution seen by NADH. This suggests that surface attachment via the phosphate group in NADH is critical to $LiCoO_2$ redox dissolution, and that reducing sugars must be considered when studying nanoparticle transformations in biological media. We also expanded NADH-exposure experiments to other metal oxides, such as Mn_2O_3 and NiO, and find that trends in metal oxidation state transfer to non-Co-containing compounds.

Acknowledgements

First, I want to thank my advisor, Bob Hamers. Thank you for being a great teacher and mentor. I have learned a lot as a graduate student, and much of this is thanks to you. I think one sign of a great advisor is that you always feel better coming from a meeting with them than before, which is the case with Bob. Through the struggles of graduate school, thank you for being understanding, supportive, and knowledgeable on whatever I might have questions about. Of course, some of it has to do with the other students (see below), but I think joining the Hamers group was one of my best graduate school decisions.

I also want to thank my other committee members, Joel Pedersen, Vivian Feng, and Christy Remucal, and previous committee member John Wright. To Joel, thank you for all our great interactions both on our work with "UW2020" and in the CSN. To Vivian, thank you for being such a bright (both intellectually and in personality) part of my graduate career and the CSN. To Christy, thank you for your help, teaching, and advice inside and outside of class. To John, thank you for serving on my committee for much of graduate school and having a great (and challenging) CHEM 621 class. There have been so many other great professors I have interacted with through classes and teaching, such as Kyoung-Shin Choi, Tim Bertram, and Silvia Cavagnero. Thank you!

Next, I want to thank all the amazing staff that have made this journey possible. Sue Martin and the other path coordinators, thanks for doing so much great work behind the scenes and truly caring for us graduate students. Steve Myers and the other machine shop staff, thanks for helping bring to life so many great (or crazy) device ideas. Tracy Drier, thanks for being awesome at what you do and fixing my glassware mistakes. Jeff Nielsen, thanks for keeping the building running through turbulent times, as we all know you are truly the pillar holding our labs up. To Rob McClain and Blaise Thompson, thanks for being great teachers and for all your help with instrumentation and electronics. To Jeanne Hamers, thank you for being a positive influence on my experience as a TA, as I am sure you are to many graduate and undergraduate students. To Chad Wilikinson, thank you for all your help both in teaching general chemistry and in developing our lab experiment. To Arrietta Clauss, thank you for your advice and help, and for being a true advocate for graduate students. To Pam Doolittle, Dominic Colosi, and Amanda Buchberger, thank you for all your help with using the ICP-MS and in teaching analytical chemistry. To Devin Wixon and others in the Delta Program, thank you for helping me to become a better teacher and mentor. Lastly, thank you to anyone else I haven not mentioned here, as there are so many great people in the purchasing department, loading-dock, copy center, information technology, and teaching staff that were essential for me to succeed.

Even though I often think graduate school as a job, the many great people in the Hamers group are not just coworkers, but friends. I want to sincerely thank each and every graduate student, undergraduate student, post-doc, etc. I have spent so much time with these past six years. We have had fun times inside and outside the Chem building. To Laura, Tim, and Kirsten, thank you for being early mentors and helping me in my first steps of research. To Curtis and Katie, thank you for working with me in experiments and having various chats in later steps of research. To Zack, Jaya, Liz, Sarah, and Kelly thank you for being great office-mates, friends, and collaborators, for helping me in my research numerous times, and for experiencing most of graduate school together. I also want to thank Sarah for her help in doing science outreach and developing our awesome lab experiment. To Jenny, thank you for being a leader and role model within our group (and just an all-around great person). To Mike, thank you for your advice, support, humor, effort, and overall

enthusiasm towards graduate students and their research: the Hamers group and the CSN are lucky to have you. Lastly, to all the undergraduates and high school students I have mentored, Riley, Kari, Devin, Alexa, and Jacob, thank you for working with me and I hope you have learned as much from me as I have learned from spending time with you.

To my family, thank you! Thank for always being there for me, whether we be near or far. Thank you to my parents for raising me to be the person I am today. Thank you to my brother, Alex, for being my closest friend growing up and someone I know I can count on. Even though I know I see you three and the rest of my family less now than when I was younger, you are all still just as important in my life. If not for a loving family, I do not know if I would be where I am today. So, while you may not have been in the lab with me, I do see you as investors in me: and here is part of the pay-off!

To my wonderful wife Katie (who is also a brilliant chemist, about to graduate with her PhD by the way): I could not have made it through this without you. Thank you so much for all you have done for me and how amazing a person you are. You are my best friend (obvi). You know better than anyone the trials we have been through in graduate school. When we met, we were star-crossed undergrads with hope. When we came to Madison, we were dating with a dream. When we inched closer to graduation, we got engaged. And now as we graduate, we are married with the world ahead of us. I look forward to celebrating our graduation milestones and exploring life with you. You don’t know until you know, but when you know, you know.

Table of Contents

Chapter 1. Background and Introduction

1.1 Electrochemistry, interfaces, and nanomaterials.

Countless recent technologies have been developed through understanding of electrochemical reactions at solid-liquid interfaces. This includes advances in energy storage,[1] energy conversion,[2] catalysis, chemical sensing,[3] and others. For example, Li ion batteries are a staple of the electronics industry and utilize the intercalation of Li ions from a Li anode, through an electrolyte, into a layered metal oxide cathode, such as $LiCoO_2$.[4] Research on electron transfer reactions is so often linked to solid-liquid interfaces both because solid surfaces allow for external power to drive unfavorable chemical reactions, and because the heterogeneity of interfaces yields surprising mechanisms that can be tuned in ways not possible in bulk solution. Solid-liquid interfaces at the atomic level often display properties vastly different from their bulk counterparts (Figure 1.1), such as shape, purity (i.e., defects), heterogeneity, interaction with light, defects, identity of chemical functional groups, and intermolecular forces between liquid and solid. This is because phase boundaries are never as “clean” as a macroscopic diagram may suggest, introducing heterogeneity and complications that can be seen as either problems or opportunities. Even diamond, one of the simplest (sp^3 hybridized C in tetrahedral coordination) and strongest known materials has an imperfect and heterogenous surface that makes it an exceedingly useful electrode material.[5]

Nanotechnology is another field tied to interfacial chemistry bursting with recent progress. Nanomaterials constitute any particle with at least one dimension less than 100 nm. On this scale, the proportion of surface atoms becomes significant, and the surface area of the material increases greatly. By their very nature, nanomaterials react and transform disproportionately at interfaces. Electron transfer reactions can come into play in nanomaterial dissolution, modification, catalysis, or by using nano- or micro-scale electrodes. Nanomaterials are also utilized in applications such as drug delivery[6] and imaging.[7] However, uncontrolled release of commercial nanomaterials poses a threat to the environment (see section 1.4). Before addressing this, it is necessary to describe an important class of molecules relevant to both projects in this thesis: reactive oxygen species.

1.2 Reactive oxygen species.

Most (electro)chemical reactions on earth occur in the presence of H_2O and/or O_2. Reactive oxygen species (ROS) are forms of oxygen other than $H_2O_{(l)}$ or $O_{2(g)}$ that are unstable and have inherent electron-transfer reactivity. Examples of ROS include hydroxyl radical (·OH), ozone (O_3), hydrogen peroxide (H_2O_2), and superoxide ($\cdot O_2^-$). Figure 1.2 shows a comparison of oxidizing strength for ROS in terms of standard reduction potential, as many of these molecules are strong oxidizing agents. ROS exist in every part of nature, from the atmosphere to bodies of water, and even living cells. Additionally, ROS may be generated through anthropogenic means, either intentionally for societal benefit, or unintentionally from pollution, etc. Because they are ubiquitous and have potential to initiate myriad chemical reactions, it is important to understand how they are produced and how they transform the molecules around them. This thesis primarily examines ·OH because it is the most powerful ROS (Figure 1.2), though others such as H_2O_2 are also relevant.

ROS are formed in the environment through various (photo)(bio)chemical processes and are relevant in gaseous and aqueous systems.[8] For an atmospheric example, one of the most important processes is the Chapman mechanism for generating stratospheric ozone.[9] In this process, a host of equilibria driven by the sun's UV radiation convert O_2, atomic O, O_3, and potentially even ·OH, between one another to generate the essential ozone layer. Additionally, photolytic production of ROS stands to be the dominant pathway for oxidative degradation of many molecules in the atmosphere.[10, 11] In natural waters, ROS can be generated via photolysis, catalytic reaction of minerals, or biochemical processes. For example, NO_3^- (Eq. 1.1) or NO_2^- (Eq 1.2-1.3) from soil and minerals can produce ·OH via photolysis in surface waters:[12]

$$NO_3^- + h\nu + H^+ \rightarrow \cdot OH + \cdot NO_2 \tag{1.1}$$

$$NO_2^- + h\nu \rightarrow NO\cdot + \cdot O^- \tag{1.2}$$

$$\cdot O^- + H_2O \rightarrow \cdot OH + {}^-OH \tag{1.3}$$

Additionally, Fe(II) and other metals can catalyze the generation of OH through the Haber-Weiss mechanism (Eq. 1.4-1.8),[13] discovered by Fenton over 100 years ago. See Gligorovski et al. for a quality review of ·OH generation in the environment.[12] Lastly, within biology, healthy and diseased cells generate ROS, in response to various stimuli, which for the most part are beyond the scope of this thesis.[14]

$$\mathrm{Fe(II)} + H_2O_2 \rightarrow \mathrm{Fe(III)} + {}^{-}OH + \cdot OH \tag{1.4}$$

$$\mathrm{Fe(II)} + \cdot OH \rightarrow \mathrm{Fe(III)} + {}^{-}OH \tag{1.5}$$

$$H_2O_2 + \cdot OH \rightarrow HO_2\cdot + H_2O \tag{1.6}$$

$$\mathrm{Fe(III)} + {}^{-}OH + HO_2\cdot \rightarrow \mathrm{Fe(II)} + O_2 + H_2O \tag{1.7}$$

$$\mathrm{Fe(III)} + H_2O_2 \rightarrow \mathrm{Fe(II)} + HO_2\cdot + H^+ \tag{1.8}$$

What happens to ROS after they have been generated? All ROS, especially ·OH, are not thermodynamically favored under standard conditions and will react or decompose. Hydroxyl radical is so reactive that concentrations of surrounding species and reaction kinetics influence the fate of ·OH much more than the respective equilibrium constants. For example, rate constants for ·OH with many organic molecules or inorganic compounds are so high they are diffusion limited,[15] meaning ·OH will react with whichever molecule it reaches first. If the nearest molecule is part of a living cell, it initiates various deleterious effects such as DNA damage,[16] protein oxidation,[17] lipid peroxidation,[18] and general oxidative stress.[19] Therefore, unintentional exposure of cells to ROS must be avoided. On the other hand, ROS are potent chemical agents that can be used for societal benefit, such as in water purification,[20] in catalysis, and as anti-bacterial agents. Therefore, it is important to understand the sources and fates of ROS, especially ·OH, to avoid toxic effects and maximize their potential applications.

A consequence of ·OH having high reactivity is that its lifetime is incredibly short (~100's ns).[21, 22] Additionally, its indiscriminate reactivity makes examining a particular reaction difficult, since there can be many interferents to also react with ·OH. Because of low concentrations, short lifetime, and lack of selectivity, detection of ·OH is challenging. To make matters more dire, ·OH absorbs light only in the far-UV,[23] making direct spectroscopic detection in most media difficult. A common approach for ·OH (and other ROS) is to use a probe molecule that reacts quickly with the ROS and then can easily be detected by absorbance, fluorescence, or mass spectroscopies.[24] The probe "scavenges" any generated ROS, and by detecting the concentration of the product or disappearance of the probe an amount of the ROS can be determined.

1.3 The place of diamond electrochemistry in water purification technologies.

The availability of clean drinking water has a profound impact on human health. Those in the developing world that lack adequate water purification and sanitation systems represent a significant fraction of the world population. The use of infected water can lead to a variety of bacterial diseases, including cholera, dysentery, and typhoid fever. These diarrheal diseases are particularly prevalent among children, for which they are a leading cause of death.[25] Although great strides have been made to improve water quality around the world, factors such as overpopulation, pollution,[26] and climate change[27] demand improved methods of water purification. Additionally, even in countries that have water purification systems in place, anthropogenic organic pollutants are increasingly finding their way into aqueous environments. For example, pharmaceuticals,[28, 29] pesticides,[30] artificial sweeteners,[31] perfluorinated surfactants,[32] disinfection byproducts, and other micropollutants have all been found in wastewaters. Highly stable and mobile molecules in wastewater, such as perfluorinated compounds, pose the greatest risk to drinking water, as they may bypass treatment facilities.[33] Chronic exposure to persistent pollutants in drinking water may be deleterious to human health, disrupting proper endocrine and reproductive function.[34] In addition, these pollutants can have negative impacts on aquatic ecosystems. For example, it is well known that oral contraceptives and other medications cause mutations in certain fish species, devastating their populations.[35, 36] Therefore, it is critical for us to understand how to remove these pollutants from wastewater systems. An ideal water purification technique would be safe, effective, efficient, inexpensive, and simple to perform, but no current technique matches meets all these criteria.

Advanced oxidation processes (AOPs) represent a large class of secondary water treatment techniques of growing research interest.[37, 38] AOPs are characterized by the production of reactive oxygen species (ROS) in water and are highly effective at degrading a variety of the aforementioned pollutants. Out of the many ROS created in AOPs, the hydroxyl radical (·OH) is the most powerful oxidant and is believed to be the main reason for AOP efficacy.[38, 39] ·OH can unselectively mineralize most organic and inorganic pollutants at near diffusion-limited rates,[15] making it a prime candidate to assist in water purification. As mentioned above, ·OH can be formed in nature, but all engineered AOPs involve some intentional combination of ultra-violet (UV) light, chemical oxidants (H_2O_2, O_3, or Cl_2), and/or electricity. One example of a photochemical AOP involves the photo-assisted production of ROS through chlorine intermediates (HOCl/UV).[40] Another long-standing and ubiquitous chemical/photochemical AOP is the Fe^{2+}-catalyzed decomposition of H_2O_2 to ·OH (Fenton's reaction).[13, 41] Fenton chemistry has been studied in a variety of laboratory and environmental settings.[42–45] Additionally, titanium dioxide (TiO_2), a wide band-gap semiconductor, has been used as a photocatalyst on the nano- and micro-scales for enhancing degradation of aqueous pollutants.[46–48] All these techniques have the potential to produce the desired ·OH and effectively degrade pollutants.

However, there are two inherent drawbacks to any chemical or photochemical AOP. First, the addition of external reagents is usually required (e.g., O_3, TiO_2, H_2O_2), which increases cost and complexity. Additionally, although the lifetime of ·OH in solution is only on the order of hundreds of nanoseconds,[21, 22] longer-lived disinfection byproducts from the primary oxidants could act as pollutants themselves. Second, large quantities of chemical oxidants and/or UV lamps are only practical on large scales where water treatment systems are already in place. It would be difficult for these methods to be point-of-use in remote areas of the world, which lack the necessary infrastructure. Therefore, not all AOPs will be suitable for every location, every scale, and every water treatment need.

Electrochemical advanced oxidation processes (EAOPs) could fill this gap within water purification technologies. EAOPs create ·OH from water itself at the surface of an electrode through an applied potential ($H_2O \rightarrow \cdot OH + H^+ + e^-$).[20, 42] These processes do require electrical power, but do not require chemical oxidants or UV light, making them simpler to perform than the above methods. Furthermore, since H_2O itself is the source of ·OH, the risk of forming hazardous degradation byproducts is decreased. Additionally, EAOPs can degrade some pollutants more effectively than other AOPs through direct electron transfer reactions of the pollutant with the electrode itself.[49] Ideally, water in remote areas would be purified by passing electric current through the right electrode with little adverse environmental or health effects. Such a method would be safe, simple, inexpensive, and effective.

However, the thermodynamics of water oxidation remain an important barrier to efficiently using EAOPs for water purification. Any electrochemical system (i.e., combination of solution, electrodes, cell geometry, etc.) is fundamentally limited by its solvent potential window, beyond which currents are dominated by oxidation or reduction of the solvent rather than the reaction of interest. Oxidation of water to form ·OH is always thermodynamically less favorable than oxidation to O_2, given that the corresponding cathodic reaction is water reduction to H_2 in both cases. This means that under anodic potentials positive enough to produce ·OH, O_2 will always be produced as the majority product. The large amount of current producing O_2 increases cost and purification time, and results in a diminished amount of the desired product (i.e., clean H_2O). Selectivity for forming ·OH over O_2 during water oxidation can be viewed as an indirect measure of EAOP efficiency and optimizing the system to produce a maximal amount of ·OH with relatively limited O_2 production is a major research challenge. An additional challenge is that the electrode material must withstand extremely oxidizing conditions for extended time. Despite the thermodynamic limits of EAOPs, various electrochemical and material properties may be leveraged to improve ·OH production efficiency through kinetic control.

Traditional, inert electrode materials (i.e., Pt, Au) are not suitable for EAOPs because they are expensive and can catalyze the oxygen evolution reaction (OER) too well. Poor OER catalysts may instead be effective ·OH producers. Several electrode materials have already been employed, including doped-SnO_2,[50] PbO_2,[51, 52] and boron-doped diamond (BDD).[53, 54] SnO_2 and PbO_2 possess moderately high overpotentials for the OER and are relatively stable but can leech toxic metal ions into solution. Alternatively, BDD is a widely used, extremely stable, non-toxic, OER-inactive electrode material. Intrinsic diamond is electrically insulating, but when heavily doped with boron it becomes semi-metallic.[5, 55] This allows for the outstanding chemical and physical stability of diamond to be applied as an electrode. Its large overpotential for OER and stability under strong anodic conditions have made it a popular material for producing ·OH.[51, 53, 54, 56] However, its relatively high cost and low efficiency prohibit it from being applied worldwide. Additionally, the mechanisms for ·OH and O_2 generation on BDD are not well understood. Therefore, if we can understand how and why BDD is effective at producing ·OH compared to O_2 and further optimize the reaction, other safe and inexpensive materials could be developed with similar properties to efficiently purify water.

1.4 Interaction of nanomaterials with biological systems.

With increasing use of electric vehicles and portable electronic devices, demand for Li ion batteries is rapidly expanding. A major class of Li ion battery cathode materials are $LiCoO_2$-based compounds, or "NMC" compositions ($LiNi_xMn_yCo_{1-x-y}O_2$, x,y < 1), in micro- and nano-structured forms. This transition metal composition is frequently tuned to improve battery performance and decrease cost.[57, 58] However, recycling of battery materials is not incentivized and there is a lack of recycling infrastructure for the growing amount of these materials.[59] This leads to an unfortunate reality of exposing $LiCoO_2$ and like materials to the environment after consumption.

Upon environmental exposure, metal oxide nanoparticles have several routes towards toxicity: ion release, physical damage, generation of abiotic ROS, and surface transformation of nearby biomolecules. Ion release simply involves dissolution and release of toxic metal such as Co^{+2} and Ni^{+2}. This has been observed for several $LiCoO_2$-like materials, and in composite materials ion release is incongruous (i.e., certain metals dissolve more readily from the lattice than others).[60, 61] Ion release can be partially mitigated by shifting the composition towards less toxic or less soluble metals, within allowance of performance. Physical damage refers to the fact that since nanomaterials are objects comparable to the sizes of cell organelles, they can enter organisms and cells to physically alter cell homeostasis. This includes damaging cell membranes, damaging cell cytoskeletons, denaturing proteins, or blocking narrow passages in tissues.[62] The formation of ROS (see section 1.3) is also possible from metal oxide nanomaterials in aqueous solution. While the processes are not fully understood, ROS have been detected from $LiCoO_2$ and NMC materials in variety of matrices and when exposed to a variety of organisms.[60, 63–66] Due to the difficulties in detecting ROS described above and the complexity of biological matrices, it is often difficult to 1) differentiate between several ROS, and 2) differentiate between ROS coming from the nanomaterial or ROS coming from the organism. Biotic ROS could be the natural response of the cell to what it accurately perceives is a threat, so-called oxidative stress. Depending on the identity of the ROS, abiotic or biotic ROS will cause toxicity as discussed in section 1.3 (e.g., DNA damage, lipid peroxidation).

Lastly, surface transformation of nearby biomolecules refers to direct surface reaction or catalysis by the nanoparticle with surrounding biomolecules (e.g., proteins or metabolites) without ROS intermediates. For example, nanoparticles in biological matrices readily acquire a corona of proteins and small molecules that depends on their surface chemistry.[67] Association with the nanoparticle surface could transform both the biomolecules and the nanoparticle. Despite the high oxidation states present in the common battery materials $LiCoO_2$ and NMC (implying potential for redox activity) and the use of these materials in catalysis,[68] few nanotoxicology studies have examined their interaction with redox-active biomolecules like nicotinamide adenine dinucleotide (NADH). If high valence metal oxide nanomaterials can react with biochemical electron-transporters, this would represent a new category of nanoparticle-based toxicity. Therefore, it is necessary to understand how technologically-relevant metal oxide nanomaterials interact with NADH and other small biomolecules with redox-activity, such as glutathione and flavins.

1.5 Scope of thesis.

As may be apparent from the abstract and introduction, this thesis covers two projects: one on the electrochemical generation of ·OH on diamond for water purification, and the other on the impacts of metal oxide nanomaterials on small redox-active biomolecules. Both projects are rooted in studying electron-transfer reactions at surfaces, reactive oxygen species, and implications for sustainability: whether they be beneficial in the case of water purification, or detrimental in the case of nanomaterial toxicity. Also, a similar suite of techniques is employed to study both systems, such as material characterization, surface analysis, electrochemical techniques, and fluorescence spectroscopy. Chapter 2 explores the reaction mechanisms generating ·OH and O_2 on the surface of BDD, and how the addition of a hydrophobic monolayer increase ·OH generation efficiency. Chapter 3 investigates the interactions of NADH and glutathione with the nano-scale Li ion battery cathode material $LiCoO_2$. This work discovered a new class of "reciprocal redox" reactions between reducing biomolecules and high valence metal oxides nanomaterials. Chapter 4 expands the work of Chapter 3 by examining the mechanism behind NADH-$LiCoO_2$ interaction and reproducing reciprocal redox phenomenon with other materials. This work revealed the surprising results that when exposing particles to constituent parts of NADH it was ribose, not nicotinamide, that reproduced the effects of NADH. Appendix 1 contains part of a collaborative study on ROS generation during $LiCoO_2$ dissolution. The study overall identified several mechanisms of $LiCoO_2$ toxicity in a model bacterium, including identifying H_2O_2 as the primary abiotic ROS generated. In this thesis a quality control investigation on the method for measuring H_2O_2 is reported, confirming the validity of H_2O_2 assays crucial to the study. Lastly, Appendix 2 describes an electrochemistry laboratory experiment developed for a general chemistry course. This discovery-based experiment grew out of science festival demonstrations to become a full-fledged part of the University of Wisconsin – Madison Chemistry curriculum and is shown to improve student understanding, appreciation, and engagement with the material.

1.6 Figures.

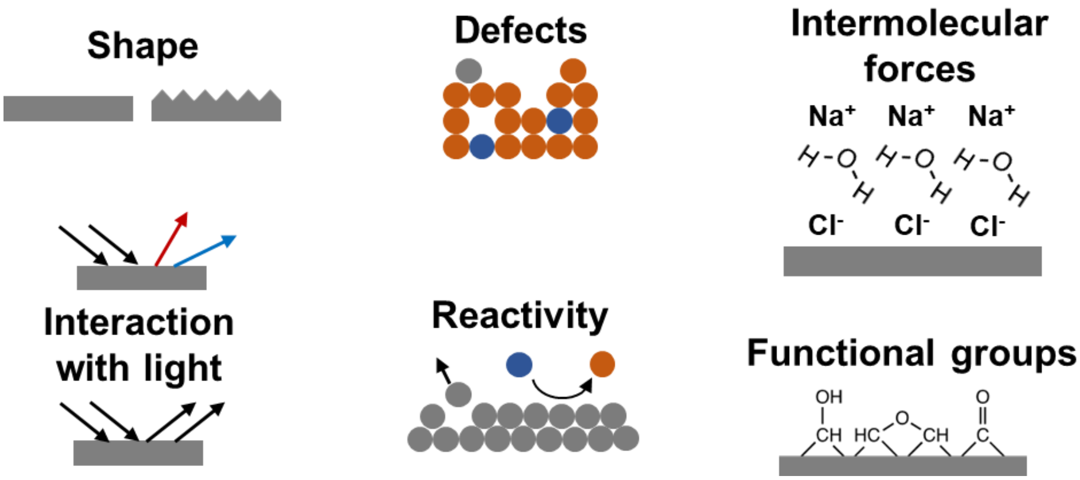

Figure 1.1. Examples of surface properties that influence chemical reactivity.

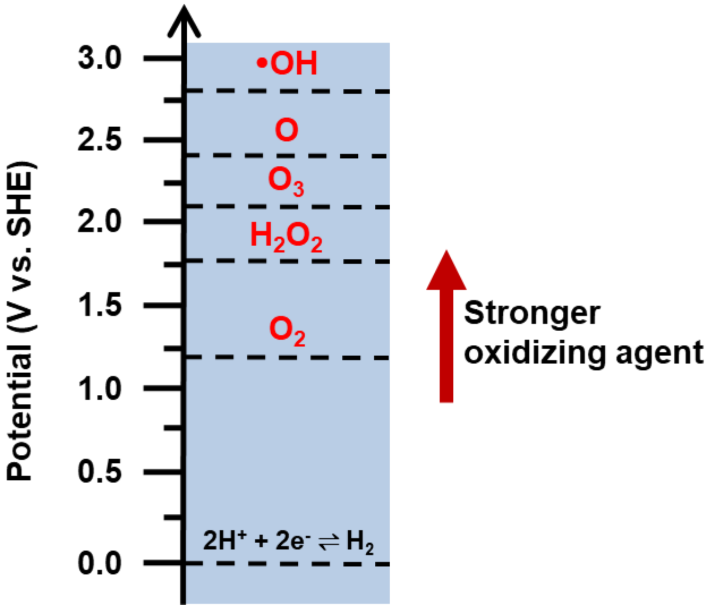

Figure 1.2. Comparison of oxidizing strength for O_2, hydrogen peroxide (H_2O_2), ozone (O_3), atomic oxygen (O), and hydroxyl radical (·OH), taken as standard reduction potentials for equilibrium with water.

1.7 References.

1. Goodenough, J. B.; Park, K. S., The Li-Ion Rechargeable Battery: A Perspective. *J. Am. Chem. Soc.* **2013**, *135*, 1167–1176.

2. Singla, M. K.; Nijhawan, P.; Oberoi, A. S., Hydrogen Fuel and Fuel Cell Technology for Cleaner Future: A Review. *Environ. Sci. Pollut. Res.* **2021**, *28*, 15607–15626.

3. Anichini, C.; Czepa, W.; Pakulski, D.; Aliprandi, A.; Ciesielski, A.; Samorì, P., Chemical Sensing with 2D Materials. *Chem. Soc. Rev.* **2018**, *47*, 4860–4908.

4. Mizushima, K.; Jones, P. C.; Wiseman, P. J.; Goodenough, J. B., A New Cathode Material for Batteries of High Energy Density. *Mater. Res. Bulliten* **1980**, *15*, 783–789.

5. Macpherson, J. V., A Practical Guide to Using Boron Doped Diamond in Electrochemical Research. *Phys. Chem. Chem. Phys.* **2015**, *17*, 2935–2949.

6. Patra, J. K.; Das, G.; Fraceto, L. F.; Campos, E. V. R.; Rodriguez-Torres, M. D. P.; Acosta-Torres, L. S.; Diaz-Torres, L. A.; Grillo, R.; Swamy, M. K.; Sharma, S.; Habtemariam, S.; Shin, H.-S., Nano Based Drug Delivery Systems: Recent Developments and Future Prospects. *J. Nanobiotech.* **2018**, *16*, 1–33.

7. Jones, Z. R.; Niemuth, N. J.; Shenderova, O. A.; Klaper, R. D.; Robinson, M. E.; Hamers, R. J., Selective Imaging of Diamond Nanoparticles within Fluorescence Contrast. *Environ. Sci. Nano* **2020**, *7*, 525-534.

8. Larson, R. A., Environmental Chemistry of Reactive Oxygen Species. *Environ. Sci. Tech.* **1978**, *8*, 197–246.

9. Chapman, S., A Theory of Upper-Atmospheric Ozone. *R. Meteorol. Soc. Mem.* **1930**, 103–125.

10. Wennberg, P. O., Atmospheric Chemistry - Radicals Follow the Sun. *Nature* **2006**, *442*, 145–146.

11. Rohrer, F.; Berresheim, H., Strong Correlation between Levels of Tropospheric Hydroxyl Radicals and Solar Ultraviolet Radiation. *Nature* **2006**, *442*, 184–187.

12. Gligorovski, S.; Strekowski, R.; Barbati, S.; Vione, D., Environmental Implications of Hydroxyl Radicals (·OH). *Chem. Rev.* **2015**, *115*, 13051–13092.

13. Haber, F.; Weiss, J., The Catalytic Decomposition of Hydrogen Peroxide by Iron Salts. *Proc. R. Soc. A* **1934**, *147*, 332–351.

14. Winterbourn, C. C., Reconciling the Chemistry and Biology of Reactive Oxygen Species. *Nat. Chem. Biol.* **2008**, *4*, 278–286.

15. Buxton, G. V.; Greenstock, C. L.; Helman, W. P.; Ross, A. B., Critical Review of Rate Constants for Reactions of Hydrated Electrons, Hydrogen Atoms and Hydroxyl Radicals (·OH/·O^- In Aqueous Solution. *J. Phys. Chem. Ref. Data* **1988**, *17*, 513–886.

16. Kasprzak, K. S., Oxidative DNA Damage in Metal-Induced Toxicity and Carcinogenesis. *Free Radic. Biol. Med.* **2002**, *32*, 958–967.

17. Jayaram, D. T.; Runa, S.; Kemp, M. L.; Payne, C. K., Nanoparticle-Induced Oxidation of Corona Proteins Initiates an Oxidative Stress Response in Cells. *Nanoscale* **2017**, *9*, 7595–7601.

18. Luo, X.; Pitkänen, S.; Kassovska-Bratinova, S.; Robinson, B. H.; Lehotay, D. C., Excessive Formation of Hydroxyl Radicals and Aldehydic Lipid Peroxidation Products in Cultured Skin Fibroblasts from Patients with Complex I Deficiency. *J. Clin. Invest.* **1997**, *99*, 2877–2882.

19. Cui, Y.; Melby, E. S.; Mensch, A. C.; Laudadio, E. D.; Hang, M. N.; Dohnalkova, A.; Hu, D.; Hamers, R. J.; Orr, G., Quantitative Mapping of Oxidative Stress Response to Lithium Cobalt Oxide Nanoparticles in Single Cells Using Multiplexed in Situ Gene Expression Analysis. *Nano Lett.* **2019**, *19*, 1990–1997.

20. Chaplin, B. P., Critical Review of Electrochemical Advanced Oxidation Processes for Water Treatment Applications. *Environ. Sci. Process. Impacts* **2014**, *16*, 1182–1203.

21. Attri, P.; Kim, Y. H.; Park, D. H.; Park, J. H.; Hong, Y. J.; Uhm, H. S.; Kim, K.; Fridman, A.; Choi, E. H., Generation Mechanism of Hydroxyl Radical Species and Its Lifetime Prediction during the Plasma-Initiated Ultraviolet (UV) Photolysis. *Sci. Rep.* **2015**, *5* (9332).

22. Pryor, W. A., Oxy-Radicals and Related Species: Their Formation, Lifetimes, and Reactions. *Annu. Rev. Physiol.* **1972**, *32*, 305–332.

23. Czapski, G.; Bielski, B. H. J., Absorption Spectra of the $\cdot$OH and $\cdot O^-$ Radicals in Aqueous Solutions. *Radiat. Phys. Chem.* **1993**, *41*, 503–505.

24. Fernández-Castro, P.; Vallejo, M.; San Román, M. F.; Ortiz, I., Insight on the Fundamentals of Advanced Oxidation Processes: Role and Review of the Determination Methods of Reactive Oxygen Species. *J. Chem. Tech. Biotech.* **2015**, *90*, 796–820.

25. Liu, L.; Johnson, H. L.; Cousens, S.; Perin, J.; Scott, S.; Lawn, J. E.; Rudan, I.; Campbell, H.; Cibulskis, R.; Li, M.; Mathers, C.; Black, R. E., Global, Regional, and National Causes of Child Mortality: An Updated Systematic Analysis for 2010 with Time Trends since 2000. *Lancet* **2012**, *379*, 2151–2161.

26. Reemtsma, T.; Berger, U.; Arp, H. P. H.; Gallard, H.; Knepper, T. P.; Neumann, M.; Quintana, J. B.; de Voogt, P., Mind the Gap: Persistent and Mobile Organic Compounds – Water Contaminants That Slip Through. *Environ. Sci. Tech.* **2016**, *50*, 10308-10315.

27. Levy, K.; Woster, A. P.; Goldstein, R. S.; Carlton, E. J., Untangling the Impacts of Climate Change on Waterborne Diseases: A Systematic Review of Relationships between Diarrheal Diseases and Temperature, Rainfall, Flooding, and Drought. *Environ. Sci. Tech.* **2016**, *50*, 4905–4922.

28. Bruce, G. M.; Pleus, R. C.; Snyder, S. A., Toxicological Relevance of Pharmaceuticals in Drinking Water. *Environ. Sci. Tech.* **2010**, *44*, 5619–5626.

29. Pharmaceuticals in Drinking-Water. *World Health Organization* **2011**, *50*.

30. Jiang, W.; Conkle, J. L.; Luo, Y.; Li, J.; Xu, K.; Gan, J. J., Occurrence, Distribution and Accumulation of Pesticides in Exterior Residential Areas. *Environ. Sci. Tech.* **2016**, *50*, 12592-12601.

31. Spoelstra, J.; Schiff, S. L.; Brown, S. J., Artificial Sweeteners in a Large Canadian River Reflect Human Consumption in the Watershed. *PLoS One* **2013**, *8*.

32. Eschauzier, C.; Beerendonk, E.; Scholte-Veenendaal, P.; De Voogt, P., Impact of Treatment Processes on the Removal of Perfluoroalkyl Acids from the Drinking Water Production Chain. *Environ. Sci. Tech.* **2012**, *46*, 1708–1715.

33. Richardson, S. D.; Kimura, S. Y., Water Analysis: Emerging Contaminants and Current Issues. *Anal. Chem.* **2016**, *88*, 546–582.

34. Colborn, T.; vom Saal, F. S.; Soto, A. M., Developmental Effects of Endocrine Disrupting Chemicals in Wildlife and Humans. *Environ. Impact Assess. Rev.* **1994**, *14*, 469–489.

35. Wise, A.; O’Brien, K.; Woodruff, T., Are Oral Contraceptives a Significant Contributor to the Estrogenicity of Drinking Water? *Environ. Sci. Tech.* **2011**, *45*, 51–60.

36. Kidd, K. A.; Blanchfield, P. J.; Mills, K. H.; Palace, V. P.; Evans, R. E.; Lazorchak, J. M.; Flick, R. W., Collapse of a Fish Population after Exposure to a Synthetic Estrogen. *Proc. Natl. Acad. Sci.* **2007**, *104*, 8897–8901.

37. Munter, R., Advanced Oxidation Processes – Current. *Proc. Est. Acad. Sci. - Chem.* **2001**, *50*, 59–80.

38. Ikehata, K.; Gamal El-Din, M., Degradation of Aqueous Pharmaceuticals by Ozonation and Advanced Oxidation Processes: A Review. *Ozone Sci. Eng.* **2006**, *28*, 353–414.

39. Glaze, W. H.; Kang, J.-W.; Chapin, D. H., The Chemistry of Water Treatment Processes Involving Ozone, Hydrogen Peroxide and Ultraviolet Radiation. *Ozone Sci. Eng.* **1987**, *9*, 335–352.

40. Jin, J.; El-Din, M. G.; Bolton, J. R., Assessment of the UV/Chlorine Process as an Advanced Oxidation Process. *Water Res.* **2011**, *45*, 1890–1896.

41. Babuponnusami, A.; Muthukumar, K., A Review on Fenton and Improvements to the Fenton Process for Wastewater Treatment. *J. Environ. Chem. Eng.* **2014**, *2*, 557–572.

42. Brillas, E.; Sirés, I.; Oturan, M. A., Electro-Fenton Process and Related Electrochemical Technologies Based on Fenton's Reaction Chemistry. *Chem. Rev.* **2009**, *109*, 6570–6631.

43. Nidheesh, P. V.; Gandhimathi, R.; Ramesh, S. T., Degradation of Dyes from Aqueous Solution by Fenton Processes: A Review. *Environ. Sci. Pollut. Res.* **2013**, *20*, 2099–2132.

44. Zepp, R. G.; Faust, B. C.; Holgne, J., Hydroxyl Radical Formation in Aqueous Reactions (pH 3-8) of Iron(II) with Hydrogen Peroxide: The Photo-Fenton Reaction. *Environ. Sci. Tech.* **1992**, *26*, 313–319.

45. Vermilyea, A. W.; Voelker, B. M., Photo-Fenton Reaction at near Neutral pH. *Environ. Sci. Tech.* **2009**, *43*, 6927–6933.

46. Nakabayashi, Y.; Nosaka, Y., OH Radical Formation at Distinct Faces of Rutile TiO_2 Crystal in the Procedure of Photoelectrochemical Water Oxidation. *J. Phys. Chem. C* **2013**, *117*, 23832–23839.

47. Likodimos, V.; Han, C.; Pelaez, M.; Kontos, A. G.; Liu, G.; Zhu, D.; Liao, S.; de la Cruz, A. A.; O'Shea, K.; Dunlop, P. S. M.; Byrne, J. A.; Dionysiou, D. D.; Falaras, P., Anion-Doped TiO_2 Nanocatalysts for Water Purification under Visible Light. *Ind. Eng. Chem. Res.* **2013**, *52*, 13957–13964.

48. Zhang, J.; Nosaka, Y., Quantitative Detection of OH Radicals for Investigating the Reaction Mechanism of Various Visible-Light TiO_2 Photocatalysts in Aqueous Suspension. *J. Phys. Chem. C* **2013**, *117*, 1383–1391.

49. Moreira, F. C.; Boaventura, R. A. R.; Brillas, E.; Vilar, V. J. P., Electrochemical Advanced Oxidation Processes: A Review on Their Application to Synthetic and Real Wastewaters. *Appl. Catal. B Environ.* **2017**, *202*, 217–261.

50. Zhao, G.; Cui, X.; Liu, M.; Li, P.; Zhang, Y.; Cao, T.; Li, H.; Lei, Y.; Liu, L.; Li, D., Electrochemical Degradation of Refractory Pollutant Using a Novel Microstructured TiO_2 Nanotubes/Sb-Doped SnO_2 Electrode. *Environ. Sci. Tech.* **2009**, *43*, 1480–1486.

51. Martínez-Huitle, C. A.; Quiroz, M. A.; Comninellis, C.; Ferro, S.; De Battisti, A., Electrochemical Incineration of Chloranilic Acid Using Ti/IrO_2, Pb/PbO_2 and Si/BDD Electrodes. *Electrochim. Acta* **2004**, *50*, 949–956.

52. Zhao, G.; Zhang, Y.; Lei, Y.; Baoying, L. V; Gao, J.; Zhang, Y.; Li, D., Fabrication and Electrochemical Treatment Application of a Novel Lead Dioxide Anode with Superhydrophobic Surfaces, High Oxygen Evolution Potential, and Oxidation Capability. *Environ. Sci. Tech.* **2010**, *44*, 1754–1759.

53. Michaud, P.; Panizza, M.; Ouattara, L.; Diaco, T.; Foti, G.; Comninellis, C., Electrochemical Oxidation of Water on Synthetic Boron-Doped Diamond Thin Film Anodes. *J. Appl. Electrochem.* **2003**, *33*, 151–154.

54. Marselli, B.; Garcia-Gomez, J.; Michaud, P.; Rodrigo, M. A.; Comninellis, C., Electrogeneration of Hydroxyl Radicals on Boron-Doped Diamond Electrodes. *J. Electrochem. Soc.* **2003**, *150*, D79–D83.

55. Patten, H. V.; Meadows, K. E.; Hutton, L. A.; Iacobini, J. G.; Battistel, D.; McKelvey, K.; Colburn, A. W.; Newton, M. E.; MacPherson, J. V.; Unwin, P. R., Electrochemical Mapping Reveals Direct Correlation between Heterogeneous Electron-Transfer Kinetics and Local Density of States in Diamond Electrodes. *Angew. Chemie - Int. Ed.* **2012**, *51*, 7002–7006.

56. Costa, C. R.; Montilla, F.; Morallon, E.; Olivi, P., Electrochemical Oxidation of Acid Black 210 Dye on the Boron-Doped Diamond Electrode in the Presence of Phosphate Ions: Effect of Current Density, PH, and Chloride Ions. *Electrochim. Acta* **2009**, *54* (27), 7048–7055.

57. Belharouak, I.; Sun, Y. K.; Liu, J.; Amine, K., $Li(Ni_{1/3}Co_{1/3}Mn_{1/3})O_2$ as a Suitable Cathode for High Power Applications. *J. Power Sources* **2003**, *123*, 247–252.

58. Conry, T. E.; Mehta, A.; Cabana, J.; Doeff, M. M., Structural Underpinings of the Enhanced Cycling Stability upon Al-Substitution in $LiNi_{0.45}Mn_{0.45}Co_{0.1-y}Al_yO_2$ Positive Electrode Materials for Li-Ion Batteries. *Chem. Mater.* **2012**, *24*, 3307–3317.

59. Dunn, J. B.; Gaines, L.; Kelly, J. C.; James, C.; Gallagher, K. G., The Significance of Li-Ion Batteries in Electric Vehicle Life-Cycle Energy and Emissions and Recycling's Role in Its Reduction. *Energy Environ. Sci.* **2015**, *8*, 158–168.

60. Bozich, J.; Hang, M.; Hamers, R.; Klaper, R., Core Chemistry Influences the Toxicity of Multicomponent Metal Oxide Nanomaterials, Lithium Nickel Manganese Cobalt Oxide, and Lithium Cobalt Oxide to Daphnia Magna. *Environ. Toxicol. Chem.* **2017**, *36*, 2493–2502.

61. Hang, M. N.; Gunsolus, I. L.; Wayland, H.; Melby, E. S.; Mensch, A. C.; Hurley, K. R.; Pedersen, J. A.; Haynes, C. L.; Hamers, R. J., Impact of Nanoscale Lithium Nickel Manganese Cobalt Oxide (NMC) on the Bacterium Shewanella oneidensis MR-1. *Chem. Mater.* **2016**, *28*, 1092–1100.

62. Sukhanova, A.; Bozrova, S.; Sokolov, P.; Berestovoy, M.; Karaulov, A.; Nabiev, I., Dependence of Nanoparticle Toxicity on Their Physical and Chemical Properties. *Nanoscale Res. Lett.* **2018**, *13* (44).

63. Buchman, J. T.; Bennett, E. A.; Wang, C.; Tamijani, A.; Bennett, J. W.; Hudson, B. G.; Green, C. M.; Clement, P. L.; Zhi, B.; Henke, A. H.; Laudadio, E. D.; Mason, S. E.; Hamer, R. J.; Klaper, R. D.; Haynes, C. L., Nickel Enrichment of Next-Generation NMC Nanomaterials Alters Material Stability, Causing Unexpected Dissolution Behavior and Observed Toxicity to S. Oneidensis MR-1 and D. magna. *Environ. Sci. Nano* **2020**, *7*, 571–587.

64. Melby, E. S.; Cui, Y.; Borgatta, J.; Mensch, A. C.; Hang, M. N.; Chrisler, W. B.; Dohnalkova, A.; Van Gilder, J. M.; Alvarez, C. M.; Smith, J. N.; Hamers, R. J.; Orr, G., Impact of Lithiated Cobalt Oxide and Phosphate Nanoparticles on Rainbow Trout Gill Epithelial Cells. *Nanotoxicology* **2018**, *12*, 1166–1181.

65. Chattopadhyay, S.; Dash, S. K.; Tripathy, S.; Das, B.; Mandal, D.; Pramanik, P.; Roy, S., Toxicity of Cobalt Oxide Nanoparticles to Normal Cells; An in vitro and in vivo Study. *Chem. Biol. Interact.* **2015**, *226*, 58–71.

66. Papis, E.; Rossi, F.; Raspanti, M.; Dalle-Donne, I.; Colombo, G.; Milzani, A.; Bernardini, G.; Gornati, R., Engineered Cobalt Oxide Nanoparticles Readily Enter Cells. *Toxicol. Lett.* **2009**, *189*, 253–259.

67. Stepien, G.; Moros, M.; Pérez-Hernández, M.; Monge, M.; Gutiérrez, L.; Fratila, R. M.; Las Heras, M. De; Menao Guillén, S.; Puente Lanzarote, J. J.; Solans, C.; Pardo, J.; de la Fuente, J. M., Effect of Surface Chemistry and Associated Protein Corona on the Long-Term Biodegradation of Iron Oxide Nanoparticles in Vivo. *ACS Appl. Mater. Interfaces* **2018**, *10*, 4548–4560.

68. Lu, Z.; Wang, H.; Kong, D.; Yan, K.; Hsu, P.; Zheng, G.; Yao, H.; Liang, Z.; Sun, X.; Cui, Y., Electrochemical Tuning of Layered Lithium Transition Metal Oxides for Improvement of Oxygen Evolution Reaction. *Nat. Commun.* **2014**, *5* (4345).

Chapter 2. Enhancing Electrochemical Efficiency of Hydroxyl Radical Formation on Diamond Electrodes by Functionalization with Hydrophobic Monolayers

The following chapter is adapted from the article published in *Langmuir* 2019, 35, 2153–2163 (DOI: 10.1021/acs.langmuir.8b04030), with the co-authors Timothy P. Saunders, Joel A. Pedersen, and Robert J. Hamers. All of the data collection, data analysis, manuscript preparation, and revision were done by Austin H. Henke under the advisement of Robert J. Hamers except for the following: Timothy P. Sauders assisted with fluorescence experiments and Joel A. Pedersen made intellectual contributions towards data analysis and manuscript preparation/revision.

This work was supported by the Wisconsin Alumni Research Foundation UW2020 initiative. The authors gratefully acknowledge use of facilities and instrumentation supported by NSF through the University of Wisconsin Materials Research Science and Engineering Center (DMR-1720415).

2.1 Introduction.

The selective electrochemical formation of energetic chemical species is of great interest as one approach to induce chemical transformations in an energy-efficient manner.[1-6] The electrochemical formation of hydroxyl radicals (·OH) has emerged as a particularly important example because hydroxyl radicals are potent oxidants capable of oxidizing a wide variety of organic and inorganic contaminants at near-diffusion-limited rates,[7, 8] leading to intense interest in the use of ·OH for applications such as water purification.[8-14] Electrochemical generation of ·OH possesses a number of advantages over existing water purification approaches in large part because no reagents need to be added to produce the oxidant.

The Faradaic efficiency for ·OH production from H_2O is poor because the direct, one-electron reaction $H_2O \rightarrow \cdot OH + H^+ + e^-$ has an associated standard reduction potential ($E^0 = 2.74$ V) that is unfavorable compared to the two-electron oxidation $H_2O \rightarrow H_2O_2 + 2H^+ + 2e^-$ ($E^0 = 1.74$ V) and the four-electron oxidation $H_2O \rightarrow O_2 + 4H^+ + 4e^-$ ($E^0 = 1.23$ V) processes. Since oxidation of water to form O_2 is the most thermodynamically favorable reaction, increases in production of ·OH must involve manipulation of the kinetic pathways, either by reducing the rate of the four-electron oxidation that produces O_2 or by increasing the rate of formation of ·OH. Empirically, it is known that SnO_2,[15] PbO_2,[16, 17] and boron-doped diamond[13, 14] are the electrode materials with highest efficiency for producing ·OH. Of these, boron-doped diamond (BDD) is recognized as having the best overall performance because it produces aqueous ·OH,[12-14, 18] is chemically and physically robust,[19] and has a high kinetic overpotential for oxidation of water to O_2.[14, 20-23]

While it is known empirically that diamond is comparatively good at producing ·OH radicals, the detailed electrochemical pathways for forming ·OH and O_2 at diamond surfaces are not well understood,[13, 14, 21, 24] inhibiting efforts to identify materials that could be even more selective at producing ·OH. A recent computational study examining water oxidation on metal oxides calculated the free energies of M–OH, M–O, and M–OOH intermediates (where M = metal) and reported that oxides with the largest free energy of formation of M–OH were most effective at forming hydroxyl radicals.[25] Yet, electrochemical reactions on diamond are quite distinct from those on metal oxides because while metal oxides have labile M–O and MO–H bonds that can transiently produce active surface sites to facilitate inner-sphere reactions, the C–H, C–O and CO–H bonds at diamond surfaces are very strong and non-labile, disfavoring inner-sphere reaction pathways.[26, 27] Density functional calculations have estimated the C–O and C–OH bond strengths at diamond surfaces to be 4-5 eV (400-500 kJ/mole), depending on the precise crystal face and surface coverage.[28] Similarly, the O–H dissociation constants K_a of aliphatic alcohols are small: $K_a \approx 10^{-18}$ for tert-butanol,[29] corresponding to free energy changes of ~100 kJ/mole. These values show that while oxidized BDD (O-BDD) surfaces may have a number of species,[30-34] these do not necessarily provide labile sites for inner-sphere electrochemical reactions.[26, 27] One potentially important property controlling electrochemical pathways on diamond is surface hydrophobicity, which impacts the organization of the adjacent water molecules.[35, 36] Surface hydrophobicity can manipulated via direct fluorination of diamond[37-42] (F-BDD) and by functionalization with polyfluorinated ligands (PF-BDD).[43] These surface modifications have been shown to yield very hydrophobic surfaces with only very weak interaction with water.[35, 36] The high C-F bond strength (calculated at 506 kJ/mole)[44] suggests that using fluorinated surfaces or ligands provides a robust way to potentially alter the relative rates of O_2 and ·OH production.

Here, we demonstrate that functionalization of conductive diamond surfaces with hydrophobic ligands significantly increases the efficiency of formation of ·OH radicals. We formed hydrophobic electrodes by covalently linking polyfluorinated molecules to conductive, boron-doped diamond (BDD) surfaces, and then compared the ·OH production efficiencies of these functionalized surfaces with those of hydrogen-terminated (H-BDD), ether-terminated (E-BDD), and O-BDD surfaces. Figure 2.1 shows schematics of the four types of functionalized BDD analyzed. Electrochemical generation of ·OH radicals was quantified using terephthalic acid (TPA), which selectively reacts with ·OH to produce a single, easily detected product.[45-48] We demonstrate that functionalization of BDD anodes with hydrophobic, polyfluorinated ligands leads to a significant enhancement in electrochemical ·OH production efficiency that persists even after 24 h of constant electrolysis. Our results suggest that a key to increasing efficiency for ·OH production is to control the surface composition and structure in a manner that reduces the possibility of inner-sphere, multi-electron oxidation steps that lead to O_2, without inhibiting the outer-sphere, single-electron oxidation pathway that produces ·OH.

2.2 Experimental.

2.2.1 Electrode preparation.

Experiments reported here used boron-doped, polycrystalline, electrochemical-grade diamond electrodes ($\rho < 2 \cdot 10^{-3}$ Ω·m, $[B] \approx 10^{20}$ atom·cm^{-3}) purchased from Element Six. The free-standing BDD electrodes were cleaned by first soaking in aqueous piranha solution (3:1 v:v concentrated H_2SO_4 : 30% H_2O_2) overnight and then by rinsing with hydrofluoric acid (Sigma Aldrich, 48%), followed by nanopure water (Barnstead Genpure system, $\rho > 18.2$ MΩ·cm). Samples were hydrogen-terminated by exposure to a pure hydrogen plasma in an Astex microwave chemical vapor deposition system using a microwave power of 600 W ($T \approx 450$ °C) and pressure ~ 3 torr. The resulting H-terminated boron-doped diamond (H-BDD) samples were stored under dry argon between experiments to prevent surface oxidation or accumulation of

H_2O in atmosphere. To produce oxygen terminated BDD (O-BDD), H-BDD samples were placed in aqueous 30% H_2O_2 and illuminated with light from a low-pressure mercury ultraviolet (UV) lamp at 254 nm (UVP Pen-Ray Grid, 254 nm, ~ 15 $mW \cdot cm^{-2}$) for at least 30 min.

We used photochemically initiated grafting of terminal organic alkenes[49-51] to functionalize H-BDD with polyfluorinated ligands and a polyethylene-ether. H-BDD electrodes were placed in a stainless-steel reaction vessel under dry argon. The surface of the H-BDD sample was covered with a single reactant of interest, typically requiring 20 – 60 μL. The reactants used are 1,1,2-H-perfluoro-oct-1-ene ("PF-8", Alfa Aesar, 99%), 1,1,2-H-perfluoro-dec-1-ene ("PF-10", Alfa Aesar, 99%), and allyloxy(diethylene oxide)-methyl-ether (Gelest, 95%) that were previously dried using molecular sieves. The reaction vessel was sealed with a UV-grade fused silica window and illuminated with light from a UV lamp (similar to the above) for 24 hr. The vessel was water-cooled to prevent evaporation of the reactant. Next, the electrode was removed from the vessel, soaked for 30 min each in chloroform (Sigma Aldrich, 99.8%) and methanol (Fisher, 99.9%) to remove excess reactant, and dried under nitrogen to produce either a polyfluorinated BDD (PF-BDD) electrode or a polyethylene-ether-functionalized BDD (E-BDD) electrode. We performed control experiments with PF-BDD to quantify non-covalent adsorption to BDD using the same procedure as above, except without UV illumination.

We primarily report results for experiments with PF-8 functionalized BDD, which are referred to as PF-BDD. Most experiments were also conducted with PF-10 functionalized BDD, which yielded similar results to PF-8 BDD, indicating their behavior is characteristic of this class of molecules. See Table 2.1 for a direct comparison. For selected experiments, E-BDD acts as a control, since it contains a monolayer of ligands similar in length to those of PF-BDD, but that are more hydrophilic. All experiments were performed in at least triplicate and reported errors are standard error of the mean from replicate samples.

2.2.2 Electrode characterization.

We determined the elemental composition of BDD surfaces using an ultrahigh vacuum X-ray photoelectron spectroscopy (XPS) system with a monochromatized Al Kα x-ray source and a hemispherical analyzer. Survey spectra were obtained summing three scans with a binding energy step size of 1 eV and high-resolution spectra were obtained summing 20 scans with step size of 0.125 eV. Casa XPS software was used for data analysis. For area quantification, peaks were fit to 70:30 Gaussian–Lorentzian functions with Shirley[52] background correction.

Electrode water droplet contact angles were measured using a Dataphysics OCA15 Goniometer with droplet volume of 8 μL and application rate of 0.5 μL/s. SCA20 software was used to capture images and calculate angles for advancing, needle-in sessile droplets.

2.2.3 Electrochemical measurements and solutions.

Electrochemical experiments were performed on a Metrohm Autolab 302N Potentiostat-Galvanostat and data were analyzed using NOVA 1.6 software. To quantify the production of ·OH, we used the oxidation of terephthalic acid (TPA) to 2-hydroxy-terephthalic acid (HTPA), for which the reaction is shown in Scheme 2.1. We used TPA specifically because (1) TPA does not directly oxidize on electrode surfaces as easily as other common ·OH probes,[53] and (2) a single product (HTPA) can be quantified via fluorescence. We prepared NaH_2PO_4/Na_2HPO_4 buffered solutions at pH 7.4 and pH 9.2 by adding H_3PO_4 (Sigma Aldrich, 85% in H_2O) as needed to a solution of 0.1 M Na_2HPO_4 (Fisher, 99.8%) in nanopure water. These solutions were used to prepare a 0.50 mM TPA stock solutions using disodium terephthalate (Alfa Aesar, 99%). Under our experimental conditions (pH 7.4), the reaction rate of ·OH with TPA is over 100× faster than that for any suspected competing reaction, as determined from literature second-order rate constants and approximate concentrations (see Table 2.2). The TPA solution was placed in the anode compartment and the buffer in the cathode compartment of an open-air, two-compartment cell with a finely porous glass frit separator. BDD was used as the working electrode, platinum mesh as the counter electrode, and 3 M Ag|AgCl as the reference electrode. Without stirring, a potential of 2.7 V vs. SHE was applied to the working electrode for 30 min while measuring current ($\Delta t = 0.5$ s). Then, the electrolyte within the anode compartment was removed and analyzed via fluorescence. We explored the behavior over a range of potentials, and data shown here were obtained at 2.7 V. This potential was selected because it is close to the minimum needed to produce ·OH at circumneutral pH ($E^0 = 2.74$ V; $E = 2.3$ V at pH = 7) and yielded higher efficiencies than more oxidizing potentials.

To further characterize differences in electrochemical performance, cyclic voltammetry (CV) was performed using functionalized BDD working electrodes in the same buffered TPA solution as above before and after a 30-min electrolysis in a one-compartment cell. For a given electrode, 5 scans were recorded at 50 mV·s^{-1} from +0.5 V → +3.5 V → -2.0 V → +0.5 V vs. SHE. Then, 2.7 V vs. SHE was applied for 30 min. Lastly, the 5 scans were repeated as above, without changing the solution. A platinum disk was used as the counter electrode, and 3 M Ag│AgCl as the reference electrode.

2.2.4 Fluorescence measurements.

We measured fluorescence of HTPA using an ISS K2 spectrofluorimeter. Measurement conditions are similar to those used previously,[45-48] and were reproduced and optimized for our system. Emission spectra for HTPA solutions were measured from 340 – 550 nm using an excitation wavelength of 315 nm. The fluorescence spectrum exhibits a maximum at 422 nm. Quantification of HTPA was conducted by converting the fluorescence intensity at this wavelength to HTPA concentration using a calibration curve (Figure 2.9). Further information on fluorescence calibration and normalization procedures can be found in section 2.5.3. The UV-visible absorption spectra of TPA and HTPA reported both here (Figure 2.9B) and in the literature[46] reveal that TPA displays negligible absorption at the excitation wavelength.

2.3 Results and discussion.

2.3.1 Functionalization of BDD.

X-ray photoelectron spectroscopy characterization of the surface composition of H-BDD, O-BDD, and PF-BDD, yielded the results shown in Figure 2.2. Freshly prepared H-BDD (Figure 2.2A) shows a strong C(1s) peak near 282 eV and a C KVV Auger peak near 1220 eV, without any other detectable species except for a very small O(1s) feature near 529 eV. The spectrum for O-BDD (Figure 2.2B) is similar to that of H-BDD, with the addition of more intense O(1s) and O KLL Auger peaks around 529 eV and 974 eV, respectively, due to surface oxidation. After functionalizing H-BDD with polyfluoroalkene molecules, the spectrum (Figure 2.2C) exhibits strong F(1s) (686 eV) and F KLL Auger (832 eV) peaks. Furthermore, the high-resolution C(1s) spectrum for PF-BDD (Figure 2.10) shows new peaks at higher binding energies than the diamond C(1s) peak corresponding to C–F_2 and C–F_3 species within the ligand layer. The F(1s) peaks and C(1s) sub-peaks at higher binding energies for the PF-BDD samples and the absence of impurity peaks confirm that the diamond surfaces have been functionalized with the perfluorinated molecules. Upon functionalization of H-BDD with the polyethylene-ether ligands (E-BDD), the O(1s) peak near 529 eV increases in intensity compared to the starting H-BDD sample (Figure 2.11) due to the presence of ether oxygen atoms. Unlike PF-BDD, E-BDD functionalization does not yield new peaks because the corresponding ligands contain only C and O.

We determined the density of PF molecules grafted to the BDD surface using the C(1s) and F(1s) peak areas of high-resolution XPS spectra and the equations described in section 2.5.4. These measurements yielded a molecular surface density for PF-BDD of 3.5 ± 0.3 molecule·nm^{-2}. This is indistinguishable from the packing density of ~3.5 molecules nm^{-2} observed for perfluorinated solid alkanes,[54] but is significantly smaller than the ~16 atom·nm^{-2} density of carbon atoms on the diamond (111) surface. Our measured coverage is consistent with prior work from our group in which we established that the reaction conditions used here will covalently graft terminal alkenes to diamond surfaces, yielding monolayer films like those depicted in Figure 2.1C.[49, 51, 55-57] However, because the lattice spacing of diamond is less than the maximum packing density of perfluorinated solid alkanes, the PF molecules cannot functionalize every C–H surface bond; as a consequence, some C–H surface sites are expected to remain un-functionalized, as depicted in Figure 2.1C.[57] This non-ideal packing and associated molecular disorder has important consequences for surface electron-transfer processes,[57] as will be discussed below.

As a control, Figure 2.2D shows an XPS spectrum of a H-BDD sample that was exposed to the PF ligand but not illuminated with UV light; this control sample shows a much lower F(1s) signal compared to that of PF-BDD with UV illumination (Figure 2.2E). This experiment further confirms that UV induces covalent grafting of PF molecules to the BDD surface as depicted in Figure 2.2C.[51, 55]

One attractive feature of BDD as a substrate is that samples can be re-used many times, as the molecular ligands can be removed and the hydrogen termination restored by exposing the sample to a hydrogen plasma. Figure 2.2E shows an XPS spectrum of a PF-BDD sample (like that of Figure 2.2C) that was then exposed to a H_2 plasma (600 W total microwave power) for 1 hour. Analysis of the F(1s) region shows that more than 99% of the surface F has been removed and the sample is chemically indistinguishable from a clean control sample. Scanning electron microscopy images (Figure 2.12) further show that H_2 plasma treatment does not affect the morphology of polycrystalline BDD. In multiple studies, we established that BDD samples can be functionalized and H-plasma cleaned many times with no detectable change in electrochemical behavior.

2.3.2 Faradaic efficiency of ·OH production on functionalized BDD.

We probed the production of ·OH by BDD samples functionalized with each molecule by electrolyzing solutions containing TPA, and then quantifying the HTPA produced. We also measured electrolytic current as a function of time (*I(t)*). Since the number of HTPA molecules observed is much less than the total number of electrons passed ($mol\ e^- = \frac{1}{F}\int I(t)dt$, where F is Faraday's constant), most of the current is associated with other oxidation reactions such as oxidation of water to O_2. Therefore, we use electrolytic current as an indirect measure of O_2 production. The Faradaic efficiency (η) for HTPA production during electrolysis is defined as:

$$\eta = \frac{CVF}{\int I(t)dt} \tag{2.1}$$

where C is the measured final concentration of HTPA, V is the solution volume within the anode compartment, and F is Faraday's constant. In this context, η is the fraction of electrons that produce HTPA, and $\eta << 1$ due to the dominance of oxygen evolution.

To estimate how η relates to ·OH generation efficiency, we measured the rate of HTPA production as a function of [TPA] (Figure 2.13A) for 30-min electrolyses, and found that HTPA production increases linearly with [TPA] at low concentration (e.g., 0.5 mM), and plateaus to become independent at high [TPA] (~5 mM). We assign this as a first order reaction of ·OH and TPA with respect to TPA that becomes pseudozero order at high [TPA]. Since [·OH] << [TPA], we assume that in the plateau region all ·OH is captured to produce HTPA. The TPA concentration used herein (0.5 mM) falls within the linear region of Figure 2.13 and yields an ·OH capture efficiency of ~20%. Therefore, our reported Faradaic efficiencies for HTPA generation are a *minimum* for absolute ·OH generation efficiency, which is likely 5× higher. Lastly, we note that the above deviation in HTPA generation from linearity at high concentrations is not due to self-absorption or molecular aggregation of HTPA, as absorbance of HTPA is linear with [HTPA] for the full concentration range tested (Figure 2.13B).

Figure 2.3 shows Faradaic efficiencies, while Figure 2.4 shows the corresponding HTPA production and the total electrochemical charge passed (all values totaled over 30 minutes) for the different BDD samples at pH = 7.2 and at pH = 9.2. We first consider the influence of surface functionalization. At pH = 7.4, Figure 2.3 shows that PF-BDD electrodes produce ·OH with significantly higher Faradaic efficiency than O-BDD, H-BDD, or E-BDD electrodes. Figure 2.4A shows that the rate of HTPA production does not differ significantly ($p > 0.05$) among BDD electrodes. Yet, the electrolytic current (Figure 2.4B) varies markedly, with PF-BDD yielding much lower current than H-BDD or O-BDD at both pH values tested. The trend in average electrolytic current is consonant with that observed for measured efficiencies in Figure 2.3. PF-BDD has the lowest electrolytic current and the highest Faradaic efficiency, while O-BDD has the highest electrolytic current and the lowest Faradaic efficiency. Similar trends are observed when comparing the differently functionalized surfaces at pH = 9.2.

Since production of HTPA (a proxy for ·OH) is nearly independent of surface functionalization, we conclude that ·OH production likely occurs by an outer-sphere electron-transfer process. In contrast, the strong dependence of total electrolytic current (which primarily reflects production of O_2) on surface functionalization indicates that O_2 production occurs by an inner-sphere process. We conclude that PF-BDD has the highest Faradaic efficiency among the tested surfaces because the PF layer is most effective at inhibiting oxygen evolution.

Figure 2.3 also shows the results of quenching experiments performed with O-BDD and PF-BDD. In these experiments, electrolyses were conducted just as described, except with *t*-butanol (t-BuOH, 0.3 M) added to the electrolyte. t-BuOH is an effective ·OH scavenger also resistant to direct oxidation on the electrode surface,[58] so this experiment was conducted to further ensure that ·OH oxidation produces HTPA. Our results show that the addition of t-BuOH dramatically decreases HTPA generation efficiency for both O-BDD and PF-BDD, suggesting that HTPA is generated from reaction of TPA with ·OH, and that the presence of t-BuOH prevents this reaction. A comparison of the electrolytic currents and HTPA production rates for the quenching experiments with other experiments is in Figure 2.14.

2.3.3 Effect of pH on water oxidation for functionalized BDD.

We now consider the influence of pH. In Figure 2.4, the data show that increasing the concentration of hydroxyl anions 60-fold (increasing from pH = 7.4 to pH = 9.2) leads to modest *decreases* in both HTPA production and in electrolytic current, and Figure 2.3 shows concurrent decrease in Faradaic efficiency for HTPA production. The pH = 7.4 and pH = 9.2 solutions have nearly the same ionic strength ($I_{pH\ 7.4} \approx 28$ mM, $I_{pH\ 9.2} \approx 25$ mM), such that differences in solution conductivity are negligible. The observed influence of increasing pH is contrary to what we expect if ·OH was formed primarily from oxidation of OH^-. Therefore, we conclude that the ·OH radicals that we detect arise from oxidation of H_2O and not from oxidation of hydroxyl anions.

The above interpretation assumes that the fluorescence quantum yield of HTPA does not depend strongly on pH within the range tested. Figure 2.15 shows that the fluorescence intensities of standard HTPA solutions are nearly constant for $6 < pH < 12$, in agreement with prior work.[48] Therefore, we conclude that differences in fluorescence between solutions of pH = 7.4 and pH = 9.2 are due to differences in HTPA concentration, further confirming our conclusion that the ·OH we detect is produced by oxidation of H_2O and not by oxidation of OH^-.

2.3.4 Cyclic voltammetry of functionalized BDD electrodes.

Cyclic voltammetry (CV) was performed with each type of functionalized BDD before and after electrolysis to observe the solvent potential window, background current, and any possible changes to these with use. Figure 2.5A-D shows the first scan of the CVs before electrolysis. The applied potential for all electrolyses is shown as a dotted line in these graphs for comparison. PF-BDD's solvent window remains wider in subsequent scans (data not shown). The peaks around +2 V in the forward sweep for O-BDD, H-BDD, and E-BDD are attributed to oxidation of carbon atoms on the diamond surface. No other major peaks were observed, indicating an absence of interfering electrochemical processes. In all subsequent scans (data not shown), these surface oxidation peaks remain present. We hypothesize that in the negative sweep of the same scan (e.g., -2 V), the electrode surface becomes reduced, such that in the positive sweep of the following scan a similar surface oxidation peak emerges. CVs with O-BDD and H-BDD electrodes after 30-min electrolyses (Figure 2.5E-F), when the surface is likely fully oxidized, further support this conclusion. The first scan after electrolysis does not contain the surface oxidation peak, whereas the second scan (after running the reductive sweep of scan 1) does show the same surface oxidation peak. This eliminates the possibility that the peak instead corresponds to direct oxidation of TPA on the electrode surface. Notably, PF-BDD does not contain the electrode surface oxidation peak for any scans and maintains a widened solvent window over multiple scans. This indicates that PF functionalization is relatively stable against oxidation, as will be discussed below.

The background current regions (0 to +1 V) for several CVs shown in Figure 2.16. PF-BDD exhibits an order of magnitude (over 10×) *lower* background current than H-BDD and O-BDD, which are themselves similar. This is an interesting result because low background currents are desirable for electrochemical sensing, and though BDD is known to yield low background current, [22] PF functionalization decreases it further. Background currents for each electrode type change minimally after 30-min electrolyses, indicating that electrode fouling with organic byproducts plays little role in changing performance (discussed below).

2.3.5 Changes in BDD surface functionalization during electrolysis.

To understand how the chemical nature of BDD surfaces change during electrolysis, we used XPS and quantified the areas for the C(1s), F(1s), and O(1s) peaks. Figure 2.17 shows representative spectra used in this analysis. Using these areas and the associated sensitivity factors, we determined the fraction of each element before and after 30 min electrolysis at 2.7 V vs. SHE (also after 24 hr for PF-BDD only), yielding the data in Figure 2.6.

Freshly prepared H-BDD and PF-BDD contain minimal (< 1%) surface oxygen content, whereas O-BDD contains 9.0 (± 1.1)% oxygen (Figure 2.6A). Electrolysis of H-BDD transforms its surface to become similar to, yet distinguishable from, that of O-BDD. After only a 30-min electrolysis, H-BDD becomes oxidized, showing higher surface oxygen content than O-BDD (Figure 2.6A). That is, the electrochemical oxidation route produces a larger fraction of surface oxygen than the chemical oxidation route (H_2O_2/UV). Some insights into the nature of the oxidized sites can be gleaned from the presence of a Na(1s) peak near 1068 eV in the XPS spectrum of H-BDD after electrolysis (Figure 2.18) Goeting et al.[34] observed a similar peak on oxidized BDD via XPS and attributed it to Na^+ bonded to deprotonated carboxylate groups. Since Na^+ is a component of our electrolyte and we detect it via XPS without detecting a significant P(2p) peak (thereby ruling out the presence of sodium phosphate species), we believe the Na we observe is associated with carboxylate groups formed during electrolysis. Notably, the XPS spectrum of an O-BDD sample that has been placed in the same Na^+-containing buffer for the same length of time as the electrolyte (Figure 2.18) exhibits a negligible Na(1s) peak. Prior studies have shown that electrochemical oxidation of H-BDD yields a mixture of different oxygen-containing functional groups including alcohols, ethers, and carboxylic acids.[30-34] Under the conditions of our experiments, electrochemical oxidation of H-BDD produces more total oxygen and more carboxylate groups than did H_2O_2/UV treatment.

The F(1s) data in Figure 2.6B show loss of F content on the PF-BDD samples upon electrolysis, consistent with a prior electrochemical study of BDD terminated directly with F atoms.[59] In addition, Figure

2.6A shows that the O(1s) content of PF-BDD increases with electrolysis time. These changes indicate partial removal of surface-attached PF molecules or molecular fragments from BDD and subsequent oxidation of surface C–H_X groups to form oxygen-containing functional groups during electrolysis. In our system, loss of F can in principle arise from either (1) individual fluorine atom abstraction by ·OH or (2) removal of ligands by cleavage of C–C bonds. Prior work on the oxidation of fluorinated surfactants by ·OH and other species reported that completely perfluorinated chains were inert to such chemical oxidation, while molecules that were only partially fluorinated were degraded into shorter fluorinated alcohols via C–C bond cleavage.[60] The molecules we use in our studies are completely fluorinated except for the terminal alkene group bonded to the surface. Thus, we believe that loss of F most likely arises from ·OH radicals attacking the –H_2C–CH_2– group immediately adjacent to the diamond surface and removing ligands from the surface. Once perfluorinated ligands are removed during electrolysis, exposed C_{diamond}–H groups at the diamond surface (see Figure 2.1C) can be oxidized via H atom abstraction followed by reaction with water.[61] Even though electrolysis induces loss of F and surface oxidation, the oxygen content of a PF-BDD surface after 30 min is much lower than that for H-BDD. Even after 24 hr of electrolysis the surface oxygen content of PF-BDD is less than that of H-BDD used for only 30 min. From this we conclude that PF-BDD is significantly more resistant to oxidation than H-BDD under our experimental conditions, due to the protective monolayer. Overall, these XPS results are fully consistent with our CV results above, since H-BDD and O-BDD exhibit surface oxidation peaks and PF-BDD does not.

Contact angles represent one way to characterize changes in diamond surface functionalization and associated properties such as hydrophobic character.[33, 38, 62-64] Figure 2.7 shows contact angle data for functionalized samples before and after 30-min electrolyses at 2.7 V vs. SHE (representative images found in Figure 2.19). The contact angle for O-BDD after electrolysis (data not shown) is very similar to O-BDD before electrolysis. As expected, the initial contact angles are in the order O-BDD < H-BDD < PF-BDD. After electrolysis, the contact angles for PF-BDD and for H-BDD both decrease. However, the value for

PF-BDD still remains higher than for the other surfaces; this is consistent with the XPS data indicating that PF-BDD is more resistant to oxidation compared with H-BDD.

We also found that PF-BDD samples that were immersed in electrolyte without undergoing any electrolysis also underwent a small decrease in contact angle compared to the initial surface. Time-dependent chronoamperometry experiments (Figure 2.20) reveal that PF-BDD exhibits an increase in electrolytic current over the first several minutes. The contact angle and chronoamperometry results together suggest that within several minutes after immersion, water molecules partially intercalate into the perfluorinated film of the PF-BDD surface. This intercalation, in addition to oxidation, may contribute to the increase in O(1s) emission observed in XPS after electrolysis of the PF-BDD sample (Figure 2.5A).[59]

2.3.6 Changes in ·OH and O_2 formation with electrode use.

To determine how changes in the surface of BDD electrodes affect electrochemical performance, we examined HTPA production from PF-BDD and H-BDD samples during three sequential 30-min electrolyses, and from a 30-min electrolysis at the end of an extended (24 hr) electrolysis for PF-BDD as a long-term (“LT”) control. In each case, TPA was added to the cell at the beginning of the 30-min period under investigation. Example current vs. time plots are in Figure 2.20. From these measurements, we extracted the HTPA production rate, the total electrolytic current and the Faradaic efficiency for HTPA production (Figures 2.8A-C, respectively).

Figure 2.8A shows that the HTPA production rate does not change significantly with electrode use. The HTPA production rate did not differ significantly ($p > 0.05$) between the multiple time points for H-BDD or PF-BDD except after 24 hr for PF-BDD. This is surprising, given that Figures 2.6 and 2.7 show that the surface termination changes significantly with use over this period. These results suggest that the rate of ·OH production, as measured by the increase in HPTA concentration, does not depend strongly on surface termination. To confirm that the HTPA we detected arose from electrochemical processes, we conducted an open-circuit control in the same manner as all electrolyses, except without an applied potential. The resulting HTPA detected in this control experiment (Figure 2.8A, “OC”) is indistinguishable from the background, confirming that HTPA in other experiments is generated electrochemically.

While Figure 2.8A shows that the HTPA production rate does not change significantly with time, Figure 2.8B shows that the electrolytic current for PF-BDD increases over multiple electrolyses, approaching the relatively constant electrolytic current of H-BDD. Consequently, as the electrolytic current of PF-BDD increases with use, the efficiency of HTPA production (Figure 2.8C) decreases and approaches that of H-BDD. These results further indicate that functionalization of diamond with hydrophobic ligands enhances the efficiency of ·OH production by inhibiting O_2 formation, and not by directly increasing ·OH production rate. Moreover, even though the PF ligands may degrade, the efficiency for ·OH production on PF-BDD remains higher than that of either H-BDD or O-BDD for multiple 30-min electrolyses. We also note that the electrolytic current for H-BDD after multiple electrolyses is still much lower than that of O-BDD, despite showing similar surface oxygen fractions (Figure 2.6A) and contact angles (Figure 2.7A). These results suggest that while H-BDD may become oxidized with use, the precise identity of the oxygen functional groups on the surface impact the O_2 formation rate, and these functional groups depend on sample history.

2.3.7 Mechanistic insights into reactions on BDD surfaces.

Our results show that the total electrolytic current is strongly dependent on the surface functionalization and increases in the order PF-BDD < E-BDD < H-BDD < O-BDD. In contrast, formation of ·OH remains relatively constant across the different surface functionalizations. Based on these observations, we conclude that the primary way PF functionalization increases the efficiency of ·OH production is by reducing the rate of the competing reaction, production of O_2.

While the precise nature of the surface sites needed to form ·OH and O_2 are unknown, we draw on recent computational studies investigating water oxidation on metal oxides.[25] Based on that work, we conjecture that the four elementary steps in O_2 formation on diamond may be:

$$\text{C–OH} \rightarrow \text{C–O} + H^+ + e^- \qquad (2.2)$$

$$C–O + H_2O \rightarrow C–OOH \text{ (hydroperoxy)} + H^+ + e^- \qquad (2.3)$$

$$C–OOH \rightarrow C\cdot \text{ (surface radical)} + O_2 + H^+ + e^- \qquad (2.4)$$

$$C\cdot + H_2O \rightarrow C–OH + H^+ + e^- \qquad (2.5)$$

In this model, an oxidized surface site, such as a surface C–OH group, acts as an inner-sphere site for O_2 production. We note that Eq. 2.2 is not a simple alcohol deprotonation but is an electrochemically driven deprotonation to form a species akin to an adsorbed OH radical. On H-BDD, a well-terminated surface initially has few C–OH sites and therefore almost no sites for O_2 formation. However, such sites can be formed *in situ*, as ·OH radicals that are formed (by an outer-sphere process) can abstract H atoms from surface C–H groups, leaving behind C "dangling bonds" that can then react with water, leading to gradual oxidation of the surface.[61] This initiation process can be described by Eq. 2.6 and 2.7 below:

$$C–H + \cdot OH \rightarrow C\cdot \text{ (surface radical)} + H_2O \qquad (2.6)$$

$$C\cdot + H_2O \rightarrow C–OH + H^+ + e^- \qquad (2.7)$$

By a similar argument, we propose that PF-BDD yields even lower electrolytic current (i.e., less O_2) by performing two essential functions: (1) the hydrophobic PF ligands block water molecules from approaching the diamond surface by providing less favorable intermolecular interactions and steric hindrance, and (2) the PF ligands act as a diffusion barrier that reduces the ability of ·OH radicals to reach the diamond surface. Both properties must contribute, as our experiments with E-BDD (a more hydrophilic monolayer that still acts as a diffusion barrier) yielded a Faradaic efficiency for HTPA production moderately improved compared to O-BDD, but significantly less than that for PF-BDD (Figure 2.3). The same properties (hydrophobicity and diffusion barrier) likely give PF-BDD the widest solvent potential window (Figure 2.55) and lowest background current (Figure 2.16) of all tested electrodes. These electrochemical characteristics make functionalization of BDD with hydrophobic ligands not only promising for enhanced ·OH generation efficiency, but also for electrochemical sensing applications. The particular PF ligand we used has C–H species at the terminal alkene group (near the diamond interface) that may be a site for attack by ·OH, leading to eventual degradation and loss of the PF layer.

Our arguments that hydrophobic molecular layers inhibit inner-sphere reactions are supported by two prior studies. Gayen et al.[43] showed that hydrophobic, perfluorinated monolayer on BDD blocked ClO_3^- from reaching the electrode surface, while still allowing for ·OH formation.[43] Zhao, et al. also reported that modification of PbO_2 anodes with hydrophobic fluorine resin increased oxygen evolution overpotential and thereby increased ·OH production efficiency.[17] Taken together, they suggest that the use of hydrophobic layers to inhibit inner-sphere reactions in aqueous media may be a general phenomenon.

The independence of ·OH generation to BDD surface functionalization is similar to the behavior observed for other redox couples that undergo characteristic outer-sphere electron-transfer reactions (e.g., $Ru(NH_3)_6^{3+/2+}$).[22, 65, 66] In our case, an outer-sphere reaction indicates that ·OH forms from oxidation in solution near the electrode surface, without any direct bond formation to the surface. In addition, we found ·OH production to decrease at higher pH, indicating that ·OH is formed from H_2O and not OH^-. Therefore, we propose that ·OH radicals are formed via an outer-sphere oxidation of H_2O to the H_2O^+ intermediate, which then decomposes to ·OH and H^+:

$$H_2O \rightarrow H_2O^+ + e^- \tag{2.8}$$

$$H_2O^+ \rightarrow \cdot OH + H^+ \tag{2.9}$$

Previous studies of plasmas formed in water have demonstrated the presence of H_2O^+.[67] Previous studies on radiolytic[68, 69] and electrolytic[70] water oxidation phase have proposed H_2O^+ as an intermediate that decays through Eq. 2.9.[70] The outer-sphere pathway given by Eq. 2.8 must allow H_2O to approach sufficiently close to the BDD surface to initiate an electron-transfer process. Our contact angle, chronoamperometry, and XPS results all suggest that some water is able to penetrate into the molecular layer. These observations are consistent with previous molecular dynamics studies of molecular ligands on diamond surfaces[57] showing that because the packing density of molecules is not well lattice-matched to the density of surface C atoms, the molecular layers formed on diamond have increased structural disorder compared with, for example, self-assembled monolayers on gold. The increased disorder on diamond leads to layers in which the molecules have a high degree of conformational flexibility, opening gaps that allow water to penetrate closer to the surface than would be inferred from the static length of a stretched-out, static surface ligand. Water molecules that partially penetrate into the molecular layer can be oxidized in an outer-sphere process to produce ·OH radicals, which can then either diffuse back into solution or penetrate all the way to the diamond surface to induce oxidation of residual C–H sites. The resulting oxidized sites likely play a role in the inner-sphere oxidation of water to O_2.

2.4 Conclusions.

The primary conclusions drawn from this study can be summarized as follows. First, oxygen evolution and ·OH production under our experimental conditions both arise from oxidation of H_2O and not OH^-. Second, ·OH production on BDD does not depend strongly on surface termination, indicating that ·OH production occurs via an outer-sphere electron-transfer process. Third, oxygen evolution on BDD varies strongly with surface functionalization. Finally, hydrophobic surface ligands protect the underlying, unreacted C-H sites from attack by hydroxyl radicals and/or other chemically reactive species.

A key aspect of our work is that formation of ·OH can be accomplished by a one-electron oxidation of H_2O, as illustrated in Eq. 2.8 and 2.9. In contrast, formation of O_2 involves a more complex, four-electron process that necessarily has a more complex pathway involving multiple, sequential electron-transfer steps, like those indicated in Eq. 2.2-2.5.[25] As a result, formation of O_2 is disfavored by the absence of surface functional groups (such as C–OH) that can form the necessary intermediates.[25] Functionalization of the surface with strongly hydrophobic ligands reduce the number of surface sites that are able to participate in inner-sphere reactions, while also creating a barrier region in which unfavorable intermolecular interactions block H_2O molecules from reaching surface active sites. The ligands may also have a protective effect, reducing the ability of ·OH radicals to directly attack the diamond surface, which could then create labile sites for inner-sphere processes.

This work suggests that the use of hydrophobic ligands may provide a general pathway toward increasing the efficiency of outer-sphere electron-transfer processes. Selective production of ·OH is of great interest because of the ability of this radical to mineralize organic contaminants and sterilize water, in processes generally referred to as Electrochemical Advanced Oxidation Processes.[7, 9-14, 71] Admittedly, the practical application of PF-BDD as an electrode for electrochemical water purification is unreasonable due to high cost, lack of scalability, and the potential toxicity of released polyfluorinated ligands. However, the ability to alter electrochemical kinetics to favor outer-sphere reactions has wider application in electrochemical synthesis and detection, as the ability to decrease formation of O_2 should facilitate enhanced efficiency for other electrochemical oxidation processes of soluble species that lie well beyond the 1.23 V stability limit of water. An excellent opportunity for future research lies in developing electrode materials that mimic the physical and electrochemical properties of our functionalized, boron-doped diamond, but that are cheaper, safer, and more scalable, such as a hydrophobic, conductive polymer of sp^3 hybridized carbon or a surface-terminated boron carbide.

2.5 Figures and supporting information.

2.5.1 Primary figures.

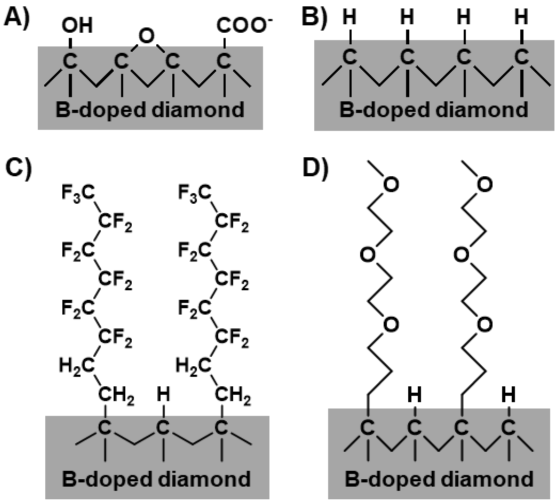

Figure 2.1. Schematic representations of surface functional groups for A) oxygen-terminated, B) hydrogen-terminated, C) 1,1,2-H-perfluoro-oct-1-ene-terminated, and D) allyloxy(diethylene oxide)-methyl-ether-terminated BDD.

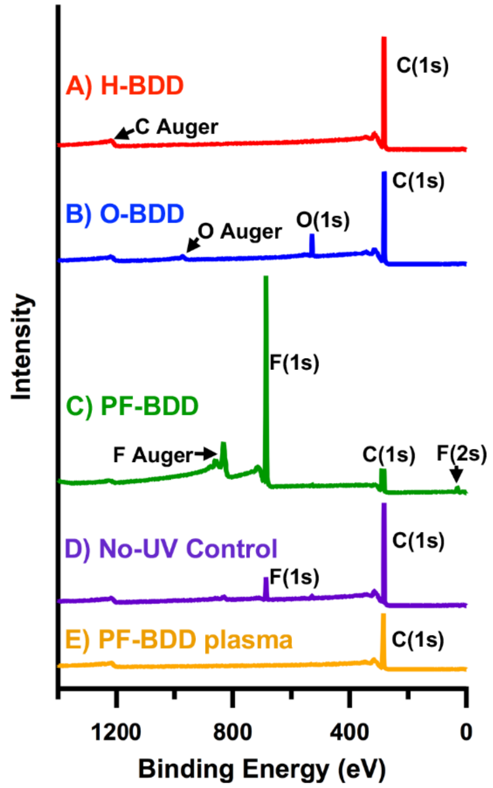

Figure 2.2. XPS spectra for A) H-BDD, B) O-BDD, C) PF-BDD, D) control sample exposed to PF without UV light, and E) PF-BDD after cleaning with H_2 plasma.

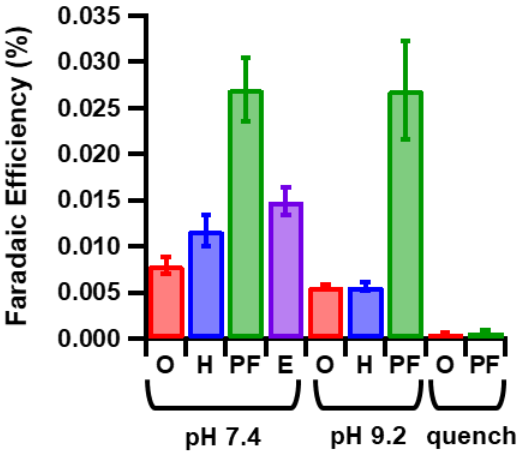

Figure 2.3. Faradaic efficiencies for formation of HTPA from functionalized diamond surfaces averaged over 30-min electrolyses at applied potential of 2.7 V vs. SHE. E-BDD was only tested at pH = 7.4. Quenched experiments were performed for O-BDD and PF-BDD at pH 7.4 by adding 0.3 M t-BuOH to the electrolyte.

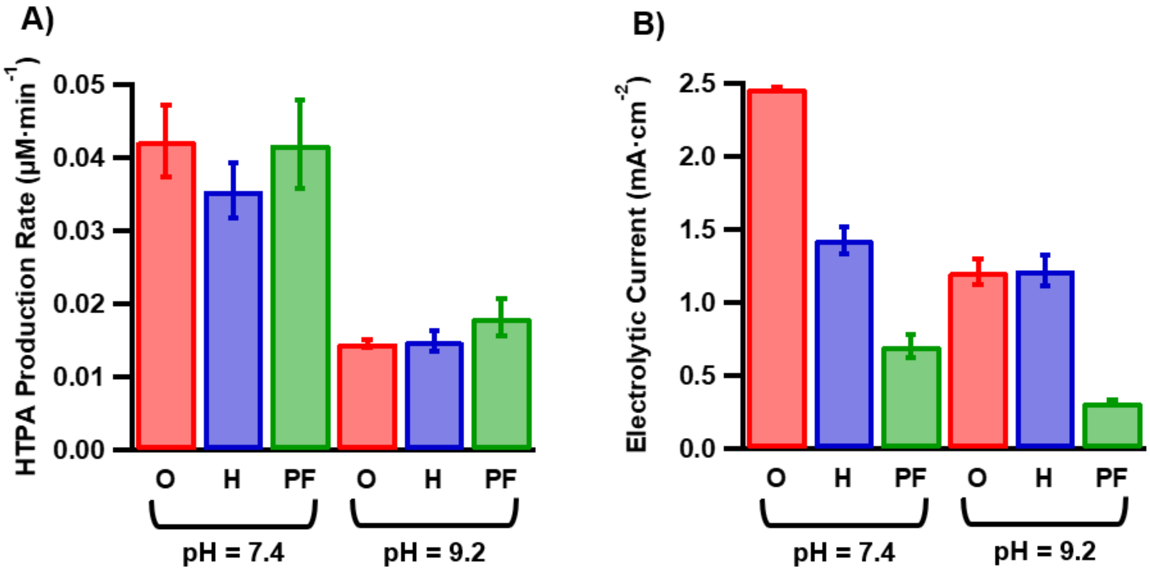

Figure 2.4. A) HTPA production rates and B) electrolytic currents for functionalized diamond surfaces averaged over 30-min electrolyses at applied potential of 2.7 V vs. SHE.

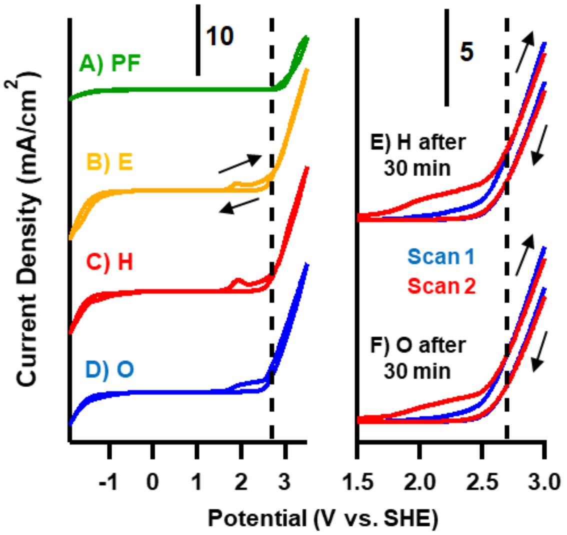

Figure 2.5. A-D) The first CV at 50 mV·s^{-1} for PF-, E-, H-, and O-BDD before electrolysis. E-F) The first and second scans for H- and O-BDD after a 30 min electrolysis. In both graphs, the dotted line corresponds to the potential at which all electrolyses are run (2.7 V). The arrows indicate the sweep direction, which is consistent in B-D.

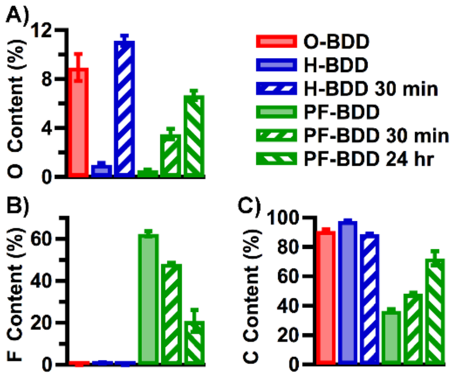

Figure 2.6. Surface content of A) oxygen, B) fluorine, and C) carbon for functionalized BDD surfaces. For H- and PF-terminated samples, the data are shown before (start) and after electrolysis for 30 min. For PF-BDD a sample is shown after 24 h continuous electrolysis. All samples held at 2.7 V vs. SHE.

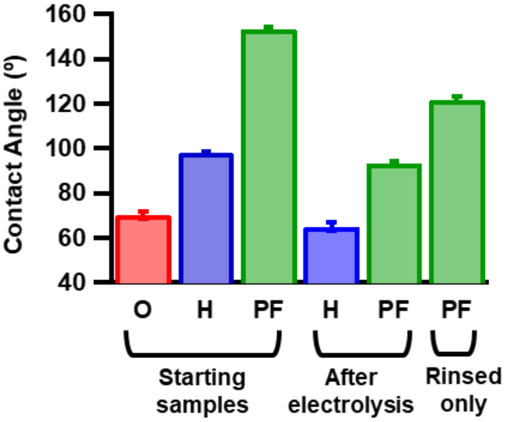

Figure 2.7. Contact angles for functionalized diamond surfaces interacting with water before and after 30-min electrolyses, and for PF-BDD samples rinsed with electrolyte (no electrolysis).

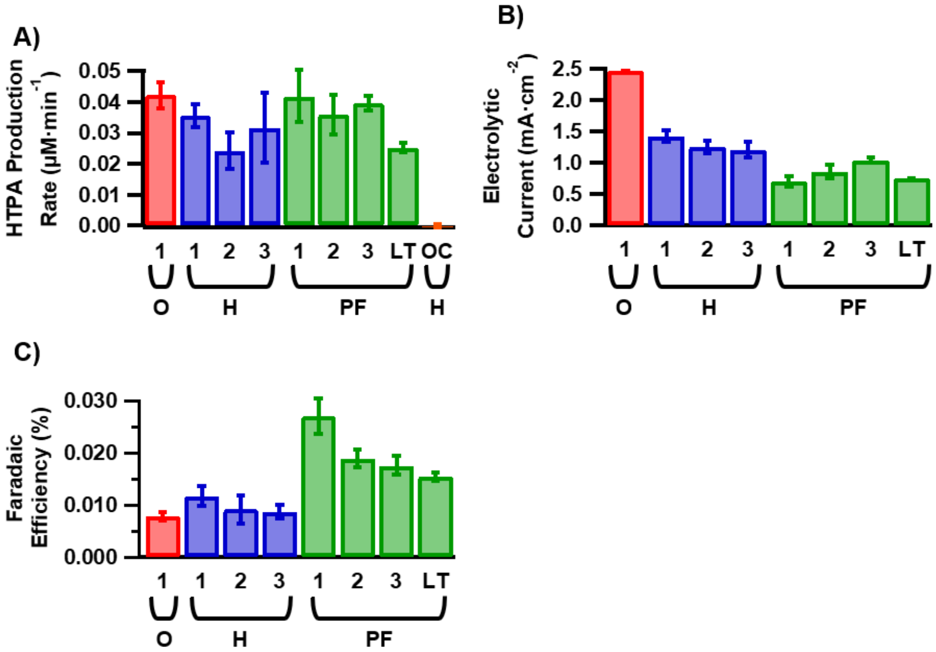

Figure 2.8. A) HTPA production rates, B) electrolytic currents, and C) Faradaic efficiencies for each of three, sequential 30-min electrolyses ("1-3", respectively) at applied potential of 2.7 V vs. SHE and pH 7.4 for functionalized BDD electrodes. The open-circuit 30 min control (OC) involves no applied potential. The "LT" (Long-Term) samples refer to 30-min electrolyses that were conducted on PF-BDD electrodes after 24 h continuous electrolysis at 2.7 V.

2.5.2 Supporting figures.

Table 2.1. Comparison of experimental results for PF-8 and PF-10 functionalized BDD electrodes.

Result	**PF-8**	**PF-10**	
Molecular surface coverage (molecule·nm^2)	12.9 ± 1.8	11.1 ± 0.8	
Initial contact angle (°)	153.6 ± 0.6	149.3 ± 0.4	
Contact angle after 30-min electrolysis (°)	93.4 ± 0.9	93.4 ± 2.1	
Initial Faradaic efficiency (%)	0.027 ± 0.003	0.024 ± 0.004	pH 7.4
Initial HTPA production rate (μM·min^{-1})	0.042 ± 0.008	0.031 ± 0.009	
Initial electrolytic current (mA·cm^2)	0.70 ± 0.08	0.56 ± 0.09	
Initial Faradaic efficiency (%)	0.026 ± 0.005	0.016 ± 0.002	pH 9.2
Initial HTPA production rate (μM·min^{-1})	0.018 ± 0.003	0.020 ± 0.003	
Initial electrolytic current (mA·cm^2)	0.32 ± 0.02	0.60 ± 0.09	
Faradaic efficiency pH 7.4 (%)	0.027 ± 0.003	0.024 ± 0.004	Three sequential
	0.019 ± 0.002	0.020 ± 0.003	
	0.18 ± 0.002	0.017 ± 0.004	
Faradaic efficiency pH 7.4 (%)	0.0155 ± 0.0008	0.009 ± 0.001	After 24 hr
HTPA production rate pH 7.4 (μM·min^{-1})	0.042 ± 0.008	0.031 ± 0.009	Three sequential
	0.036 ± 0.006	0.028 ± 0.004	
	0.040 ± 0.002	0.027 ± 0.001	
HTPA production rate pH 7.4 (μM·min^{-1})	0.025 ± 0.001	0.025 ± 0.004	After 24 hr
Electrolytic current pH 7.4 (mA·cm^2)	0.70 ± 0.08	0.56 ± 0.09	Three sequential
	0.86 ± 0.10	0.66 ± 0.09	
	1.05 ± 0.04	0.77 ± 0.14	
Electrolytic current pH 7.4 (mA·cm^2)	0.756 ± 0.004	1.21 ± 0.02	After 24 hr

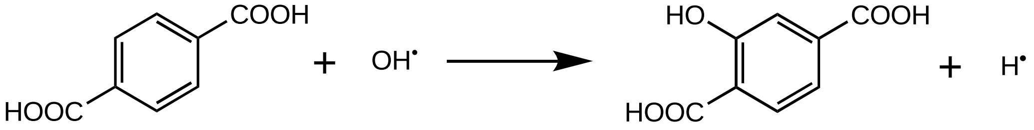

Scheme 2.1. Reaction of terephthalic acid (TPA) with the hydroxyl radical to produce 2-hydroxy-terephthalic acid (HTPA).

Table 2.2. Comparison of pseado-1st order rate constants for reactions of each species with ·OH, as calculated from approximate solution concentrations and literature[72] 2nd order rate constants.

Species	2nd Order k ($M^{-1}\cdot s^{-1}$)	Concentration (M)	Pseado-1st Order k' (s^{-1})	$k'_{TPA} : k'_{X}$
TPA	$3.3\cdot10^{9}$	$5.0\cdot10^{-4}$	$1.6\cdot10^{6}$	1.00
HPO_4^{2-}	$1.5\cdot10^{5}$	0.06	$9.0\cdot10^{3}$	183
$H_2PO_4^{-}$	$2.0\cdot10^{4}$	0.04	$8.0\cdot10^{2}$	2060
HTPA	$6.3\cdot10^{9}$	$1.0\cdot10^{-6}$	$6.3\cdot10^{3}$	262
OH^{-}	$1.2\cdot10^{10}$	$2.5\cdot10^{-7}$	$3.0\cdot10^{3}$	547

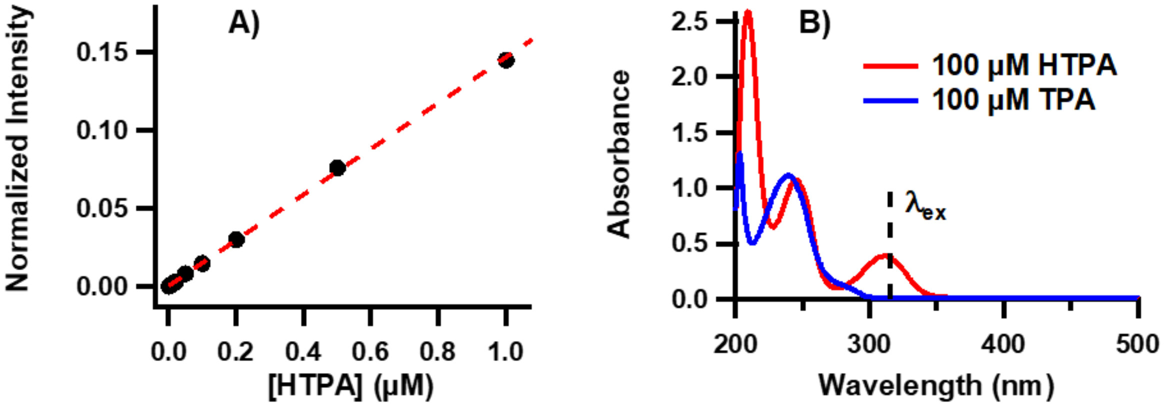

Figure 2.9. A) HTPA fluorescence calibration curve with linear fit of Y = (0.146 ± 0.001)X + 0.001, R^2 = 0.9994, and B) comparison of absorption spectra for 100 μM solutions of HTPA and TPA. This comparison is similar to that made by Page et al.[46] The excitation wavelength used in fluorescence experiments is 315 nm (shown), and the maximum emission wavelength is 422 nm.

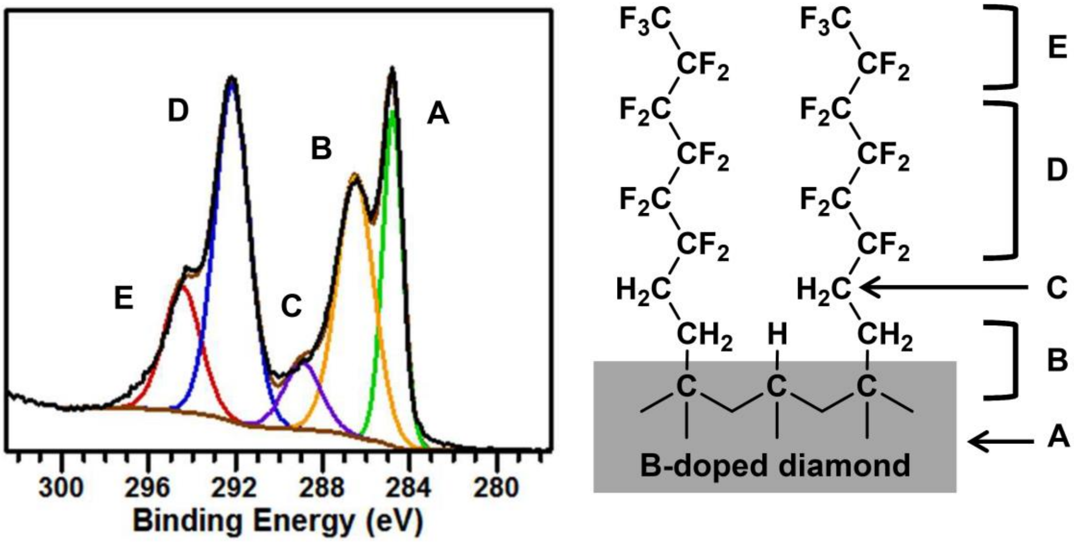

Figure 2.10. (left) Representative high-resolution C(1s) x-ray photoelectron spectrum for PF-8 functionalized boron-doped diamond (BDD) electrode (black trace) with five fit components (colored traces), and (right) assignments for each peak component.

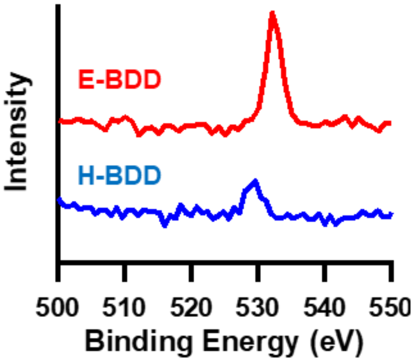

Figure 2.11. O(1s) region of XPS spectra for polyethylene-ether-functionalized (E-) and hydrogen-terminated (H-) BDD. Intensities are normalized to the C(1s) peak maxima. After functionalizing H-BDD with polyether ligands, intensity of the O(1s) peak greatly increases. Note that samples were stored under argon between treatment and analysis to prevent other possible forms of oxidation from producing such a peak.

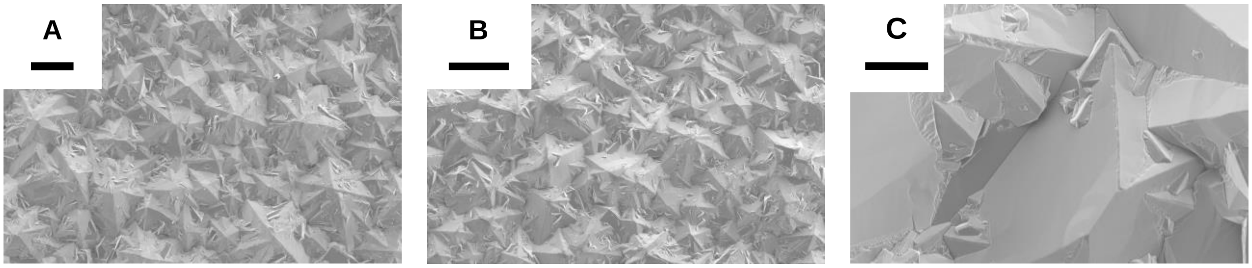

Figure 2.12. Scanning electron microscopy images for A) starting oxygen-terminated BDD (scale bar: 100 μm), B) BDD after functionalization and cleaning with H_2 plasma (scale bar: 100 μm), and C) enlargement of diamond crystals in image B (scale bar: 10 μm). There is no noticeable change in crystal morphology at these scales. Images were taken in out-of-lens secondary electron detection mode at an incident electron energy of 5 keV.

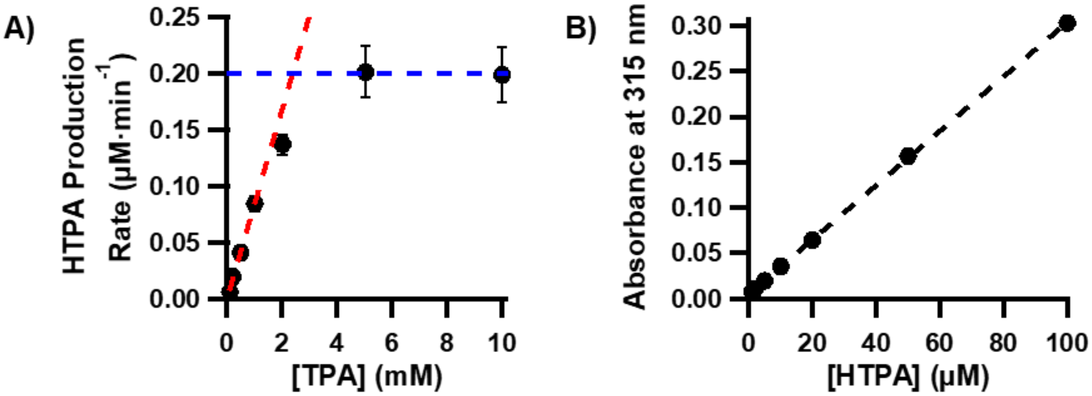

Figure 2.13. A) HTPA production rate as a function of [TPA] with a linear fit for the first four points of $y = 0.084x - 0.0003$, $R^2 = 0.9963$ and an approximate maximum of 0.2 $\mu M \cdot min^{-1}$. B) Absorbance of HTPA solutions at 315 nm as a function of [HTPA] within the concentration range relevant for 30-min electrolyses with linear fit of $y = 0.0030x + 0.0050$, $R^2 = 0.9999$. Absorbance of HTPA for all the tested concentrations is at baseline for wavelengths above ~350 nm.

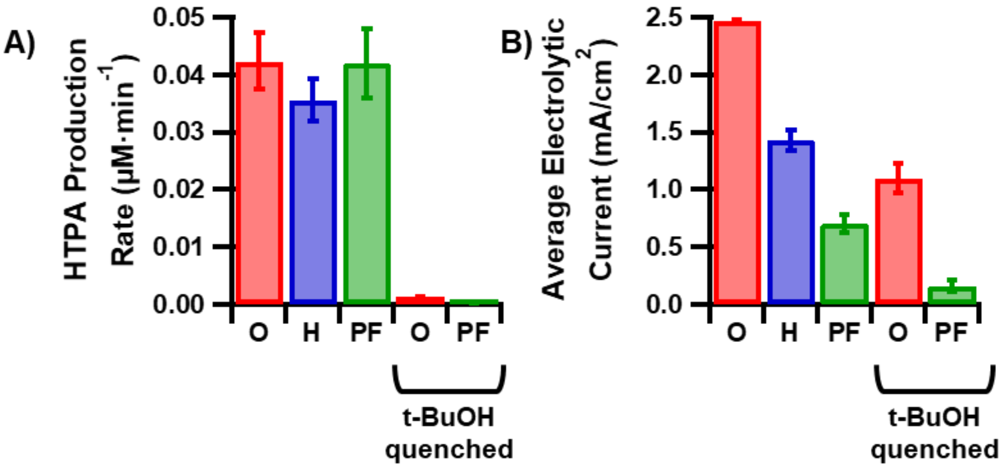

Figure 2.14. A) HTPA production rates and B) electrolytic currents for functionalized diamond surfaces averaged over 30-min electrolyses at applied potential of 2.7 V vs. SHE and pH = 7.4. Samples quenched with 0.3 M *t*-butanol (t-BuOH) in the electrolyte show a decrease in HTPA production to nearly zero due to ·OH scavenging by t-BuOH, and a modest decrease in electrolytic current. Note that 0.3 M t-BuOH was not detected to absorb light at any wavelength used in our fluorescence analysis.

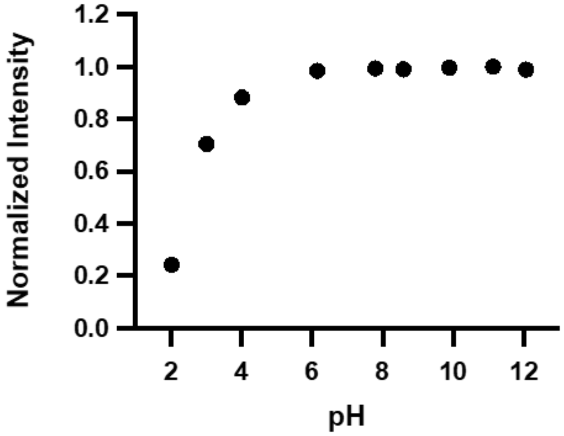

Figure 2.15. Fluorescence intensity of 1 μM HTPA in solutions of varying pH, normalized to the value of maximum intensity (pH 11.1) and corrected for dilutions. Error bars (not shown) lie within the width of the markers. Each solution pH is obtained through addition of 0.1 M HCl, 0.1 M KOH, or Na_2HPO_4/NaH_2PO_4 buffer. The starting HTPA solution was measured as pH = 6.15 ± 0.05. These results support those previously reported by Linxiang et al.[48]

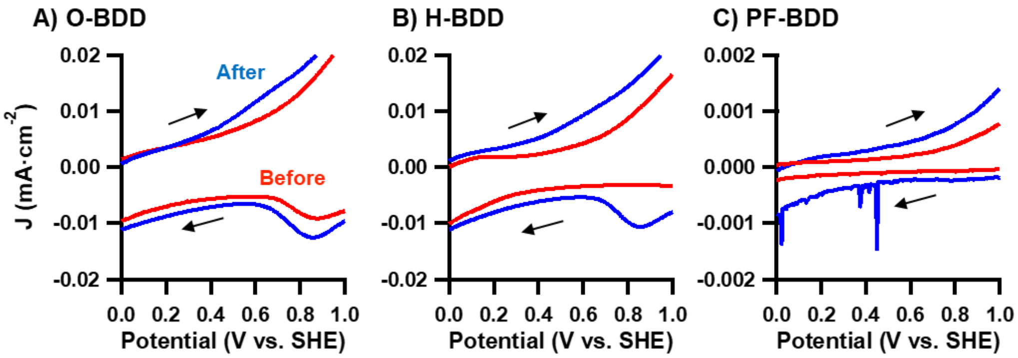

Figure 2.16. First scans of cyclic voltammograms before (red) and after (blue) electrolysis voltammograms at 50 mV·s^{-1} for A) O-BDD, B) H-BDD, and C) PF-BDD. Graphs are zoomed to show the background current region at low applied potentials. Note the difference in y-axis scale between A and B vs. C. Arrows show the sweep direction.

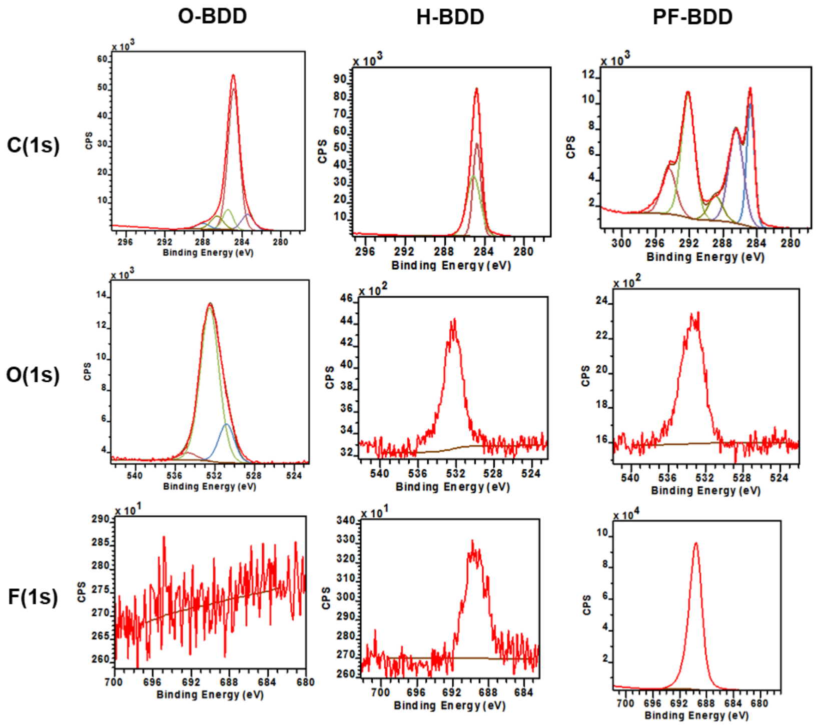

Figure 2.17. Representative high-resolution C(1s), O(1s), and F(1s) XPS spectra of O-BDD, H-BDD, and PF-BDD used for peak area quantification in Casa XPS Software. Some H-BDD samples (as the one pictured here) contained a weak F(1s) peak because individual samples were cleaned using a hydrogen plasma and reused.

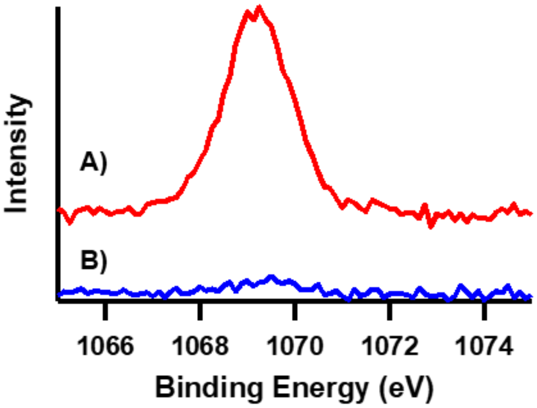

Figure 2.18. High-resolution XPS spectra of the Na(1s) region for A) H-BDD after 30-min electrolysis in pH 7.4 NaH_2PO_4/Na_2HPO_4 buffer and B) O-BDD after soaking in the same NaH_2PO_4/Na_2HPO_4 buffer for 30 min.

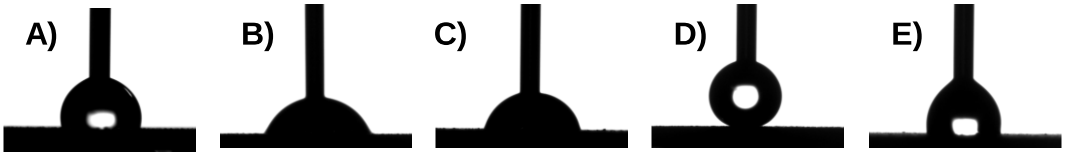

Figure 2.19. Representative needle-in water droplet contact angle images for A) H-BDD, B) H-BDD after 30-min electrolysis, C) O-BDD, D) PF-BDD, and E) PF-BDD after 30-min electrolysis.

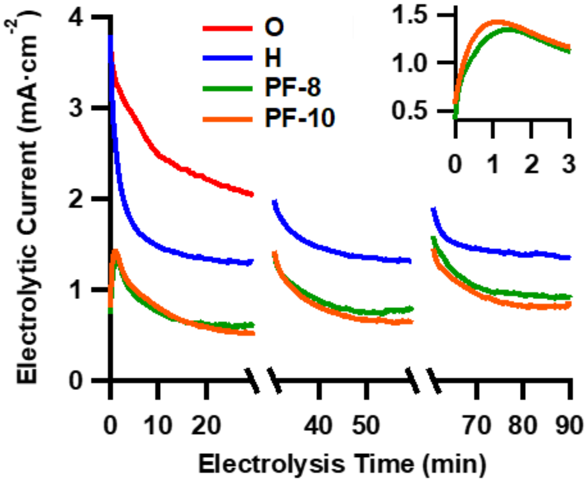

Figure 2.20. Representative current vs. time plots for individual electrodes of each type of functionalized BDD. Breaks in the x-axis indicate the beginning of a new, 30-min electrolysis. O-BDD was only tested once per electrode. The inset shows a peak in current for PF-8 and PF-10 BDD at the beginning of their first electrolyses only.

2.5.3 Fluorescence calibration and normalization procedures.

Emission spectra for 2-hydroxyterephthalic acid (HTPA) solutions were measured from 340 – 550 nm using an excitation wavelength (λ_{ex}) of 315 nm. The fluorescence spectrum exhibits a maximum at 422 nm (λ_{max}). Quantification of HTPA after electrolysis was conducted by subtracting the background signal of the starting TPA solution from the intensity at this wavelength and converting the resulting intensity to HTPA concentration using the calibration curve in Figure 2.9A. We made the calibration curve by measuring fluorescence intensities for nine solutions of varying concentration (2 nM to 1 μM) made by dissolving pure HTPA (TCI, 98.0%) in the same NaH_2PO_4/Na_2HPO_4 buffer (pH 7.4) used in electrochemical experiments. To account for instrumental variations between experiments, daily we normalized HTPA fluorescence intensities to that of an acrylic tetraphenylbutadiene standard (Starna Cells, λ_{ex} = 348 nm, λ_{max} = 418 nm). For both this standard and strongly fluorescent samples in the calibration, optical density filters were used to attenuate emitted light before detection by a photomultiplier tube. Typical measured HTPA concentrations of solutions after electrolysis range from 0.1 – 1 μM, which fall within the linear region of the calibration curve and are greater than the analytical limit of quantification (1.07 ± 0.12 nM) determined from the calibration data.

2.5.4 Surface coverage analysis.

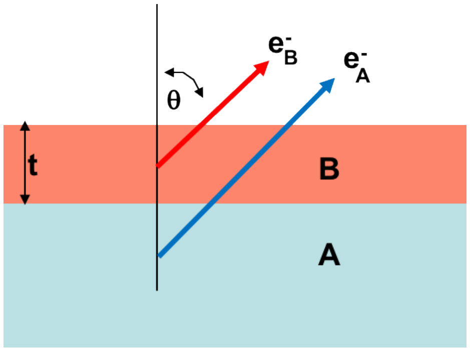

For a thin film of a material B covering an infinitely thick substrate A, the absolute coverage of B can be determined by using a peak from the substrate A as an internal standard (referred to here as Method 1) or by using a separate external sample (referred to here as Method 2). In both cases, the the measured XPS peak areas $Area_B$ and $Area_A$ can then be related to an effective film thickness t, taking into account inelastic scattering that occurs within both materials, yielding the following equation.

$$\frac{1-e^{-t/\lambda_{B,B}\cos\theta}}{e^{-t/\lambda_{A,B}\cos\theta}} = F(t) = \frac{Area_B\lambda_{A,A}\,\rho_A S_A}{Area_A\lambda_{B,B}\,\rho_B S_B} \tag{2.10}$$

where S_A and S_B refer to the atomic sensitivity factors associated with the species being measured, ρ_A and ρ_B refer to the density (atoms per volume) of the atomic species of interest in material A and B, and $\lambda_{X,Y}$ refers to the inelastic mean free path for electrons for element "X" passing through material "Y".

Method 1:

In the term on the far left, the exponential terms account for losses due to scattering of the substrate electrons and the overlayer electrons within the overlayer B. Due to the presence of two exponential terms this equation cannot be solved analytically but can be solved by plotting function F(t) as a function of assumed thickness *t* and finding the value of *t* at which F(t) equals the known value of the right-hand side of the equation. The total surface coverage of “B” (in atoms/area) is then equal to $\rho_B t$.

The expression on the far right-hand side contains known parameters such as the measured peak areas and sensitivity factors. The parameter ρ_B (density of the overlayer of material B) is generally not known precisely but can be approximated as the density of the solid “B” material. Note that choosing a value of ρ_B that is too high (for example) will yield a resulting effective thickness *t* that is too low, such that the product ρ_Bt remains relatively constant; thus, modest errors in the choice of density B results in self-compensating errors such that the total coverage in atoms per unit area, given by $\rho_B t$, is nearly constant.

Method 2:

A second method to measure the coverage is similar to the method above, but relies on having a second sample, measured in an identical geometry and with an identical x-ray intensity, to directly measure the unattenuated intensity of element A, $Area_{A,U}$. This approach avoids the need to need to measure the intensity from element A (in our experiment, the 284.8 eV C1s carbon peak) on the sample containing the molecular overlayer. This method is particularly advantageous when peaks originating from “A” and “B” overlap.

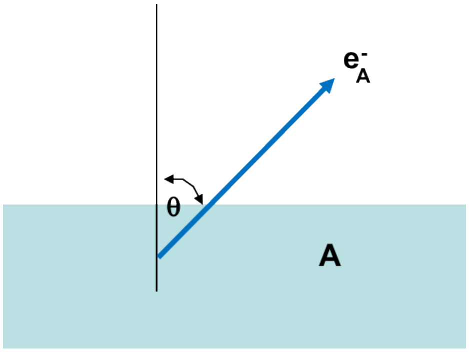

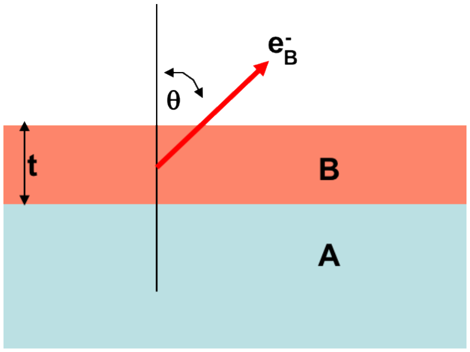

In this case, the analysis simplifies to:

$$1 - e^{-t/\lambda_{B,B}\cos\theta} = \frac{Area_B \lambda_{A,A}\, \rho_A S_A}{Area_{A,U}\, \lambda_{B,B}\, \rho_B S_B} \qquad (2.11)$$

or, rearranging

$$t = -\lambda_{B,B} cos\theta \ln\left(1 - \frac{Area_B \lambda_{A,A}\, \rho_A S_A}{Area_{A,U}\, \lambda_{B,B}\, \rho_B S_B}\right) \tag{2.12}$$

In both Method 1 and Method 2, the inelastic mean free paths can be estimated based on work of Tanuma, et al.[73] We use the inelastic mean free path for C(1s) electrons within diamond as $\lambda_{\mathrm{A,A}}$ = 1.9 nm. For C(1s) electrons passing through the PF film we used 2.0 nm, and for F(1s) electrons we used 1.42 nm, based on, electron kinetic energies $E_{k,C}$ = 1202 V for C(1s) and $E_{k,F}$ = 802 eV for fluorine, and the scaling relationship:[54]

$$\frac{\lambda_{C,B}}{\lambda_{F,B}} = \left(\frac{E_{k,C}}{E_{k,F}}\right)^{0.85} = \left(\frac{1200}{802}\right)^{0.85} \tag{2.13}$$

As a density for the molecular layer, we used a value of $4.38 \cdot 10^{22}$ F atoms·cm^{-3} based on a density of 1.7 g·cm^{-2} and a molecular weight of 438 g·mol^{-1} for perfluorooctane.[5] Using Method 1, we determined an effective thickness of 1.63 nm, leading to a coverage of 43 F atoms·nm^{-2} or 3.4 PF molecules·nm^{-2} (using the known stoichiometry of 13 F atoms per molecule). Using method 2 with a separate H-terminated sample as an internal standard, we obtained an effective thickness of 1.71 nm, yielding a value of value of 3.5 molecules·nm^{-2}. Because Method 2 avoids the need to deconvolute the C(1s) peaks, it is a more accurate; we therefore use the value of 3.5 molecules·nm^{-2}.

2.6 References.

1. Anson, C. W.; Stahl, S. S., Cooperative Electrocatalytic O_2 Reduction Involving Co(salophen) with p-Hydroquinone as an Electron-Proton Transfer Mediator. *J. Am. Chem. Soc.* **2017,** *139*, 18472-18475.

2. Kattel, S.; Liu, P.; Chen, J. G. G., Tuning Selectivity of CO_2 Hydrogenation Reactions at the Metal/Oxide Interface. *J. Am. Chem. Soc.* **2017,** *139*, 9739-9754.

3. McCreery, R. L., Advanced Carbon Electrode Materials for Molecular Electrochemistry. *Chem. Rev.* **2008,** *108*, 2646-2687.

4. Monroe, E. B.; Heien, M. L., Electrochemical Generation of Hydroxyl Radicals for Examining Protein Structure. *Anal. Chem.* **2013,** *85*, 6185-6189.

5. Roylance, J. J.; Kim, T. W.; Choi, K. S., Efficient and Selective Electrochemical and Photoelectrochemical Reduction of 5-Hydroxymethylfurfural to 2,5-Bis(hydroxymethyl)furan using Water as the Hydrogen Source. *ACS Catalysis* **2016,** *6*, 1840-1847.

6. Wang, Y. H.; Pegis, M. L.; Mayer, J. M.; Stahl, S. S., Molecular Cobalt Catalysts for O_2 Reduction: Low-Overpotential Production of H_2O_2 and Comparison with Iron-Based Catalysts. *J. Am. Chem. Soc.* **2017,** *139*, 16458-16461.

7. Chaplin, B. P.; Schrader, G.; Farrell, J., Electrochemical Destruction of N -Nitrosodimethylamine in Reverse Osmosis Concentrates using Boron-doped Diamond Film Electrodes. *Environ. Sci. Tech.* **2010,** *44*, 4264-4269.

8. Gligorovski, S.; Strekowski, R.; Barbati, S.; Vione, D., Environmental Implications of Hydroxyl Radicals (•OH). *Chem. Rev.* **2015,** *115*, 13051-13092.

9. Chaplin, B. P., Critical Review of Electrochemical Advanced Oxidation Processes for Water Treatment Applications. *Environ. Sci.: Processes and Impacts* **2014,** *16*, 1182-1203.

10. Sirés, I.; Brillas, E.; Oturan, M. A.; Rodrigo, M. A.; Panizza, M., Electrochemical Advanced Oxidation Processes: Today and Tomorrow. A Review. *Environ. Sci.& Poll. Res.* **2014,** *21*, 8336-8367.

11. Moreira, F. C.; Boaventura, R. A. R.; Brillas, E.; Vilar, V. J. P., Electrochemical Advanced Oxidation Processes: A Review on their Application to Synthetic and Real Wastewaters. *Appl. Cat. B: Environ.* **2017,** *202*, 217-261.

12. Enache, T. A.; Chiorcea-Paquim, A.-M.; Fatibello-Filho, O.; Oliveira-Brett, A. M., Hydroxyl Radicals Electrochemically Generated in situ on a Boron-doped Diamond Electrode. *Electrochem. Comm.* **2009,** *11*, 1342-1345.

13. Marselli, B.; Garcia-Gomez, J.; Michaud, P.; Rodrigo, M. A.; Comninellis, C., Electrogeneration of Hydroxyl Radicals on Boron-Doped Diamond Electrodes. *J. Electrochem. Soc.* **2003,** *150*, D79-D83.

14. Michaud, P.; Panizza, M.; Ouattara, L.; Diaco, T.; Fóti, G.; Comninellis, C., Electrochemical Oxidation of Water on Synthetic Boron-doped Diamond Thin Film Anodes. *J. Appl. Electrochem.* **2003,** *33*, 151-154.

15. Zhao, G.; Cui, X.; Liu, M.; Li, P.; Zhang, Y.; Cao, T.; Li, H.; Lei, Y.; Liu, L.; Li, D., Electrochemical Degradation of Refractory Pollutant Using a Novel Microstructured TiO_2 Nanotubes/Sb-doped SnO_2 Electrode. *Environ. Sci. Tech.* **2009,** *43*, 1480-1486.

16. Martinez-Huitle, C. A.; Quiroz, M. A.; Comninellis, C.; Ferro, S.; De Battisti, A., Hydroxyl Radicals Electrochemically Generated in situ on a Boron-doped Diamond Electrode. *Electrochimica Acta* **2004,** *50*, 949-956.

17. Zhao, G.; Zhang, Y.; Lei, Y.; Baoying, L. V.; Gao, J.; Zhang, Y.; Li, D., Fabrication and Electrochemical Treatment Application of a Novel Lead Dioxide Anode with Superhydrophobic Surfaces, High Oxygen Evolution Potential, and Oxidation Capability. *Environ. Sci. Tech.* **2010,** *44*, 1754-1759.

18. Bejan, D.; Guinea, E.; Bunce, N. J., On the Nature of the Hydroxyl Radicals Produced at Boron-doped Diamond and Ebonex Anodes. *Electrochimica Acta* **2012,** *69*, 275-281.

19. Macpherson, J. V., A Practical Guide to Using Boron Doped Diamond in Electrochemical Research. *Phys. Chem. Chem. Phys.* **2015,** *17*, 2935-2949.

20. Kapalka, A.; Fóti, G.; Comninellis, C., Determination of the Tafel Slope for Oxygen Evolution on Boron-doped Diamond Electrodes. *Electrochem. Comm.* **2008,** *10*, 607-610.

21. Garcia-Osorio, D. A.; Jaimes, R.; Vazquez-Arenas, J.; Lara, R. H.; Alvarez-Ramirez, J., The Kinetic Parameters of the Oxygen Evolution Reaction (OER) Calculated on Inactive Anodes via EIS Transfer Functions: •OH Formation. *J. Electrochem. Soc.* **2017,** *164*, E3321-E3328.

22. Fischer, A. E.; Show, Y.; Swain, G. M., Electrochemical Performance of Diamond Thin-Film Electrodes from Different Commercial Sources. *Anal. Chem.* **2004,** *76*, 2553-2560.

23. Einaga, Y., Diamond Electrodes for Electrochemical Analysis. *J. Appl. Electrochem.* **2010,** *40*, 1807-1816.

24. Salazar-Gastélum, M. I.; Lin, S. W.; Pina-Luis, G. E.; Pérez-Sicairos, S.; Félix-Navarro, R. M., Electrochemical and Spectrometric Studies for the Determination of the Mechanism of Oxygen Evolution Reaction. *J. Electrochem. Soc.* **2016,** *163*, G37-G43.

25. Siahrostami, S.; Li, G. L.; Viswanathan, V.; Nørskov, J. K., One- or Two-Electron Water Oxidation, Hydroxyl Radical, or H_2O_2 Evolution. *J. Phys. Chem. Lett.* **2017,** *8*, 1157-1160.

26. Swain, G. M.; Ramesham, R., The Electrochemical Activity of Boron-doped Polycrystalline Diamond Thin-film Electrodes. *Anal. Chem.* **1993,** *65*, 345-351.

27. Granger, M. C.; Witek, M.; Xu, J. S.; Wang, J.; Hupert, M.; Hanks, A.; Koppang, M. D.; Butler, J. E.; Lucazeau, G.; Mermoux, M.; Strojek, J. W.; Swain, G. M., Standard Electrochemical Behavior of High-quality, Boron-doped Polycrystalline Diamond Thin-film Electrodes. *Anal. Chem.* **2000,** *72*, 3793-3804.

28. Petrini, D.; Larsson, K., Theoretical Study of the Thermodynamic and Kinetic Aspects of Terminated (111) Diamond Surfaces. *J. Phys. Chem. C* **2008,** *112*, 3018-3026.

29. Eckert, F.; Diedenhofen, M.; Klamt, A., Towards a First Principles Prediction of pKa: COSMO-RS and the Cluster-continuum Approach. *Mol. Phys.* **2010,** *108*, 229-241.

30. Girard, H.; Simon, N.; Ballutaud, D.; Herlem, M.; Etcheberry, A., Effect of Anodic and Cathodic Treatments on the Charge Transfer of Boron Doped Diamond Electrodes. *Diam. Relat. Mater.* **2007,** *16*, 316-325.

31. Wang, M.; Simon, N.; Charrier, G.; Bouttemy, M.; Etcheberry, A.; Li, M.; Boukherroub, R.; Szunerits, S., Distinction Between Surface Hydroxyl and Ether Groups on Boron-doped Diamond Electrodes Using a Chemical Approach. *Electrochem. Comm.* **2015,** *12*, 351-354.

32. Notsu, H.; Yagi, I.; Tatsuma, T.; Tryk, D. A.; Fujishima, A., Surface Carbonyl Groups on Oxidized Diamond Electrodes. *J. Electroanal. Chem.* **2000,** *492*, 31-37.

33. Hoffmann, R.; Kriele, A.; Obloh, H.; Hees, J.; Wolfer, M.; Smirnov, W.; Yang, N.; Nebel, C. E., Electrochemical Hydrogen Termination of Boron-doped Diamond. *Appl. Phys. Lett.* **2010,** *97*, 1-4.

34. Goeting, C. H.; Marken, F.; Gutiérrez-Sosa, A.; Compton, R. G.; Foord, J. S., Electrochemically Induced Surface Modifications of Boron-doped Diamond Electrodes: an X-ray Photoelectron Spectroscopy Study. *Diam. Relat. Mater.* **2000,** *9*, 390-396.

35. Kondo, T.; Ito, H.; Kusakabe, K.; Ohkawa, K.; Honda, K.; Einaga, Y.; Fujishima, A.; Kawai, T., Characterization and Electrochemical Properties of CF4 Plasma-treated Boron-doped Diamond Surfaces. *Diam. Relat. Mater.* **2008,** *17*, 48-54.

36. Mayrhofer, L.; Moras, G.; Mulakaluri, N.; Rajagopalan, S.; Stevens, P. A.; Moseler, M., Fluorine-Terminated Diamond Surfaces as Dense Dipole Lattices: The Electrostatic Origin of Polar Hydrophobicity. *J. Am. Chem. Soc.* **2016,** *138,* 4018-4028.

37. Siné, G.; Ouattara, L.; Panizza, M.; Comninellis, C., Electrochemical Behavior of Fluorinated Boron-Doped Diamond. *Electrochem. Solid-State Lett.* **2003,** *6*, D9-D11.

38. Salvadori, M. C.; Araujo, W. W. R.; Teixeira, F. S.; Cattani, M.; Pasquarelli, A.; Oks, E. M.; Brown, I. G., Termination of Diamond Surfaces with Hydrogen, Oxygen and Fluorine using a Small, Simple Plasma Gun. *Diam. Relat. Mater.* **2010,** *19*, 324-328.

39. Jawando, W.; Gayen, P.; Chaplin, B. P., The Effects of Surface Oxidation and Fluorination of Boron-doped Diamond Anodes on Perchlorate Formation and Organic Compound Oxidation. *Electrochimica Acta* **2015,** *174*, 1067-1078.

40. Popov, C.; Kulisch, W.; Bliznakov, S.; Ceccone, G.; Gilliland, D.; Sirghi, L.; Rossi, F., Surface Modification of Nanocrystalline Diamond/Amorphous Carbon Composite Films. *Diam. Relat. Mater.* **2008,** *17*, 1229-1234.

41. Guan, B.; Zhi, J.; Zhang, X.; Murakami, T.; Fujishima, A., Electrochemical Route for Fluorinated Modification of Boron-doped Diamond Surface with Perfluorooctanoic Acid. *Electrochem. Comm.* **2007,** *9*, 2817-2821.

42. Foord, J. S.; Singh, N. K.; Jackman, R. B.; Gutiérrez-Sosa, A.; Proffitt, S.; Holt, K. B., Reactions of Xenon Difluoride and Atomic Hydrogen at Chemical Vapour Deposited Diamond Surfaces. *Surf. Sci.* **2001,** *488*, 335-345.

43. Gayen, P.; Chaplin, B. P., Fluorination of Boron-Doped Diamond Film Electrodes for Minimization of Perchlorate Formation. *Appl. Mater. Interfaces* **2017**, *9*, 27638–27648.

44. Harris, S. J.; Belton, D. N., Thermochemistry on a Fluorinated Diamond(111) Surface. *Appl. Phys. Lett.* **1991,** *59*, 1949-1951.

45. Saran, M.; Summer, K. H., Assaying for Hydroxyl Radicals: Hydroxylated Terephthalate is a Superior Fluorescence Marker than Hydroxylated Benzoate. *Free Radical Res.* **1999,** *31*, 429-36.

46. Page, S. E.; Arnold, W. A.; McNeill, K., Terephthalate as a Probe for Photochemically Generated Hydroxyl Radical. *J. Environ. Monitoring* **2010,** *12*, 1658-1665.

47. Matthews, R. W., The Radiation Chemistry of the Terephthalate Dosimeter. *Radiation Res.* **1980,** *83*, 27-41.

48. Linxiang, L.; Abe, Y.; Nagasawa, Y.; Kudo, R.; Usui, N.; Imai, K.; Mashino, T.; Mochizuki, M.; Miyata, N., An HPLC Assay of Hydroxyl Radicals by the Hydroxylation Reaction of Terephthalic Acid. *Biomed. Chrom.* **2004,** *18*, 470-474.

49. Strother, T.; Knickerbocker, T.; Russell, J. N.; Butler, J. E.; Smith, L. M.; Hamers, R. J., Photochemical Functionalization of Diamond Films. *Langmuir* **2002,** *18*, 968-971.

50. Nichols, B. M.; Butler, J. E.; Russell, J. N.; Hamers, R. J., Photochemical Functionalization of Hydrogen-terminated Diamond Surfaces: A Structural and Mechanistic Study. *J. Phys. Chem. B* **2005,** *109*, 20938-20947.

51. Colavita, P. E.; Streifer, J. A.; Sun, B.; Wang, X.; Warf, P.; Hamers, R. J., Enhancement of Photochemical Grafting of Terminal Alkenes at Surfaces via Molecular Mediators: The Role of Surface-Bound Electron Acceptors. *J. Phys. Chem. C* **2008,** *112*, 5102-5112.

52. Shirley, D. A., High-resolution X-ray Photoemission Spectrum of the Valence Bands of Gold. *Phys. Rev. B* **1972,** *5*, 4709-4714.

53. Jing, Y.; Chaplin, B. P., A Mechanistic Study of the Validity of Using Hydroxyl Radical Probes to Characterize Electrochemical Advanced Oxidation Processes. *Environ. Sci. Tech.* **2017,** *51*, 2355-2365.

54. Starkweather, H. W., Melting and Crystalline Transitions in Normal Perfluoroalkanes and Poly(tetrafluoroethylene). *Macromol.* **1986,** *19*, 1131-1134.

55. Wang, X.; Colavita, P. E.; Streifer, J. A.; Butler, J. E.; Hamers, R. J., Photochemical Grafting of Alkenes onto Carbon Surfaces: Identifying the Roles of Electrons and Holes. *J. Phys. Chem.* **2010,** *114*, 4067-4074.

56. Wang, X.; Landis, E. C.; Franking, R.; Hamers, R. J., Surface Chemistry for Stable and Smart Molecular and Biomolecular Interfaces via Photochemical Grafting of Alkenes. *Acc. Chem. Res.* **2010,** *43*, 1205-1215.

57. Ruther, R. E.; Cui, Q.; Hamers, R. J., Conformational Disorder Enhances Electron Transfer Through Alkyl Monolayers: Ferrocene on Conductive Diamond. *J. Am. Chem. Soc.* **2013,** *135*, 5751-5761.

58. Barazesh, J. M.; Prasse, C.; Sedlak, D. L., Electrochemical Transformation of Trace Organic Contaminants in the Presence of Halide and Carbonate Ions. *Environ. Sci. Tech.* **2016,** *50*, 10143-10152.

59. Martin, H. B.; Argiotia, A.; Angus, J. C.; Landau, U., Voltammetry Studies of Single-Crystal and Polycrystalline Diamond Electrodes. *J. Electrochem. Soc.* **1999,** *146*, 2959.

60. Schroeder, H. F.; Meesters, R. J. W., Stability of Fluorinated Surfactants in Advanced Oxidation Processes — A Follow Up of Degradation Products Using Flow Injection – Mass Spectrometry, Liquid Chromatography – Mass Spectrometry and Liquid Chromatography – Multiple Stage Mass Spectrometry. *J. Chrom. A* **2005,** *1082*, 110-119.

61. Zhang, L. H.; Hamers, R. J., Photocatalytic Reduction of CO_2 to CO by Diamond Nanoparticles. *Diam. Relat. Mater.* **2017,** *78*, 24-30.

62. Ohashi, T.; Zhang, J.; Takasu, Y.; Sugimoto, W., Steam Activation of Boron Doped Diamond Electrodes. *Electrochimica Acta* **2011,** *56*, 5599-5604.

63. Liu, F. B.; Wang, J. D.; Liu, B.; Li, X. M.; Chen, D. R., Effect of Electronic Structures on Electrochemical Behaviors of Surface-terminated Boron-doped Diamond Film Electrodes. *Diam. Relat. Mater*. **2007,** *16*, 454-460.

64. Björkman, H.; Ericson, C.; Hjertén, S.; Hjort, K., Diamond Microchips for Fast Chromatography of Proteins. *Sensors and Actuators B* **2001,** *79*, 71-77.

65. Yagi, I.; Notsu, H.; Kondo, T.; Tryk, D. A.; Fujishima, A., Electrochemical Selectivity for Redox Systems at Oxygen-terminated Diamond Electrodes. *J.Electroanal. Chem.* **1999,** *473*, 173-178.

66. Hutton, L. A.; Iacobini, J. G.; Bitziou, E.; Channon, R. B.; Newton, M. E.; Macpherson, J. V., Examination of the Factors Affecting the Electrochemical Performance of Oxygen-Terminated Polycrystalline Boron-Doped Diamond Electrodes. *Anal. Chem* **2013,** *85*, 7230-7240.

67. Lew, H.; Heiber, I., Spectrum of H_2O^+. *J. Chem. Phys.* **1973,** *58*, 1246-1247.

68. Hochanadel, C. J., Effects of Cobalt γ-Radiation on Water and Aqueous Solutions. *J. Phys. Chem.* **1952,** *56*, 587-594.

69. Hart, E. J., The Radical Pair Yield of Ionizing Radiation in Aqueous Solutions of Formic Acid. *J. Phys. Chem.* **1952,** *56*, 594-599.

70. Joshi, A. A.; Locke, B. R.; Arce, P.; Finney, W. C., Formation of Hydroxyl Radicals, Hydrogen Peroxide and Aqueous Electrons by Pulsed Streamer Corona Discharge in Aqueous Solution. *J. Hazard. Mater*. **1995,** *41*, 3-30.

71. Chaplin, B. P.; Hubler, D. K.; Farrell, J., Understanding Anodic Wear at Boron Doped Diamond Film Electrodes. *Electrochimica Acta* **2013,** *89*, 122-131.

72. Buxton, G. V; Greenstock, C. L.; Helman, W. P.; Ross, A. B. *J.* Critical Review of Rate Constants for Reactions of Hydrated Electrons, Hydrogen Atoms and Hydroxyl Radicals in Aqueous Solution. *Phys. Chem. Ref. Data* **1988**, *17*, 513–886.

73. Tanuma, S.; Powell, C. J.; Penn, D. R. Calculations of Electron Inelastic Mean Free Paths. IX. Data for 41 Elemental Solids over the 50 eV to 30 keV Range. *Surf. Interface Anal.* **2011**, *43*, 689–713.

Chapter 3. Reciprocal Redox Interactions of Lithium Cobalt Oxide Nanoparticles with Nicotinamide Adenine Dinucleotide (NADH) and Glutathione (GSH): Toward a Mechanistic Understanding of Nanoparticle-Biological Interactions

The following chapter is adapted from the article published in *Environmental Science: Nano* 2021 (DOI: 10.1039/D0EN01221A), with the co-authors Elizabeth D. Laudadio, Jenny K. Hedlund Orbeck, Ali Abbaspour Tamijani, Khoi Nguyen L. Hoang, Sara E. Mason, Catherine J. Murphy, Z. Vivian Feng, and Robert J. Hamers. All of the data collection, data analysis, manuscript preparation, and revision were done by Austin H. Henke under the advisement of Robert J. Hamers except for the following: Elizabeth D. Laudadio and Jenny K. Hedlund Orbeck assisted with nanoparticle synthesis and characterization and manuscript preparation, Ali Abbaspour Tamijani and Sara E. Mason assisted with DFT calculations and data analysis/interpretation, Khoi Nguyen L. Hoang and Catherine J. Murphy assisted with TEM of $LiCoO_2$ nanomaterials, and Z. Vivian Feng assisted with statistical analysis and manuscript revision.

This work was supported by the National Science Foundation (NSF) under the Center for Sustainable Nanotechnology, CHE-2001611. The Center for Sustainable Nanotechnology is part of the NSF Centers for Chemical Innovation Program. The authors gratefully acknowledge use of University of Wisconsin facilities and instrumentation through the Research Science and Engineering Center (partially supported through NSF DMR-1720415) and Water Science and Engineering Laboratory. The authors also acknowledge Dr. Pamela Doolittle for assistance with ICP-MS measurements.

3.1 Introduction.

The interactions of nanomaterials with environmental and biological systems involve a complex suite of interaction mechanisms. While physical interactions can be important, many emerging nanoparticles of technological utility have chemical compositions that are reactive, leading to new mechanisms such as release of solubilized metals[1, 2] or surface-driven formation of reactive oxygen species. For example, nano-Ag(0) can be oxidized to Ag(I), which then has significant antimicrobial activity. Metal oxides constitute the most widely used class of engineered nanomaterials and are frequently used in high oxidation states, with the corresponding metal hydroxides having much lower solubility than those formed from the lower oxidation states. For example, at pH = 6, the solubility of $Fe(OH)_3$ is ~10^{-13} M while $Fe(OH)_2$ is highly soluble. Because of the low solubility of high-valence metals, redox-active small organic acids can enhance dissolution of metal oxides by reducing the metals to lower oxidation states,[3-7] and biologically-induced reduction processes impact biogeochemical cycling of metals such as Fe and Mn.[8-10] The interaction of biomolecular reducing agents with nanoparticles could induce biological impacts both by enhancing release of transition metals and by altering the cellular redox potential and associated homeostasis. Despite the critical role that redox chemistry plays in cellular homeostasis, the influence of specific biologically relevant electron transporters such as nicotinamide adenine dinucleotide (NADH) and glutathione (GSH) on the transformation of engineered nanoparticles has not been widely considered previously.

Among high-valence metal oxides, $LiCoO_2$ and a broader family of "NMC" compositions ($LiNi_xMn_yCo_{1-x-y}O_2$, $x,y < 1$) are of particular environmental importance because of the rapidly increasing use of these materials in micro- and nano-structured form as cathodes in lithium-ion batteries. Because the use of lithium ion batteries in consumer electronics is rapidly expanding and their recycling is limited,[11] understanding the chemical transformations of $LiCoO_2$ has significant potential for environmental risk assessment and provides fundamental insights of a broader class of high-valence transition metal nanoparticles. Released cobalt from $LiCoO_2$ is hazardous to cells in aqueous environments because it is carcinogenic, induces oxidative stress, competes with the intended ions (e.g., Fe^{2+}) for binding sites in metalloproteins, induces a hypoxia-like state, and has increased mobility once in the Co(II) form.[12, 13] Cobalt is released in a manner strongly dependent on the oxidation state. At pH = 6, the solubility of Co^{3+} is ~1×10^{-20} M compared with $>10^{-5}$ M for Co^{2+}, based on the experimental solubility products of $Co(OH)_3$ and $Co(OH)_2$.[14, 15] Among redox-active biomolecules that could impact $LiCoO_2$ dissolution, the $NADH/NAD^+$ and GSH/GSSG redox couples, depicted in Figure 3.1, are among the most important. NADH can be oxidized to

NAD^+, while GSH can be oxidized to glutathione disulfide (GSSG) by forming a disulfide dimer. Both NADH/NAD^+ and GSH/GSSG act as coenzymes and substrates for various metabolic processes and maintain an appropriate redox state within the cell (e.g., antioxidants).[16, 17]

Here we report an investigation of the interaction between $LiCoO_2$ nanoparticles with NADH and GSH. Between these molecules, we choose to primarily study NADH with some comparison to GSH. Prior studies have shown surface-mediated oxidation of GSH on nanocarbon surfaces.[18, 19] NADH or GSH may interact is such a way with $LiCoO_2$, which to our knowledge has not been reported. Additionally, the redox-dependent fluorescence of NADH/NAD^+ allows easy detection, making the molecule an appealing choice. Quantitative measurements of Co release using inductively coupled plasma-mass spectrometry (ICP-MS) show that exposure of $LiCoO_2$ nanoparticles to either NADH or GSH increases solubilization of cobalt, while corresponding spectroscopic measurements show that NADH is concurrently oxidized to NAD^+. To demonstrate that these effects are a consequence of the high valence of Co(III) in $LiCoO_2$, we performed control experiments using Co(II)-containing $Co(OH)_2$ and $LiCoPO_4$. Additionally, by testing interaction of $LiCoO_2$, etc. with molecules of similar structure to NADH and GSH, but that are not reducing agents, we find the NADH oxidation / Co reduction effect due to a redox reaction and not chelation of a specific functional group with Co or the dissolved ions. This coupled transformation of $LiCoO_2$ and redox-active biomolecules has implications in the biological impacts of high-valence metal oxide nanomaterials and the redox-driven weathering of metal oxides.

3.2 Experimental.

3.2.1 Nanoparticle synthesis and characterization.

We synthesized sheet-like nanoparticles of cobalt hydroxide, $Co(OH)_2$, and $LiCoO_2$ following procedures we described previously.[20, 21] $Co(OH)_2$ nanosheets were prepared via a precipitation method. The $Co(OH)_2$ precursor was converted to Li_xCoO_2 using a molten salt flux of 6:4 molar ratio of $LiNO_3$:LiOH at 200 °C. As a control sample, we synthesized rod-like Cmcm

$LiCoPO_4$ nanoparticles using a microwave-assisted solvothermal method adapted from a method published previously.[22] All solutions in this study were prepared from nanopure water (Barnstead Genpure System, $\rho \geq 18.2$ MΩ·cm). Detailed procedures for nanoparticle syntheses are found in section 3.5.2 and chemical information is found in Table 3.2.

Powder X-ray diffraction (XRD) patterns were obtained for each sample using a Bruker D8 Advance diffractometer equipped with a copper K_α source and 6 mm slit width. Samples for XRD analysis were prepared by affixing nanoparticle powder onto a B-doped silicon crystal zero-diffraction plate (MTI Corporation) with vacuum grease. Scanning electron microscope (SEM) images were collected using a LEO Supra55 VP field-emission scanning electron microscope. Samples for SEM were prepared by drop-casting a dilute solution of nanoparticles suspended in ethanol onto a conductive B-doped silicon wafer. Specific surface area measurements of ~0.1 g vacuum-dried samples were determined by nitrogen physisorption (Micromeritics Gemini VII 2390 surface area analyzer) and Brunauer-Emmett-Teller (BET) analysis.[23] Lastly, we used dynamic light scattering (DLS) and laser Doppler microelectrophoresis with a Malvern Zetasizer Nano ZS to measure particle aggregate size and surface charge (respectively) in the solution of interest. Each particle type was suspended in minimal medium with dextrose (see section 3.2.2) at 100 $mg \cdot mL^{-1}$ in approximately 10 mL. These stock solutions were then diluted to 5 $mg \cdot mL^{-1}$. Particle suspensions were sonicated for 1 h in a cup ultrasonicator with cooling water (10 s on, 10 s off for 30 min total sonication time) immediately before analysis. The results reported are averages and standard errors of the mean of at least three measurements of size (number mean) and zeta potential for each sample.

3.2.2 Dissolution studies with nanoparticles and biomolecules.

A model bacterial growth medium with minimal constituents ("minimal medium" with dextrose) was prepared in nanopure water with various salts, 4-(2-hydroxyethyl)-1-piperazineethanesulfonic acid (HEPES) buffer, and dextrose. See Table 3.2 for chemical information and Table 3.3 for the full composition of minimal medium with dextrose. We recognize that minimal medium used may not fully replicate the complex environment inside cells, perhaps warranting further investigations. However, this medium does provide a relatively simple matrix to investigate the specific interactions of NADH and other molecules with the nanomaterials of interest. Additionally, while NADH is typically unable to transverse membranes, there is evidence that lower concentrations of NADH (< 1 μM) can exist in extracellular matrices via transmembrane protein transport or other mechanisms.[24] It follows that our conclusions do not rely on nanomaterials entering cells.

NADH reduced disodium salt, NAD^+ free acid, L-glutathione reduced, and ophthalmic acid were obtained from Sigma Aldrich and used as received. Ophthalmic acid (OA) is nearly identical to glutathione in structure, except it lacks the redox-active thiol group (Figure 3.1C). Solutions were prepared for each molecule of interest by dissolving 0.5 mM in minimal medium. This concentration was chosen because it is relevant to concentrations of these molecules found in certain cells[25-27] and produces suitable fluorescence and absorbance signals for NADH/NAD^+ solutions. Nanoparticles were introduced to each solution at 1 $mg \cdot mL^{-1}$ nanoparticle concentration, using vials of approximately 3 mL. The sealed vials were covered from light and shaken for 24 h. The samples were then centrifuged at 13,100 × g for 20 min (Eppendorf MiniSpin plus). Finally, the supernatant was collected and filtered through 0.1 μm porosity syringe filter cartridges (Millex VV) to ensure nanoparticle removal. Preliminary experiments in which particles were isolated only by centrifugation showed light scattering in fluorescence measurements, particularly for $LiCoO_2$. Light scattering was eliminated with the introduction of the additional syringe filter isolation step to completely remove nanoparticles from the solutions. While the 0.1 μm porosity dimension is larger than certain particle dimensions, most particles are likely blocked as aggregates while navigating the filter. All experiments were performed in at least duplicate and error bars represent standard error of the mean.

We performed another form of dissolution experiment to study the kinetics of NADH and $LiCoO_2$ reacting in a single solution over time. $LiCoO_2$ was introduced at 1 $mg \cdot mL^{-1}$ to a single 30 mL solution of NADH in minimal medium in a larger reaction vessel. The reaction was stirred for

48 h total, and 1-mL aliquots were removed at 2 h, 6 h, 12 h, 24 h, and 48 h (five total). The 1 mg·mL^{-1} concentration for $LiCoO_2$ does not vary greatly from aliquot removal because the volume change (1 mL) is small relative to the total volume (30 mL) and the stirred solution is moderately homogeneous. The aliquots were centrifuged and filtered in the same way as the above samples.

3.2.3 Quantification of NADH concentrations.

The concentration of NADH in samples was determined using fluorescence measurements using an ISS K2 photon-counting spectrofluorimeter, using measurement conditions similar to those reported previously.[28, 29] Samples were placed in a fused silica cuvette at room temperature, excited at λ_{ex} = 338 nm, and the emission spectrum was measured between λ_{em} = 400 and λ_{em} =550 nm with a step size $\Delta\lambda$ = 1 nm and integration time of 1 s per step. NADH exhibits an emission peak at $\lambda_{ex} \approx$ 455 nm, whereas NAD^+ does not. The intensity was background-subtracted using a blank consisting of minimal medium with dextrose. Spectra were also normalized to the fluorescence of a solid tetraphenylbutadiene (TPB) standard to account for day-to-day variations in lamp intensity. NADH was quantified by converting the fluorescence intensity to concentration using a calibration curve (Figure 3.8). As a secondary method for detecting NADH and NAD^+, UV-visible absorbance spectra were obtained of selected NADH and NAD^+ solutions using a Shimadzu UV2401 dual-beam spectrophotometer.

3.2.4 Determination of dissolved ion concentrations.

We used inductively coupled plasma mass spectrometry (ICP-MS, Shimadzu 2030) to measure dissolved ion concentrations in samples after centrifugation/filtration. Samples were acidified in 2.5% HNO_3 before analysis. Additionally, a 500:1 dilution was required to reduce salt concentrations from the minimal medium. ^{7}Li and ^{59}Co intensities were measured and referenced to internal standards of ^{9}Be and ^{69}Ga, respectively. Each sample was measured in triplicate by ICP-MS and the average intensities were used for quantification. Concentrations of Li and Co were determined using calibration curves (Figure 3.9). Standard solutions of Li and Co (combined) were prepared by serial dilution from 1 g·L^{-1} certified reference materials. Standards were diluted and acidified in the same manner as the unknowns.

3.2.5 Nanoparticle-NADH binding experiments.

To examine if NADH/NAD$^+$ bind to nanoparticles surface, we used X-ray photoelectron spectroscopy to characterize the surface composition of nanoparticles that were exposed to NADH in nanopure water. Nanopure water was used instead of minimal medium to avoid the influence of dissolved salts on the XPS analysis. Nanoparticles at 1 mg·mL^{-1} concentration were exposed to NADH solutions for 24 h in ~3 mL vials; the samples were then centrifuged (same as above), the supernatant removed, and the remaining nanoparticles particles were rinsed and centrifuged 3× with nanopure water to remove any weakly adsorbed species. The particles were then dried overnight in a vacuum oven. To determine elemental composition on the nanoparticle surfaces, the dried samples were pressed into indium foil and analyzed using a Thermo X-ray photoelectron spectrometer with a monochromatized Al Kα X-ray source and hemispherical analyzer at an angle 45° relative to the surface normal. Survey spectra were obtained summing three scans with a binding energy step size of 1 eV and pass energy of 200 eV, and high-resolution spectra were obtained average 10 (Co(2p)), 20 (O(1s) and C(1s)), or 50 (N(1s) and P(2p)) scans with step size of 0.2 eV and pass energy of 50 eV. Casa XPS software was used for data analysis. For area quantification, peaks were fit to 70:30 Gaussian-Lorentzian functions with Shirley[30] background correction.

3.3 Results and discussion.

3.3.1 Nanoparticle characterization.

SEM images in Figure 3.2A-C show relatively monodisperse size and shape within each particle type, with the range in size from $LiCoPO_4$ > $Co(OH)_2$ > $LiCoO_2$. $LiCoO_2$ and $Co(OH)_2$ form hexagonal sheets and $LiCoPO_4$ forms cylindrical rods. Specific surface area measurements (S) were found as $S_{LiCoO2} = 126.5 \pm 0.4$ m^2·g^{-1}, $S_{Co(OH)2} = 33.29 \pm 0.05$ m^2·g^{-1}, and $S_{LiCoPO4} = 28.1 \pm 0.2$ m^2·g^{-1}. Differences in these specific surface areas are consistent with sizes observed in SEM.

Since most of the experiments reported herein are conducted according to particle mass concentration ($mg \cdot mL^{-1}$), this difference in surface area will be addressed in section 3.3.3.

Table 3.1 shows the results of characterizing particles in minimal medium via DLS size (mean diameter approximating as spherical) and zeta potential. DLS sizes for $LiCoPO_4$ and $Co(OH)_2$ are only slightly larger than compared to what is observed in SEM, indicating minor aggregation. On the other hand, the DLS size for $LiCoO_2$, is much larger than the primary particles observed in SEM, indicating significant aggregation. All three particle types possess a similarly negative zeta potential, which is consistent with all of them being partially deprotonated and/or delithiated in the salt/buffer solution at circumneutral pH.

XRD diffraction patterns of all three particle types are consistent with previously published reference patterns (Figure 3.2D-F),[31-33] indexed to the $R\bar{3}m$ ($LiCoO_2$), $P\bar{3}m1$ ($Co(OH)_2$) and Cmcm ($LiCoPO_4$) space groups. This agreement indicates that the particles are crystalline and have the correct structure. Slight broadening of XRD peaks is expected given their nanoscale size.[34] Transmission electron microscopy (TEM) images of $LiCoO_2$ nanosheets before and after exposure to minimal medium reveal a layered structure ~8 nm thick that does not change significantly with solution exposure (Figure 3.10).

3.3.2 Influence of NADH and GSH on Co release.

Figure 3.3 shows the concentrations of Co measured after $LiCoO_2$, $LiCoPO_4$, and $Co(OH)_2$ nanoparticles were introduced into minimal medium for 24 h. Similar data for Li are included in Figure 3.11. Figure 3.3 shows key differences across particles and across solutions tested. Figure 3.3A shows that exposing $LiCoO_2$ to NADH increases the release of Co approximately 3×, being statistically significant from the media alone at 95% confidence. Co release from $LiCoO_2$ with GSH exposure is higher than from media alone (nearly 2×), though not statistically significant at 95% confidence. Since NADH and GSH contain functional groups (phosphate and carboxylic acid groups, respectively) that could complex with Co ions, we conducted further studies using NAD^+

and ophthalmic acid (OA). These molecules are nearly identical in structure to NADH and GSA but lack the redox-active functional groups with the ability to reduce Co(III) in $LiCoO_2$. Furthermore, this experiment is necessary because in our experiments (see section 3.3.5) and in prior studies, phosphate is shown to have affinity for the $LiCoO_2$ surface. Figure 3.3A shows that NAD^+ and OA exposure yields Co concentrations not statistically different from the media alone, and much lower than Co concentrations from NADH or GSH exposure. Based on these results, we conclude that the enhancement produced by NADH arises from its oxidation-reduction properties and cannot be attributed to complexation of Co ions with the phosphate groups. Interestingly, NADH shows a greater effect on Co release compared to GSH. By comparing their reduction potentials at pH 7.0 vs. SHE (E^0_{NADH} = -0.320 V[35] and E^0_{GSH} = -0.252 V[36]), NADH is the stronger reducing agent. This is consistent with 1) redox reactivity being the involved in increased Co release and 2) enhancement in Co release from NADH exposure compared to GSH exposure.

To further verify that the enhancement in Co release from $LiCoO_2$ induced by NADH is due to the ability of these molecules to reduce Co(III) (in $LiCoO_2$) to the more highly soluble Co(II), we conducted control experiments using two nanoparticle compositions in which Co exists in a Co(II) state: $LiCoPO_4$ (Figure 3.3B) and $Co(OH)_2$ (Figure 3.3C). Figures 3.3B-C show that for these compositions, the redox-active molecules NADH and GSH as well as the non-redox-active counterparts (NAD^+ and OA) do not increase the amount of Co release compared with minimal medium. In the case of $LiCoPO_4$, no Co concentrations from molecule exposures are statistically distinct from Co concentration of media alone at 95% confidence. Exposure to certain molecules for $Co(OH)_2$ also shows slight decrease in Co concentration, with NAD^+ and GSH statistically different from media alone at 95% confidence. Based on these data, we conclude that the influence of NADH on $LiCoO_2$ to enhance Co release can be ascribed to their ability to reduce Co(III) to Co(II). The slightly decreased Co release from $Co(OH)_2$ and $LiCoPO_4$ exposed to each molecule compared to with minimal medium alone suggests that these molecules may adsorb to the nanoparticles surfaces and partially restrict ion release (discussed in section 3.3.5).

Since $LiCoO_2$ and $LiCoPO_4$ are Li intercalation compounds, we also quantified the Li release to examine if it is impacted by the presence of each molecule (Figure 3.11). Dissolved Li concentrations for a given particle in Figure 3.11 are largely unaffected by changing the composition of the dissolution media. Consistent with prior results, the amount of Li released from these nanoparticles exceed that of Co, since H^+ ions in the buffered solution can exchange with Li^+ ions in the solid without involving any redox processes.[37] The Li^+/H^+ exchange increases the pH of the solution, as shown by our pH measurements in Table 3.4. Increase in pH occurs despite the medium being buffered with HEPES due to the high particle concentration ($1\ mg \cdot mL^{-1}$) used in our experiments. Notably, the pH values measured after 24-h exposure of $LiCoO_2$ nanoparticles to minimal medium and minimal medium with NADH, NAD^+, GSH, and OA are identical within 0.2 pH units. Therefore, we conclude that while Li^+/H^+ exchange occurs and increases pH, this process is independent from the mechanism causing enhanced Co release in $LiCoO_2$ in the presence of NADH or GSH and not in the presence of NAD^+ or OA.

3.3.3 NADH oxidation during $LiCoO_2$ dissolution.

Our results indicate that the enhancement in Co release induced by the presence of NADH involves reduction of Co(III) to Co(II). In this case, the release of Co should be directly accompanied by an equivalent oxidation of NADH to NAD^+ or possibly to other oxidation products. Figure 3.4 shows the NADH concentration remaining in solution after nanoparticles of the indicated compositions were introduced into the NADH solution for 24 h. These data show that [NADH] greatly decreases with exposure to $LiCoO_2$, slightly decreases with exposure to $Co(OH)_2$ and is statistically unchanged at 95% confidence when exposed to $LiCoPO_4$. Also shown in Figure 3.4 are results from control samples prepared in an identical manner except lacking NADH; these samples show no significant fluorescence. We attribute the large decrease in [NADH] with $LiCoO_2$ to the oxidation of NADH coupled with Co release from $LiCoO_2$. The slight decrease in observed [NADH] with $Co(OH)_2$ exposure is consistent with our results in Figure 3.7B showing NADH adsorbing onto the surface of $Co(OH)_2$, as any adsorbed molecules would be removed from the solution with the particles before fluorescence analysis (see section 3.3.5).

Considering that the specific surface area of $LiCoO_2$ particles (126.5 ± 0.4 $m^2 \cdot g^{-1}$) is approximately 4 - 4.5 times the specific surface areas of $Co(OH)_2$ (33.29 ± 0.05 $m^2 \cdot g^{-1}$) and $LiCoPO_4$ (28.1 ± 0.2 $m^2 \cdot g^{-1}$), we performed $LiCoPO_4$ dissolution experiments normalized by surface area instead of mass (i.e., 4.5× $LiCoPO_4$ particle concentration) to ensure that selective loss of NADH is not simply a surface area effect. The resulting [NADH] measured by fluorescence is shown in Figure 3.4 as "*$LiCoPO_4$". The [NADH] for surface area normalized *$LiCoPO_4$ samples is nearly identical to the [NADH] for mass-normalized $LiCoPO_4$ and $Co(OH)_2$ samples and much higher than that for $LiCoO_2$ samples. This shows that the differences in dissolution behavior and biomolecule interactions between $LiCoO_2$ and $LiCoPO_4/Co(OH)_2$ are due to differences in their chemical properties, not differences in surface areas.

While we anticipate that loss of NADH fluorescence is caused by oxidation to NAD^+, we also considered whether loss of NADH might be cause by several other phenomena, including 1) a reaction of NADH with dissolved Co^{2+} or Li^+ ions, 2) adsorption of NADH onto the filter used to remove particles, and 3) interference in fluorescence spectra from residual particles scattering light. Details of these control experiments are presented in section 3.5.3 and Figure 3.12. Notably, exposing NADH solution to dissolved Co^{2+}/Li^+ ions similar in concentration to experimental solutions or passing NADH solution through the syringe filter show no appreciable decrease in their fluorescence intensities. These control experiments uniformly confirm that NADH is oxidized to NAD^+ by the nanoparticles.

As a complement to measuring the loss of NADH by fluorescence, we also used UV-visible absorption spectra of NADH solutions with/without exposure to $LiCoO_2$, $LiCoPO_4$ and $Co(OH)_2$ to assess the concentrations of NADH and NAD^+ before/after nanoparticle exposure. NADH and NAD^+ both exhibit peaks around 203 nm and 259 nm with similar molar absorptivities, whereas NADH alone exhibits a peak at 339 nm.[38] Section 3.5.4 contains a detailed analysis of NADH and

NAD^+ UV-visible absorbance spectra (Table 3.5 and Figure 3.13). Interestingly, we found concentration-dependent peak shifts at higher concentrations, perhaps due to molecule aggregation/stacking. Based on their spectral properties, we can identify the redox state of a NADH/NAD^+ solution using absorbances at 259 nm and 339 nm. For a NADH solution exposed to particles, the three possible cases are: 1) to retain absorbance at 339 nm, NADH has not been transformed to NAD^+, removed, or degraded, 2) to lose absorbance at 339 nm but retain absorbance at 259 nm, NADH has been oxidized to NAD^+, or 3) to lose absorbance at both 339 nm and 259 nm, NADH has been removed from the system or severely degraded. Figure 3.5 shows a clear difference in which case is followed between solutions exposed to $LiCoO_2$ compared to solutions exposed to $LiCoPO_4$ or $Co(OH)_2$. With exposure to $LiCoPO_4$ or $Co(OH)_2$, NADH solutions maintain absorbance at 339 nm and 259 nm, indicating that NADH is unchanged (case #1). With exposure to $LiCoO_2$, absorbance at 339 nm is almost entirely lost, while absorbance at 259 nm is constant (case #2). Therefore, our UV-visible absorption results support the conclusion that NADH is oxidized to NAD^+ with $LiCoO_2$ exposure, but not with $LiCoPO_4$ or $Co(OH)_2$ exposure. Since these data suggest NAD^+ was present in our prior fluorescence studies, we confirmed that solutions of NAD^+ with/without nanoparticle exposure yield negligible fluorescence compared to NADH solutions (Figure 3.14).

Since NADH/NAD^+ absorbance properties change with concentration, particularly at the 500 μM used for most dissolution experiments, additional dissolution experiments identical to those described in the experimental were performed exposing $LiCoO_2$ to 100 μM NADH in minimal medium. The results combining $LiCoO_2$ and 100 μM NADH show a decrease in [NADH] measured by fluorescence from 91.6 ± 6.6 μM to 2.21 ± 0.19 μM, and an increase in released Co measured by ICP-MS from 0.120 ± 0.002 mM to 0.139 ± 0.006 mM. These changes reaffirm that NADH enhances Co release and $LiCoO_2$ oxidizes NADH. Since results are consistent across the NADH concentrations tested, we conclude that the increase in released Co and oxidation of NADH at higher concentrations is not due to some specific spectral or aggregation effect of NADH, but through interaction with $LiCoO_2$.

The relative magnitudes of NADH removal and Co release for 100 μM NADH exposure are different compared to those of the 500 μM NADH experiments (i.e., Figures 3.3 and 3.4) because in the case of 100 μM, $[LiCoO_2] \approx 100\times[NADH]$, whereas in the case of 500 μM, $[LiCoO_2] \approx 20\times[NADH]$ (1 $mg\cdot mL^{-1}$ $LiCoO_2$ for both). That is, in the extreme where $[LiCoO_2] >> [NADH]$, a given amount of reaction yields a relatively large change in [NADH] and a relatively small change in released Co concentration.

3.3.4 Reaction kinetics of NADH and $LiCoO_2$.

To characterize the kinetics of the interaction between NADH and $LiCoO_2$, we measured the concentrations of NADH (reactant) and released Co (product) over time for a single reaction solution. Time-points were taken from 2-hr to 48-hr, spanning the 24-hr time point used in other experiments. The data in Figure 3.6A reveal an exponential decrease in [NADH] over the course of reaction. The general rate equation for this reaction is described by Eq. 3.1:

$$\boldsymbol{\frac{d[NADH]}{dt} = k[NADH]^{n}[LiCoO_{2}]^{m}} \tag{3.1}$$

where k is the rate constant and n and m are reaction orders for NADH and $LiCoO_2$, respectively. As noted above, under the conditions of our experiments we assume $[LiCoO_2] >> [NADH]$ and $\Delta[LiCoO_2] \approx 0$. Because of this, even if $m \neq 0$ the rate expression in Eq. 3.1 can be simplified by combining $[LiCoO_2]^m$ within the rate constant, k:

$$\boldsymbol{\frac{d[NADH]}{dt} \approx k'[NADH]^{n}} \tag{3.2}$$

From curve fitting of [NADH], ln[NADH], and $[NADH]^{-1}$ vs. time, it is clear that the reaction is first order with respect to NADH (i.e., $n = 1$). For example, in the case of ln[NADH] vs. time a linear regression yields $R^2 = 0.972$, whereas for [NADH] vs. time linear $R^2 = 0.581$. We determined the pseudo-first-order rate constant of $k' = 0.084 \pm 0.007$ hr^{-1}. Interestingly, the $t = 0$ point in Figure 3.6A deviates more significantly from the fit than most points. This suggests that a separate process, possibly adsorption of NADH onto the particles (see section 3.3.5) occurs in the initial stages of dissolution to remove more NADH than expected over the longer-term reaction.

Concentrations of dissolved Co and Li for the same dissolution experiment are shown in Figure 3.6B. As with single time point experiments, [Li] >> [Co] due to Li^+-proton exchange. Both species are released at a greater rate in the initial stages of reaction, and plateau in concentration over time. The plot of Co concentration with time mirrors that of NADH with time, which we ascribe to solubilized Co being a product of the reaction of NADH with $LiCoO_2$. The decrease in the rate of Co-production with time is consistent with our conclusion that the NADH-$LiCoO_2$ reaction depends directly on [NADH].

3.3.5 Binding of NADH to nanoparticles.

The data in Figures 3.3 and 3.4 suggest that some of the apparent loss of NADH is due to adsorption onto the nanoparticle surfaces. Additionally, the sharp decrease in [NADH] at the first time point of our kinetics study suggests NADH adsorbs relatively quickly compared to the longer-term redox reaction. To determine the extent of NADH interaction with nanoparticle surfaces, we obtained XPS spectra of nanoparticles before and after exposure to NADH, using N(1s) emission to quantify the presence of NADH and using Co(2p) as an internal standard. Figure 3.7A shows representative N(1s) spectra from $LiCoO_2$ before and after exposure to NADH (0.5 mM, 24 h). Additional spectra are shown in Figure 3.15. Figure 3.7A clearly shows a pronounced increase in N(1s) emission intensity for the NADH-exposed sample compared to the unexposed sample. Figure 3.7B summarizes similar data for $LiCoO_2$, $LiCoPO_4$, and $Co(OH)_2$. We note that while NADH is the species introduced to the nanoparticles, the XPS spectra cannot distinguish between adsorbed NADH or NAD^+. We determined the surface coverage of N atoms bound to each surface ($LiCoO_2$, $LiCoPO_4$, and $Co(OH)_2$) from the N(1s) and Co(2p) photoelectron emission (Figure 3.7B), as described in section 3.5.5. Figure 3.7B shows the resulting surface coverages. The data show a statistically significant increase in N surface coverage with NADH exposure for $Co(OH)_2$ at 95% confidence, a moderate increase for $LiCoO_2$, and no change for $LiCoPO_4$. Using the known stoichiometry of 7 N atom per NADH/NAD$^+$ molecule, the N coverages correspond to 0.37 ± 0.07 NADH/NAD$^+$ molecule·nm^{-2} for $LiCoO_2$, 0.036 ± 0.007 molecule·nm^{-2} for $LiCoPO_4$, and 0.62 ± 0.05 molecule·nm^{-2} for $Co(OH)_2$. For comparison, assuming a density of closely packed NADH of ~1.7 g·cm^{-3} (from solid NADH) and monolayer thickness of ~0.5 nm yields a maximum coverage of ~0.8 molecule·nm^{-2}. A 0.5 nm monolayer thickness is estimated using literature[39] bond lengths and assuming a monolayer of NADH/NAD$^+$ molecules bind via a phosphate moiety (see below) in a planar conformation roughly perpendicular to the surface. Thus, on $LiCoO_2$ and $Co(OH)_2$ the molecular coverages estimated from XPS are comparable to that expected from a monolayer of NADH/NAD$^+$.

The presence of significant N coverage after three cycles of rinsing, mixing, and centrifuging indicates that NADH/NAD$^+$ has a high affinity with $LiCoO_2$ and $Co(OH)_2$ surfaces. The strong binding we observe for NADH/NAD$^+$ with $LiCoO_2$ and $Co(OH)_2$ suggests that the phosphate moieties in NADH/NAD$^+$ bind to surface oxygen atoms on each particle surface, and that the phosphate-containing molecules do not bind to phosphate terminated particles (i.e. $LiCoPO_4$). This result is an agreement with prior work showing that phosphate binds strongly to $LiCoO_2$[21] and to Fe(III) oxides[40] via an inner-sphere configuration on an oxygen-terminated surface. Notably, prior work reported that despite its attachment to the $LiCoO_2$ surface, phosphate does not increase $LiCoO_2$ dissolution.[21] In contrast, we find that NADH significantly increases $LiCoO_2$ dissolution. Using our measured $LiCoO_2$ specific surface area, XPS surface density, and known solution volumes, we determined that adsorption onto the $LiCoO_2$ nanoparticle surfaces accounts for decrease in total NADH concentration of (0.077 ± 0.014 mM). This value is much smaller than the actual decrease in [NADH] after 24-h $LiCoO_2$ exposure (0.539 ± 0.012 mM) that we observed and allows us to conclude that while NADH binds to $LiCoO_2$ nanoparticle surfaces, surface adsorption is not the primary origin of the decrease in [NADH] observed in Figures 3.4 and 3.5. On the other hand, the fact that NADH binds even more strongly with $Co(OH)_2$ can explain the much smaller decrease in [NADH] seen in Figure 3.4. Any NADH molecules adhering to the

$Co(OH)_2$ particles are removed from the solution and would not contribute to the measured fluorescence.

3.3.6 Coupled transformation of NADH and $LiCoO_2$.

The data in Figure 3.3 show that in minimal medium alone (i.e., in the absence of NADH or other intentionally added reducing agents), the amount of Co released from $LiCoO_2$ is much less than the amount released from $LiCoPO_4$. This observation is consistent with the hypothesis that while $LiCoPO_4$ can directly release cobalt in the highly soluble Co(II) form, release of cobalt from $LiCoO_2$ is less favorable due to the highly insoluble nature of Co(III). The lower rate of release from $LiCoO_2$ in the absence of added reducing agents is further supported by density functional theory (DFT) and thermodynamics calculations of the initial steps (loss of first partial-monolayer) in release of Co from the lowest-energy surface faces of $LiCoO_2$ and $LiCoPO_4$ in water. These calculations (see section 3.5.7) indicate that the initial release of Co from the $LiCoO_2(001)$ surfaces in pure water at pH = 7 (with other water-soluble species set at 10^{-6} M) is endergonic with an energy change of $\Delta G = +1.15$ eV/Co while initial release from the $LiCoPO_4(010)$ surface is exergonic, $\Delta G = -0.87$ eV/Co, in qualitative agreement the experimental results.

Our experiments demonstrate that NADH greatly increased the rate of Co release from $LiCoO_2$, while no corresponding increase release from $LiCoPO_4$. This observation strongly points to an electrochemically driven interaction between NADH and $LiCoO_2$. The electrochemical reduction of $LiCoO_2$ with release of Co^{2+} can be described via the half-cell reaction:

$$LiCoO_{2(s)} + 4H^+_{(aq)} + e^- \rightleftharpoons Li^+_{(aq)} + Co^{2+}_{(aq)} + 2H_2O_{(l)} \qquad E^0_{(SHE)} = 2.14\ V \qquad (3.3)$$

Here, the standard electrochemical reduction potential of $E^0 = +2.14$ V at 25°C can be readily determined using the Gibbs free energy of formation of $LiCoO_2$ from the pure elements at standard state ($-615\ kJ\cdot mol^{-1}$)[41, 42] and standard electrochemical potentials. The $NADH/NAD^+$ couple is described by the electrochemical reduction:[35]

$$NAD^+_{(aq)} + H^+_{(aq)} + 2e^- \rightleftharpoons NADH_{(aq)} \qquad E^0_{(SHE)} = -0.315\ V \qquad (3.4)$$

Coupling these two together to form the electrochemically mediated reaction (Eq. 3.5) yields a net $\Delta G = -4.9$ eV (-474 kJ·mol^{-1}) as written, or -2.45 eV per Co^{2+} ion released.

$$2LiCoO_{2(s)} + 7H^{+}_{(aq)} + NADH_{(aq)} \rightleftharpoons 2Li^{+}_{(aq)} + 2Co^{2+}_{(aq)} + 4H_2O_{(l)} + NAD^{+}_{(aq)} \qquad (3.5)$$

Additionally, our measurements of [NADH] vs. time and [Co] vs. time demonstrate the reaction is first order with respect to NADH and that the reaction rate is greatest when nanoparticles and NADH solution are first exposed to one another. While the stoichiometry of Eq. 3.5 suggests there should be two Co ions released for each molecule of NADH that is reduced, experimentally we observe that the Co release (0.32 ± 0.13 mM) is smaller than the loss of NADH (loss of 0.539 ± 0.012 mM). This greater than anticipated loss of NADH suggests that NADH may be simultaneously involved in other reduction reactions, such as:

$$NADH + H^{+} \rightleftharpoons NAD^{+} + H_{2(g)} \qquad (3.6)$$

with $\Delta G^0 = +0.037$ eV. A prior study reported evidence for direct surface oxidation of NADH at Co_3O_4 surfaces,[43] while other studies have shown that oxides made from metal oxides exhibit enhanced electrochemical reduction of NADH and have attributed this enhancement to the ability of metal oxide surfaces to adsorb protons.[43] As a result, we conclude that while release of Co(II) is directly attributed to NADH, the transformation of NADH and NAD^+ may be further increased by additional surface-catalyzed reactions.

3.4 Conclusions.

Our results show that biological molecules that are important in cellular respiration and electron transport can play an active role in the transformation of high-valence transition metal oxides through redox chemistry at nanoparticle surfaces. NADH interacts with $LiCoO_2$ nanoparticles by redox chemistry at the solid-liquid interface: electrochemical reduction of Co(III) to Co(II) allows Co to be easily solubilized and released into solution while also oxidizing NADH to NAD^+. We attribute this coupled redox transformation to redox reaction between Co(III) within $LiCoO_2$ and NADH reducing agents, and not a complexation/chelation/pH effect, based on five pieces of evidence. First, NADH and GSH produce similar effects when exposed to $LiCoO_2$ despite differences in their structures. Second, non-reducing analogues of NADH and GSH do not reproduce the same effects. Third, NADH is oxidized when exposed to $LiCoO_2$ but not when exposed to $LiCoPO_4$ or $Co(OH)_2$ (whether samples are normalized by mass or surface area) and is not oxidized when exposed to Co^{2+}/Li^{+} ions. Fourth, Li release is relatively unaffected by the presence of the molecules, as this occurs primarily by H^{+} exchange, and pH change is found to not be the driver of changes in dissolution in our experiments. Lastly, measuring concentrations of NADH (reactant) and released Co (product) over time reveal a direct relationship between reaction rate and [NADH].

Redox transformations of nanoparticles and biological electron transport molecules pose two important mechanisms for toxicity in the environment. First, the reduction of Co(III) and other high valence metals to lower-valence states increases their solubility and leads to faster release into the aqueous phase. High concentrations of metals such as Co and Ni released from metal oxides have been shown to induce toxicity towards various aquatic organisms.[44, 45] Select microorganisms (e.g., *Shewanella oneidensis* MR-1) are known to reduce high valent metals (Fe, Co, Mn) in minerals extracellularly,[46] increasing metal ion release.[47-49] We find similar behavior from introduction of reducing biomolecules, suggesting that this metal-reduction phenomenon could occur to a lesser extent from non-metal-reducing organisms interacting with high surface area nano-scale metal oxides. Secondly, the corresponding oxidation of NADH, GSH, and other molecules relevant to electron transport and cellular homeostasis can serve as an additional pathway to biological impact. When redox-active molecules facilitate metal oxide nanoparticle dissolution, they can be transformed or degraded. In the case of NADH and GSH, severe unnatural oxidation surrounding a non-metal-reducing organism from interaction with a nanoparticle will alter the $NADH:NAD^{+}$ and GSH:GSSG ratios in/around cells, entirely disrupting cellular redox homeostasis. Imbalances in GSH or NADH concentrations can have many toxic effects,[50] but in particular, removal of the reduced forms of these well-known antioxidants may lower cellular defenses against ROS. Several studies have observed ROS in the presence of nanomaterials,[51, 52] including LiCoO$_2$.[53] In such cases, whether nanoparticle transformation or cellular machinery generates ROS, the ROS will more negatively impact cells with reduced anti-oxidant capability.

3.5 Figures and supporting information.

3.5.1 Primary figures.

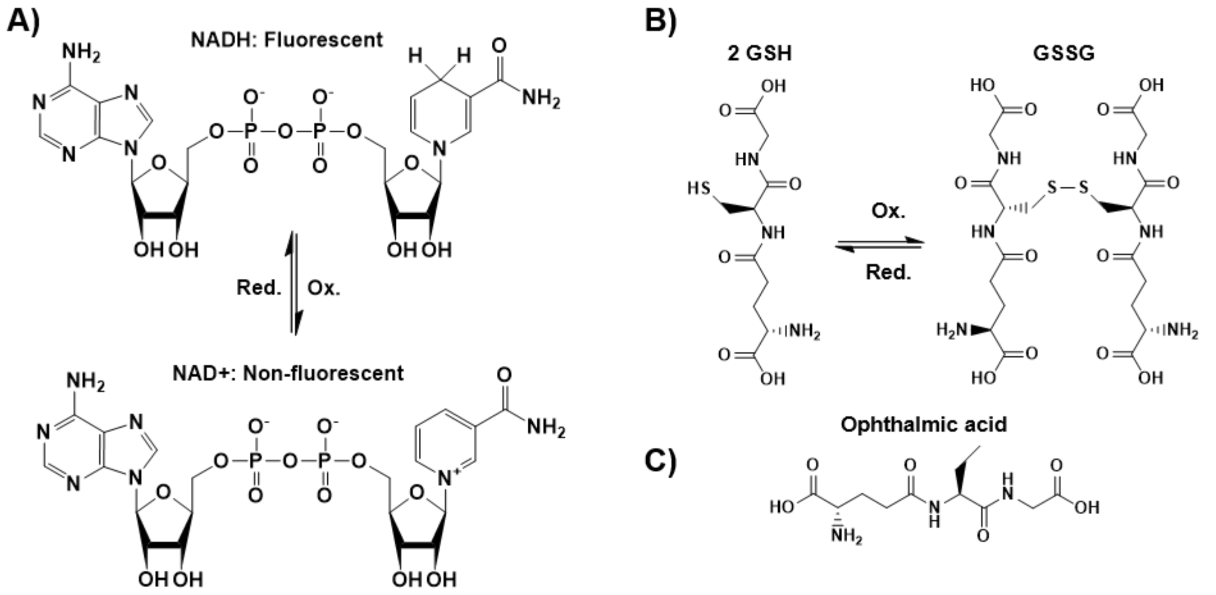

Figure 3.1. Oxidation-reduction equilibria (H$^+$ not shown) of the biomolecules A) NADH and NAD$^+$, B) glutathione (GSG) and glutathione disulfide (GSSG), and C) structure of ophthalmic acid (OA), a molecule similar to glutathione except lacking the redox-active thiol moiety.

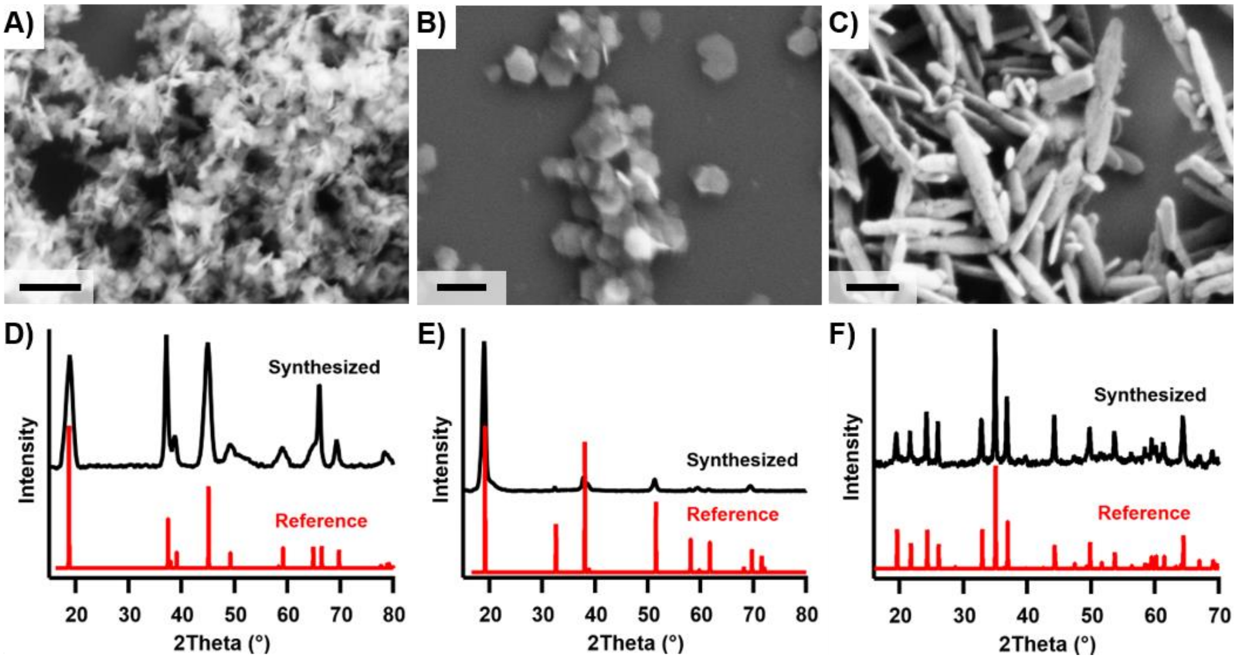

Figure 3.2. Scanning electron microscopy images and x-ray diffraction patterns for A/D) $LiCoO_2$, B/E) $Co(OH)_2$, and C/F) $LiCoPO_4$ nanoparticles, respectively. Scale Bars = 200 nm. Experimental XRD patterns (black) are compared to reference patterns (red). See text for references.

Table 3.1. Size and zeta potential of particles in minimal medium determined from DLS and laser Doppler microelectrophoresis.

Particle	Mean d (nm)	Zeta potential (mV)
$LiCoO_2$	364 ± 57	-18.4 ± 0.7
$LiCoPO_4$	118 ± 13	-16.5 ± 3.8
$Co(OH)_2$	130 ± 5	-16.0 ± 2.0

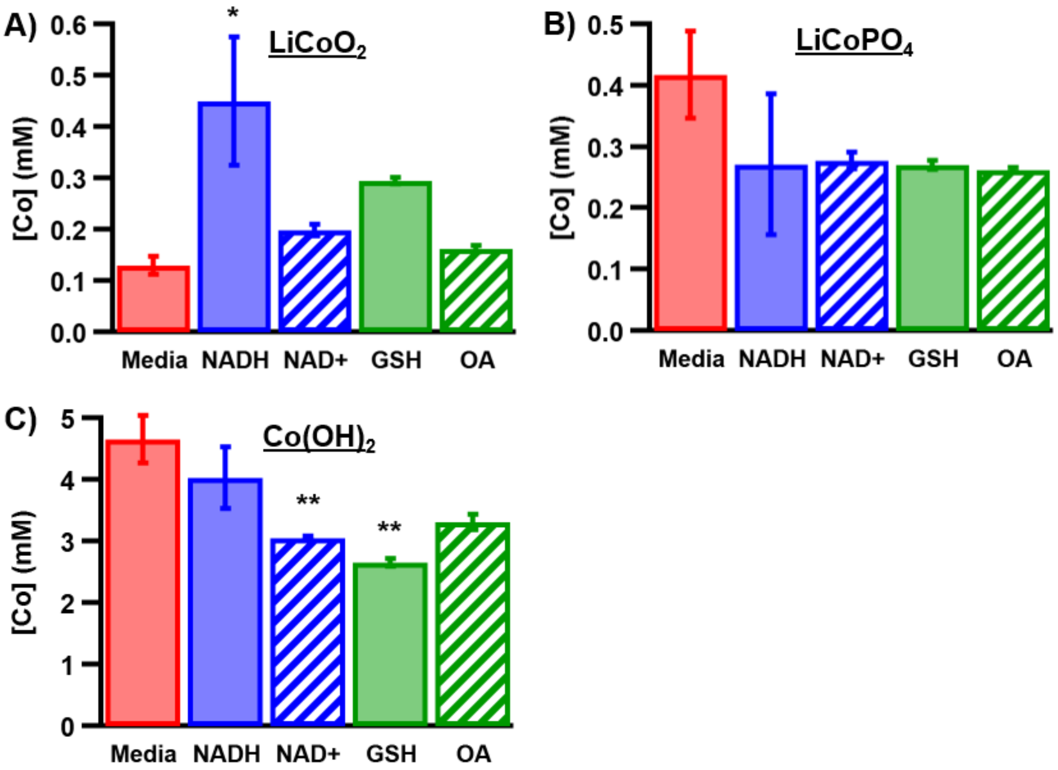

Figure 3.3. Dissolved Co concentrations in minimal medium solutions for A) $LiCoO_2$, B) $LiCoPO_4$, and C) $Co(OH)_2$ after 24-h exposure to each molecule under study. Molecule exposures are compared to media exposure with one-way ANOVA with Dunnett's multiple comparisons test: $n = 3$ or $n = 4$, * for $p < 0.05$ and ** for $p < 0.01$.

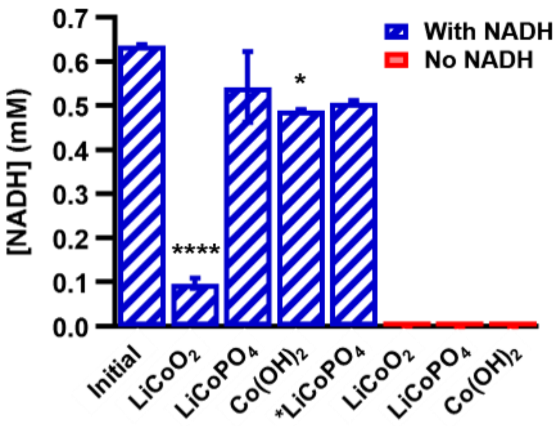

Figure 3.4. Concentration of NADH before (“initial”) and after exposure to the indicated nanoparticles for 24 h. “*$LiCoPO_4$” refers to NADH solutions after 24-h exposure to 4.5 × [LiCoPO4], a matching specific surface area exposure to $LiCoO_2$ samples. Particle solutions are compared to initial with one-way ANOVA with Dunnett’s multiple comparisons test: n = 2 or n = 3, * for $p < 0.05$ and *** for $p < 0.0001$. Also shown are fluorescence intensities of control samples prepared in an identical manner but without NADH (“No NADH”).

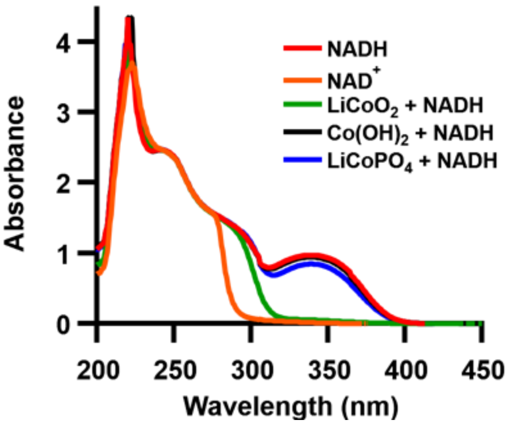

Figure 3.5. UV-visible absorption spectra of 0.5 mM solutions of NADH and NAD^+, and 0.5 mM NADH solutions after 24-h exposure to $LiCoO_2$, $LiCoPO_4$, and $Co(OH)_2$. All solutions were prepared in minimal medium, which also served as the background. All 0.5 mM NAD^+ samples exposed to nanoparticles yielded spectra nearly identical to the orange “NAD^+” trace without nanoparticle exposure and are omitted for clarity.

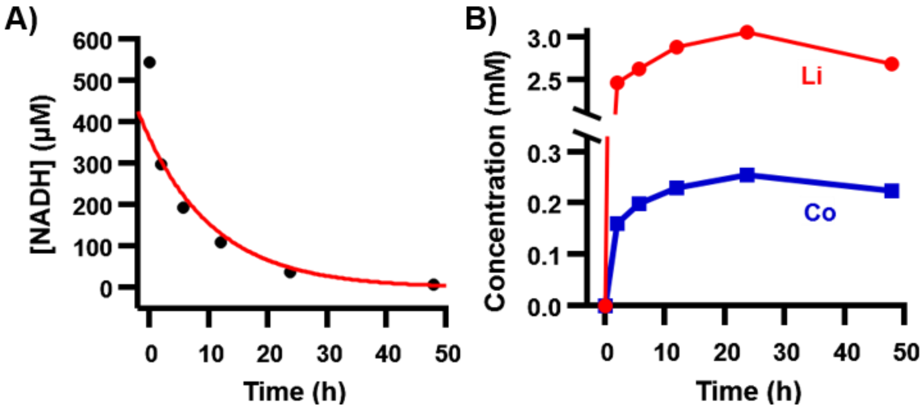

Figure 3.6. Concentrations measured over time for species in dissolution of 1 mg·mL^{-1} $LiCoO_2$ with 0.5 mM NADH A) NADH measured by fluorescence with exponential decay fit of $Y = 360 \cdot e^{-0.084 \cdot X}$, $R^2 = 0.972$, and B) concentrations of Li (red circles) and Co (blue squares) measured by ICP-MS.

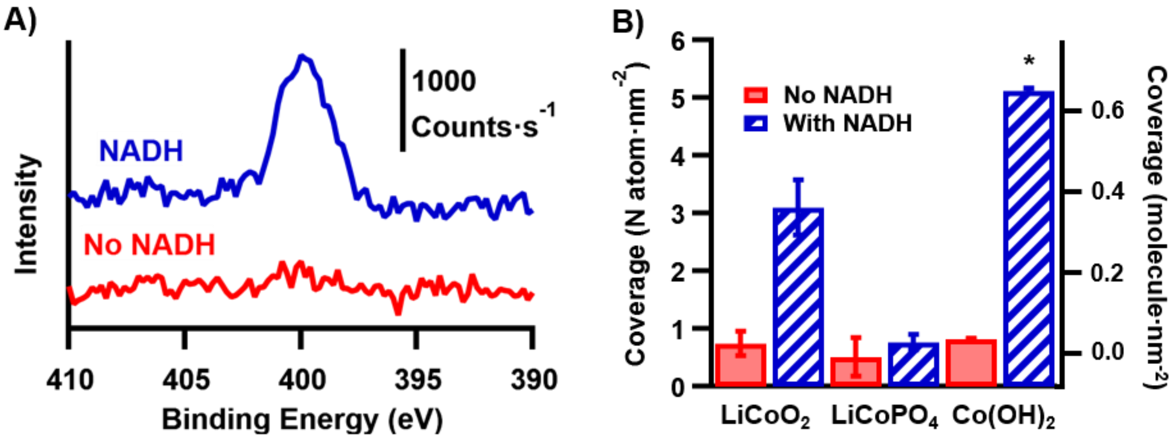

Figure 3.7. A) N(1s) XPS spectra of $LiCoO_2$ particles after 24-h soak in solutions with or without 0.5 mM NADH, and B) N atom surface coverages on nanoparticles after 24-h soak with or without 0.5 mM NADH, determined from N(1s) and Co(2p) peak areas. With/without NADH samples are compared for a given particle type with unpaired t-test with Welch's correction: n = 2 or n = 3, * for $p < 0.05$.

3.5.2 Nanoparticle synthesis procedures.

We synthesized sheet-like nanoparticles of cobalt hydroxide, $Co(OH)_2$, and $LiCoO_2$ following procedures we described previously.[20, 21] $Co(OH)_2$ nanosheets were prepared via a precipitation method. First, 20 mL of 1 M $Co(NO_3)_2$ was added dropwise to a 0.1 M solution of LiOH and the precipitate was collected immediately after addition. The precipitate was isolated and washed by 3 repeated cycles of centrifugation for 5 min at 4696 × g (Thermo Scientific, Sorvall Legend X1) and resuspension in water. After washing, the supernatant was decanted, and the solid product was dried in a vacuum oven at 30 °C overnight. The $Co(OH)_2$ precursor was lithiated to form Li_xCoO_2 by to a molten salt flux of 6:4 molar ratio of $LiNO_3$:LiOH at 200 °C in a poly(tetrafluoroethylene) container with magnetic stirring in a silicone oil bath. After 30 min the reaction was quenched with water. The precipitate was isolated by decanting the supernatant, washed by 3 repeated cycles of centrifugation, and dried in a vacuum oven at 30 °C overnight.

As a control sample, we synthesized rod-like Cmcm $LiCoPO_4$ nanoparticles using a microwave-assisted solvothermal method adapted from a method published previously.[22] Successful synthesis of the Cmcm $LiCoPO_4$ polymorph is extremely sensitive to any contributions of moisture, and therefore all reagents were stored and handled in an argon-atmosphere glovebox. First, ~15 mL of tetraethylene glycol (TEG) was dried with anhydrous magnesium sulfate in an approximate 1:3 volume ratio. This solution was stirred for approximately 2.5 hr, allowed to settle overnight, and then decanted and centrifuged at 4696 × g for 10 min to fully separate out any remaining magnesium sulfate. Lithium hydroxide monohydrate, cobalt (II) acetate tetrahydrate, and anhydrous (solid) phosphoric acid were mixed in 1:1:1 stoichiometric ratio (2.38 mmol) in 12 mL of dried TEG in a 35 mL borosilicate microwave vessel and stirred overnight. Next, the mixture was removed from the glovebox and quickly loaded into a CEM Discover® SP microwave synthesizer equipped with Activent® capabilities to avoid over-pressurization. The microwave settings were set to 300 W, ~50 psi, and 260°C for 30 minutes with continuous high-speed stirring. The resulting pink/purple product was transferred from the microwave vessel to a 50 mL centrifuge tube and separated from the TEG solvent by centrifugation. After decanting, the product was washed in 3 cycles by suspending in ~20 mL acetone through mixing and ultra-sonication, and then centrifugation at 4696 × g for 10 min. Finally, the wash solution was decanted, and the particles dried in a vacuum oven at 30 °C overnight.

3.5.3 Additional control experiments regarding NADH fluorescence.

First, we tested if dissolved Co^{2+} and Li^{+} ions alone (no particles) reproduced the decrease in [NADH] observed during $LiCoO_2$ dissolution, as this would suggest an aqueous phase reaction between the ions and NADH after nanoparticle dissolution. A 0.5 mM NADH solution was prepared with [Co] and [Li] typical after 24-h dissolution experiments (0.45 mM and 9.6 mM, respectively) from chloride salts. The fluorescence spectrum of this ion control solution after 24 h is nearly identical to that of the initial NADH solution (Figure 3.12A). Additionally, $Co(OH)_2$ releases similar amounts of Co to $LiCoO_2$ yet does not show the same dramatic decrease in [NADH] as with $LiCoO_2$. These data show that Li^{+} and Co^{2+} ions themselves have no effect on NADH concentration in our experiments.

Next, we were concerned that NADH might be lost during centrifugation steps or by molecules adsorbing onto the filter used during nanoparticle removal. To rule out this experimental error, a standard NADH solution (no particles) was treated in the same manner as unknown samples, including passing through the finely porous filter. The fluorescence spectra before/after passing through the filter are nearly identical (Figure 3.12B), showing that loss of NADH during the nanoparticle removal steps is minimal.

Removal of nanoparticles at the experiment stop time is necessary not only to halt dissolution, but also because nanoparticles would interfere with fluorescence analysis by absorbing and scattering light. To check that residual nanoparticles did not influence the experiment, nanoparticle dissolution samples without 0.5 mM NADH were analyzed by fluorescence. Samples without NADH yielded negligible fluorescence (Figure 3.4), as expected due to the lack of the fluorescent NADH. This eliminates the possibility of nanoparticles remaining in solution and interfering with NADH fluorescence spectra. NAD^{+} also contributes negligible fluorescence, as shown in Figure 3.14.

3.5.4 Additional control experiments regarding NADH and NAD$^+$ UV-visible absorbance.

Standard solutions of NADH and NAD+ in minimal medium and pure water were analyzed by UV-visible spectroscopy. Using minimal medium vs. pure water as the solvent yields no difference in results if the same solvent is used as the blank. Serial dilutions were performed to prepare 9 samples ranging logarithmically in concentration from 1 – 500 μM (Figure 3.13A-B). Peaks are present at 203 nm, 259 nm, and 339 nm (NADH only). Absorbance values and linear least squares analysis were used to calculate molar absorptivities for both species at each wavelength (Table 3.5). Figure 3.14C illustrates each peak and compares absorbance for solutions of NADH and NAD$^+$ at nominally the same concentrations. When the concentration of either species increases beyond ~200 μM, The 203 nm peak shifts to slightly higher wavelengths and the 259 nm peak splits in two (Figure 3.13D-E). In either concentration range, NADH and NAD$^+$ both absorb similarly below 280 nm and NADH absorbs much more strongly above 300 nm.

3.5.5 Description of XPS calculations.

To quantify bound NADH on each type of nanoparticle, we first determine the N atom surface coverage using the following equation:

$$N\ coverage = \frac{A_{N(1s)}}{A_{Co(2p)}} \times \frac{SF_{Co(2p)}}{SF_{N(1s)}} \times \frac{scans_{Co(2p)}}{scans_{N(1s)}}\ \rho_{Co}\lambda_{Co(2p)} \cos\theta \qquad (3.7)$$

Where $A_{N(1s)}$ and $A_{Co(2p)}$ are the areas for the respective peaks, $SF_{Co(2p)}$ and $SF_{N(1s)}$ are the sensitivity factors for the respective peaks ($SF_{Co(2p)} = 4.429$ and $SF_{N(1s)} = 0.407$), “scans” represents the number of scans summed for each peak, ρ_{Co} is the density of Co in the bulk, $\lambda_{Co(2p)}$ is the inelastic mean free path (IMFP) of Co(2p) electrons at the surface (estimated at 1.92 nm),[21] and θ is the angle of the analyzer relative to the surface normal (45°). This equation assumes the layer of NADH is thin relative to the electron IMFP and treats the bulk (Co) as an internal standard. The *molecular* coverage of NADH is obtained by subtracting the N coverage of samples not exposed to NADH and using the stoichiometry of 7:1, N atom to NADH molecule.

3.5.6 Determination of electrochemical potential for $LiCoO_2$ half reaction.

The electrochemical potential for the reaction $LiCoO_2 + 4H^+ + e^- \rightarrow Li^+ + Co^{2+} + 2H_2O$ was determined using the free energy of formation of $LiCoO_2$, combined with known electrochemical reactions, as outlined below:[41]

$Li_{(s)} + Co_{(s)} + O_{2(g)} \rightarrow LiCoO_2$ $\Delta G^0 = -615\ kJ \cdot mol^{-1}$

$Co^{2+}_{(aq)} + 2e^- \rightarrow Co_{(s)}$ $E^0 = -0.28\ V$

$Li^+_{(aq)} + e^-_{(SHE)} \rightarrow Li_{(s)}$ $E^0 = -3.04\ V$

$O_{2(g)} + 4H^+_{(aq)} + 4e^- \rightarrow 2H_2O$ $E^0 = +1.229\ V$

Using $\Delta G = -nFE$, the electrochemical potentials are converted to free energies, with electrochemical potentials of electrons referenced to the standard hydrogen electrode, $\Delta G^0_{(SHE)}$

$Li_{(s)} + Co_{(s)} + O_{2(g)} \rightarrow LiCoO_2$ $\Delta G^0 = -615\ kJ \cdot mol^{-1} = -6.37\ eV$

$Co^{2+}_{(aq)} + 2e^- \rightarrow Co_{(s)}$ $\Delta G^0_{(SHE)} = +0.56\ eV$ as written

$Li^+_{(aq)} + e^- \rightarrow Li_{(s)}$ $\Delta G^0_{(SHE)} = +3.04\ eV$ as written

$O_{2(g)} + 4H^+_{(aq)} + 4e^- \rightarrow 2H_2O$ $\Delta G^0_{(SHE)} = -4.916\ eV$ as written

The overall reaction: $LiCoO_2 + 4H^+_{(aq)} + e^- \rightarrow Li^+_{(aq)} + Co^{2+}_{(aq)} + 2H_2O$ can then be written as

$LiCoO_2 \rightarrow Li_{(s)} + Co_{(s)} + O_{2(g)}$ $\Delta G^0 = +6.37\ eV$

$Co_{(s)} \rightarrow Co^{2+}_{(aq)} + 2e^-$ $\Delta G^0_{(SHE)} = -0.56\ eV$ as written

$Li_{(s)} \rightarrow Li^+_{(aq)} + e^-$ $\Delta G^0_{(SHE)} = -3.04\ eV$ as written

$O_{2(g)} + 4H^+_{(aq)} + 4e^- \rightarrow 2H_2O$ $\Delta G^0_{(SHE)} = -4.916\ eV$ as written

The sum of these reactions, and their corresponding energies, then leads to

$LiCoO_2 + 4H^+_{(aq)} + e^- \rightarrow Li^+_{(aq)} + Co^{2+}_{(aq)} + 2H_2O$

$$\Delta G^0_{(SHE)} = +6.37 + (-0.56) +(-3.04) +(-4.916) = -2.14 \text{ eV}$$

Finally, the standard electrochemical potential is determined as $E^0=\Delta G^0_{(SHE)}/nF$ (here, n = 1)

$LiCoO_2 + 4H^+_{(aq)} + e^- \rightarrow Li^+_{(aq)} + Co^{2+}_{(aq)} + 2H_2O$ $E^0_{(SHE)} = +2.14$ V

3.5.7 Density functional theory (DFT) computations.

The free energy associated with the initial release of Co from $LiCoO_2$(001) surfaces was described previously.[54] Here we applied the identical methods and level of theory to determine the free energy associated with the initial release of Co from $LiCoPO_4$(010) surfaces. This approach couples first-principles calculations with thermodynamic experimental data. The overall dissolution process is following a two-step transformation. The starting surface is a $LiCoPO_4$(010) that has ½ monolayer of Li ions terminating the exposed surface. The half-monolayer Li termination corresponds to the surface that would be exposed by cleaving $LiCoPO_4$ along with (010) plane through a layer of Li atoms, with half the lithium atoms going to each of the two separating surfaces; this distribution of Li leads to free surfaces with zero net charge. In the first step, a Li/H ligand exchange occurs:

a. ½ Li-terminated $LiCoPO_4$ + 2H → ½ H-terminated $LiCoPO_4$ + 2Li (3.8)

In the next step, a Co atom is removed from the ½ H-terminated surface, yielding a $LiCoPO_4$ with a surface Co vacancy, denoted as $LiCoPO_4$-vacancy:

b. ½ H-terminated $LiCoPO_4$ → ½ H-terminated $LiCoPO_4$-vacant + Co (3.9)

This procedure does not remove a complete unit cell and therefore is distinct from the overall thermodynamic energy associated with complete dissolution of the material. We previously used similar methodology for $LiCoO_2$.[54] For $LiCoPO_4$ at pH = 7, our calculations yield ΔG for initial release of Co from the $LiCoO_2$(010) surface to be -0.87 eV. As a point of comparison, using the same methodology[54] for $LiCoO_2$ at the same pH and the removing the same fraction of Co atoms, the energy associated with initial release of a Co is +1.15 eV. This indicates that in pure water (i.e., in the absence of any reducing agents), the initial release of Co from the $LiCoO_2$(001) surface is much less favorable than release from the $LiCoPO_4$(010) surface.

Density functional theory (DFT) calculations were carried out using the Quantum Espresso open source suite.[55, 56] Exchange-correlation energies were approximated using GGA-PBE functional.[57] As pure DFT is known to over-delocalize the charge density, a remedial Hubbard U correction term of 5.00 eV magnitude was applied to Co^{2+} sites.[58-60] To describe atomic species GBRV ultra-soft pseudopotentials were employed.[61] In accordance with the criteria set for the pseudopotentials used, a plane-wave cutoff of 40 Ry for the wavefunction and 320 Ry for the charge density was selected for Kohn-Sham states. To account for the effect of unpaired electrons in Co(II), spin-polarization effects were included in the calculations. During the geometry optimization calculations, all the atoms in the structures were fully relaxed until the residual of forces was smaller than 5 $meV \cdot Å^{-2}$ per atom. For bulk calculations, the orthorhombic *Cmcm* phase of $LiCoPO_4$ was relaxed using a 6 × 4 × 6 grid of *k*-points and the obtained lattice constants were $a = 5.54$ Å (-2.21%), $b = 8.29$ Å (-1.59%), and $c = 6.26$ Å (-0.64%), in agreement with their experimental analogues of $a = 5.42$ Å, $b = 8.16$ Å and $c = 6.22$ Å.[62] The overprediction of the lattice constants by up to ~2% is attributable to the inherent shortcomings of the GGA-PBE exchange-correlation functionals.[63] The optimized bulk structure was cut along the (010) plane afterwards to create a P-1 slab possessing 3 Co layers. The resulting surface was expanded along the y axis to create a 1 × 2 supercell, providing four Co sites on each of its topmost layers (Figure 3.16). The generated slab has the dimensions of 6.26 × 11.07 × 12.57 $Å^3$. 25 Å of vacuum was inserted along the cleaved plane to evade undesirable interactions between periodic images of surfaces exposed. A 4 × 4 × 1 and a 4 × 2 × 1 mesh was used to sample the reciprocal space for 1 × 1 and 1 × 2 slabs, respectively. All slab models have inversion symmetry and are optimized in accord with the best available practices for such calculations.[64, 65]

To quantify the energetics of dissolution, we turn our attention to ΔG of the cation release process. We use a combination of first-principles calculations and thermodynamics experimental data to obtain the cation release energetics. Our approach has, in the recent past, been successfully applied to several cases of release process in a wide variety of Li-ion rechargeable battery cathode materials, ranging from $LiCoO_2$ (LCO)[55] to $LiNi_{1/3}Mn_{1/3}Co_{1/3}O_2$ (NMC)[66] and its compositionally tuned variants.[67, 68] In this approach, we divide the overall ΔG into two sub-terms. ΔG_1 sub-term which accounts for the energy penalty to be paid to remove the transition metal from the lattice structure. This term is obtained by calculating the $\sum E_{\text{products}}$ - $\sum E_{\text{reactants}}$ where DFT total energies are related to Gibbs free energies by accouting for zero-point energy and vibrational contributions, and all terms are purely DFT-calculable. As the (010) surface of $LiCoPO_4$ has an exposed layer of under-coordinated Co sites, the removal of this site dictates the magnitude of the ΔG_1**.** The thermodynamics pathway for this term starts with the surface terminated with a half-layer (50% occupancy) of Li atoms; this structure corresponds to the electrically charge-neutral surface that would be produced by cleavage through a layer of Li atoms, with half the Li atoms going to each opposing surface. In water, this surface undergoes a Li/H ligand exchange that leaves a ½ H-terminated surface, as shown in Eq. 3.8. In the next step, a cation is removed from the ½ H-terminated surface, yielding a $LiCoPO_4$ with a surface Co vacancy, denoted as $LiCoPO_4$-vacant, as shown in Eq. 3.9.

Since the created slab is a 1 × 2 supercell, it has 4 exposed penta-coordinated Co sites in its outermost layers (Figure 3.16). Therefore, the removal of one exposed Co from each side of the slab translates to a vacancy density of 25% per surface. Total ΔG_1 is the sum of the energetics of products minus those of reactants for the sum of steps a and b above, including the ZPE correction. The total energies of Li, Co, and H are computed based on their DFT atomic energetics predicted at their standard states, namely, $Li_{(s)}$, $Co_{(s)}$, and $H_{2(g)}$. The indirect outcome of this choice for the energetics of the elemental species, is that ΔG_1 is a measure of lattice stability upon the release of Co.

ΔG_2, which accounts for the energy given off upon the hydrolysis of released species, is purely based on experimental data. This term is computed using the Nernst equation:

$$\Delta G_2 = \Delta G^0_{SHE} - n_e e U_{SHE} - 2.303 n_{H^+} k_B T pH + k_B T \ln a^{z-}_{H_x A O_y} \tag{3.10}$$

In the above equation, ΔG°_{SHE} is the change in free energy of the aqueous species with respect to their standard states, referenced to the Standard Hydrogen Electrode (SHE). These values are tabulated in the literature.[69] We have also included them in Table 3.6. n_e is the number of electrons in the half-reactions for each species starting with their standard state, transforming to their oxidized forms under aqueous conditions. e is the charge of electron and U_{SHE} is the applied potential (set to zero here), n_{H+} is the number of protons associated with the oxidation chemical half-reactions considered for each species. $H_xAO_y^{z-}$ denotes the concentration of the constituent ions, assumed here to be 1×10^{-6} M, in line with the experimental data formerly reported for similar release experiments.[70]

In discussing the ΔG_2 terms, it is noteworthy that the values for Li^+ and Co^{2+} are the pH-independent while those of H and O, as H_2O, are pH-dependent. Table 3.6 contains the total values of ΔG_2 various terms for the relevant species utilized in this work to predict the free energies of release from the $LiCoPO_4$ surface at neutral pH. Pourbaix diagrams show that $Li^+_{(aq)}$ and $Co^{2+}_{(aq)}$ are the dominant speciations for, respectively, Li and Co elements at up to neutral pH. The chemical reactions giving rise to ΔG^0_{SHE} for Li, H_2, Co, and O_2 are:

$Li_{(s)} \rightarrow Li^+_{(aq)} + e^-$

$\frac{1}{2} H_{2(g)} \rightarrow H^+_{(aq)} + e^-$

$Co_{(s)} \rightarrow Co^{2+}_{(aq)} + 2e^-$

$O_2 + 4H^+ + 4e^- \rightarrow 2H_2O$

3.5.8 Supporting figures.

Table 3.2. Reagent information.

Reagent	**Supplier**	**Purity (%)**
Magnesium chloride anhydrous	Alfa Aesar	99.0%
Dextrose (D-glucose)	Sigma Aldrich	99.5%
Indium foil	Sigma Aldrich	99.995%
Nitric acid	Sigma Aldrich	70.0%
Cobalt (II) choride hexahydrate	Sigma Aldrich	98.0%
Ammonium chloride	Sigma Aldrich	99.5%
NAD^+ free acid	Sigma Aldrich	99.9%
Ophthalmic acid	Sigma Aldrich	97.0%
L-Glutathione, reduced	Sigma Aldrich	98.0%
Tetraethylene glycol	Sigma Aldrich	99.0%
Magnesium sulfate	Sigma Aldrich	99.5%
Lithium hydroxide hydrate	Sigma Aldrich	98.0%
Cobalt (II) acetate tetrahydrate	Sigma Aldrich	98.0%
Anhydrous phosphoric acid	Sigma Aldrich	99.999%

Table 3.3. Composition of model bacterial growth medium “minimal medium” with dextrose used for nanoparticle dissolution experiments.

Component	**Concentration (mM)**
NaCl	11.6
HEPES	10.0
Dextrose (D-glucose)	10.0
KCl	4.0
Na_2SO_4	2.8
NH_4Cl	2.8
$MgCl_2$	1.4
Na_2HPO_4	0.088
$CaCl_2 \cdot H_2O$	0.051

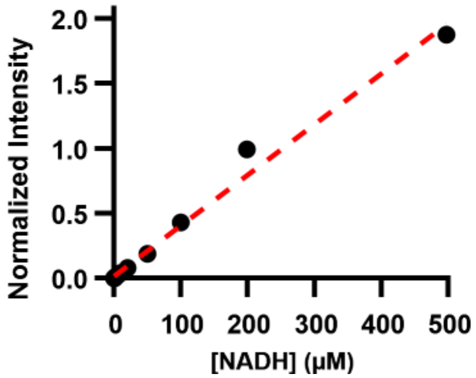

Figure 3.8. Fluorescence calibration curve of standard NADH solutions. Y = (0.00395 ± 0.00015)X, R^2 = 0.9850, n = 12.

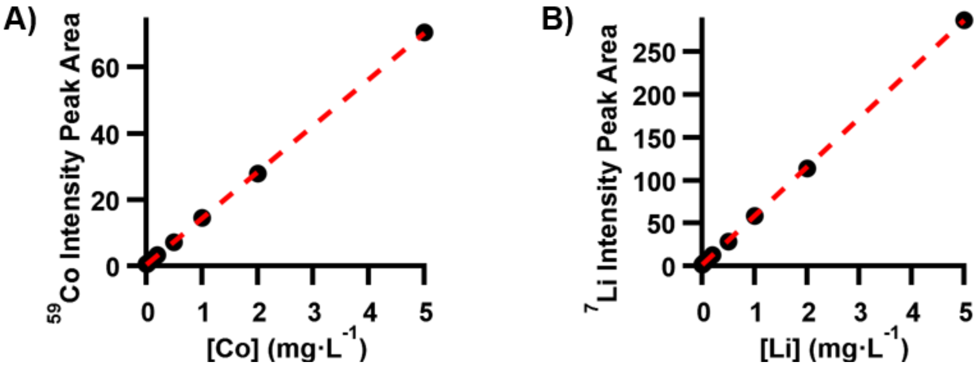

Figure 3.9. Representative ICP-MS standard calibration curves for quantifying A) Co, Y = (13.98 ± 0.04)X + (0.40 ± 0.08), R^2 = 0.99992, and B) Li, Y = (57.1 ± 0.2)X + (1.2 ± 0.3), R^2 = 0.99994. Standards were prepared by serial dilution from certified reference standards (1 g·L^{-1}, Sigma Aldrich).

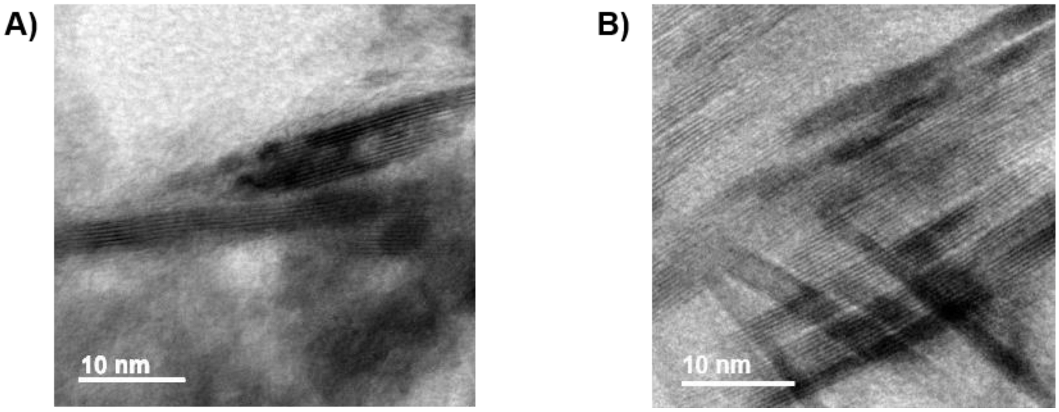

Figure 3.10. Transmission electron microscope (TEM) images of $LiCoO_2$ nanoparticles A) before and B) after exposure to minimal medium. Samples were washed twice for 20 min in nanopure water and drop-casted on a copper grid (Ted Pella, carbon type-B 300 mesh). Images taken on a JEO 2100 CRYO TEM with accelerating voltage at 200 kV and single-tilt holder.

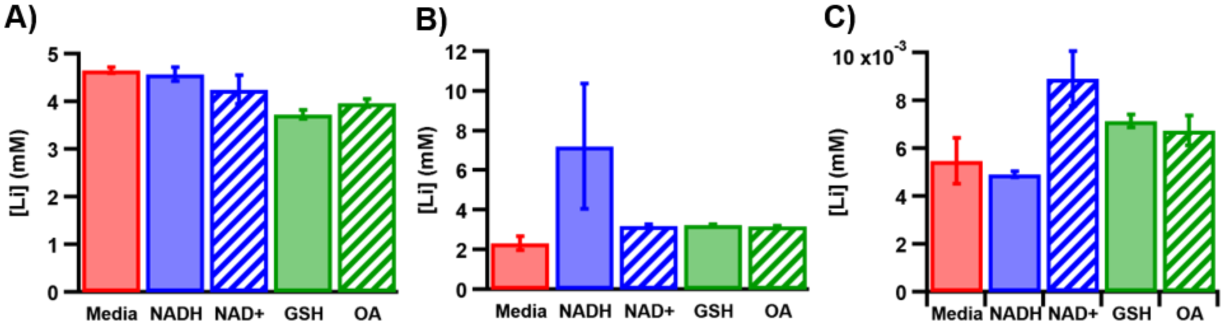

Figure 3.11. Dissolved Li concentrations in minimal medium solutions for A) $LiCoO_2$, B) $LiCoPO_4$, and C) $Co(OH)_2$ after 24-hr exposure to each molecule under study. A small amount of Li is present in $Co(OH)_2$ solutions as impurities within the synthesis (LiOH used to basify the solution) or within the commercial salts used to prepare minimal medium.

Table 3.4. Measured pH of solutions containing the indicated molecule before and after 24 hr exposure to the indicated nanoparticles in minimal medium. Uncertainty for the pH probe used is estimated at pH ± 0.02.

Nanoparticle	**Molecule**	**Initial pH**	**Final pH**	**ΔpH**
$LiCoO_2$	None	5.33	7.15	1.82
$LiCoO_2$	NADH	5.18	7.32	2.14
$LiCoO_2$	NAD^+	4.61	7.16	2.55
$LiCoO_2$	GSH	4.52	7.16	2.64
$LiCoO_2$	OA	4.57	7.14	2.57
$Co(OH)_2$	None	5.33	7.50	2.17
$Co(OH)_2$	NADH	5.18	7.46	2.28
$Co(OH)_2$	NAD^+	4.61	7.44	2.83
$Co(OH)_2$	GSH	4.52	7.32	2.80
$Co(OH)_2$	OA	4.57	7.47	2.90
$LiCoPO_4$	None	5.80	6.85	1.05
$LiCoPO_4$	NADH	5.51	7.49	1.98
$LiCoPO_4$	NAD^+	4.63	6.74	2.11
$LiCoPO_4$	GSH	4.46	6.74	2.28
$LiCoPO_4$	OA	4.57	6.78	2.21

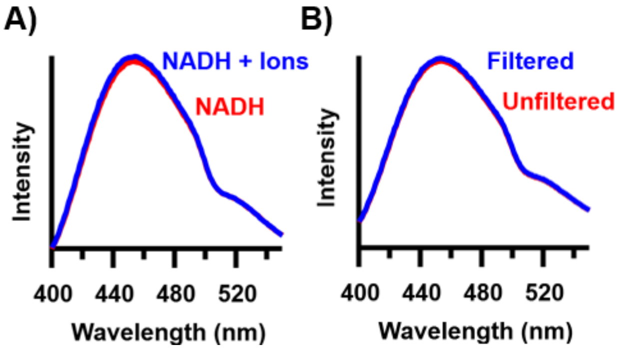

Figure 3.12. Fluorescence spectra of 0.5 mM NADH in minimal medium: A) after a 24-h period with (blue) and without (red) Co and Li ions, and B) before (red) and after (blue) filtration. There are no observed decreases in NADH fluorescence from filtration or exposure to Co^{2+} and Li^+ ions.

Table 3.5. Molar absorptivities of NADH and NAD$^+$ (1 – 100 µM) in pure water.

Species	$\varepsilon_{203\ \mathrm{nm}}$ **(cm^{-1}·M^{-1})**	$\varepsilon_{259\ \mathrm{nm}}$ **(cm^{-1}·M^{-1})**	$\varepsilon_{339\ \mathrm{nm}}$ **(cm^{-1}·M^{-1})**
NADH	$(30.9 \pm 0.9)\times10^3$	$(13.1 \pm 0.1)\times10^3$	$(5.12 \pm 0.03)\times10^3$
NAD$^+$	$(27.8 \pm 0.4)\times10^3$	$(15.3 \pm 0.3)\times10^3$	$(0.018 \pm 0.004)\times10^3$

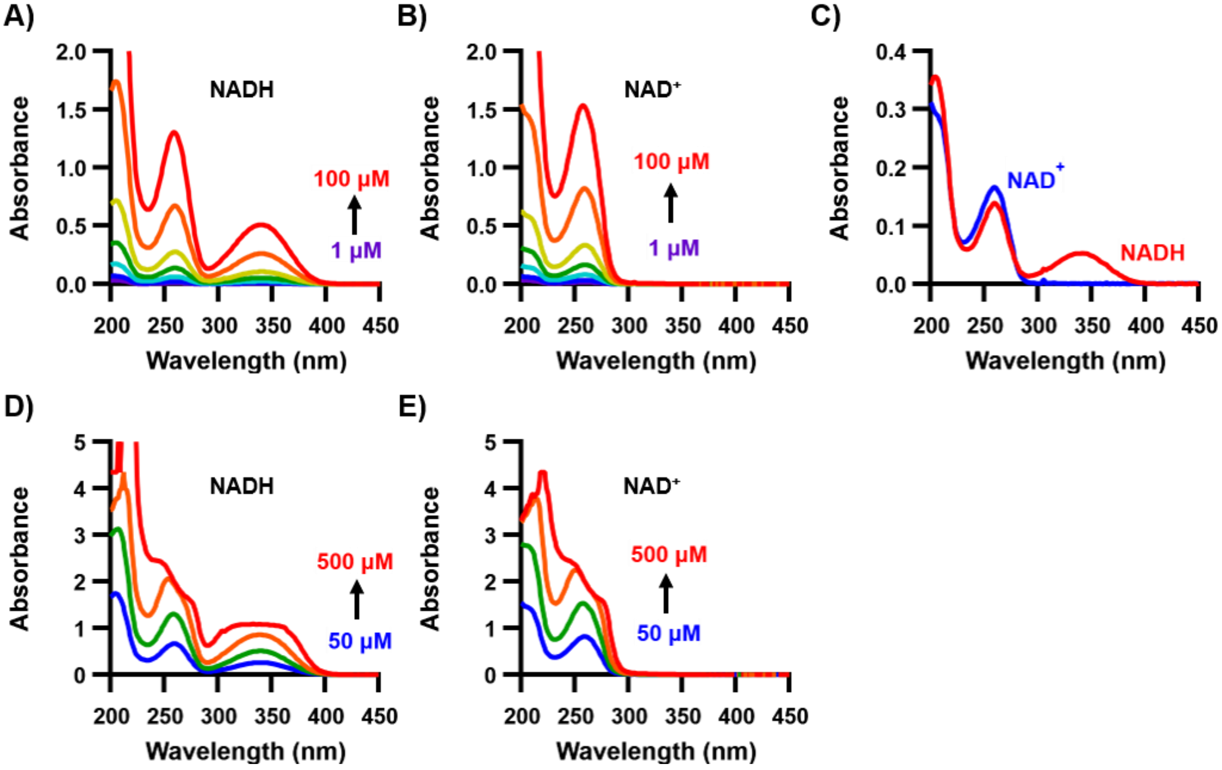

Figure 3.13. UV-visible absorbance spectra of standard solutions in nanopure water: A-B) NADH and NAD$^+$ (respectively) in the linear range of 1 µM to 100 µM, C) 10 µM NADH and NAD$^+$ spectra comparing absorbances at 259 nm and 339 nm, D-E) NADH and NAD$^+$ (respectively) in a higher concentration range showing shifts in lower wavelength peaks.

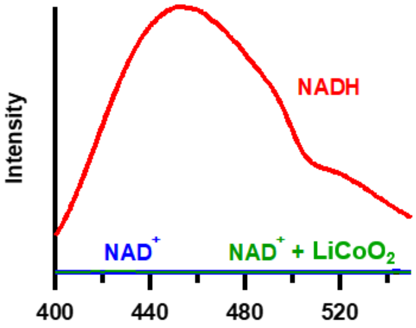

Figure 3.14. Fluorescence spectra of solutions containing NADH (red), NAD$^+$ (blue), and NAD$^+$ after 24-hr exposure to LiCoO$_2$ nanoparticles (green). Both NAD$^+$ solutions (blue and green) overlap near baseline, insignificant compared to NADH fluorescence.

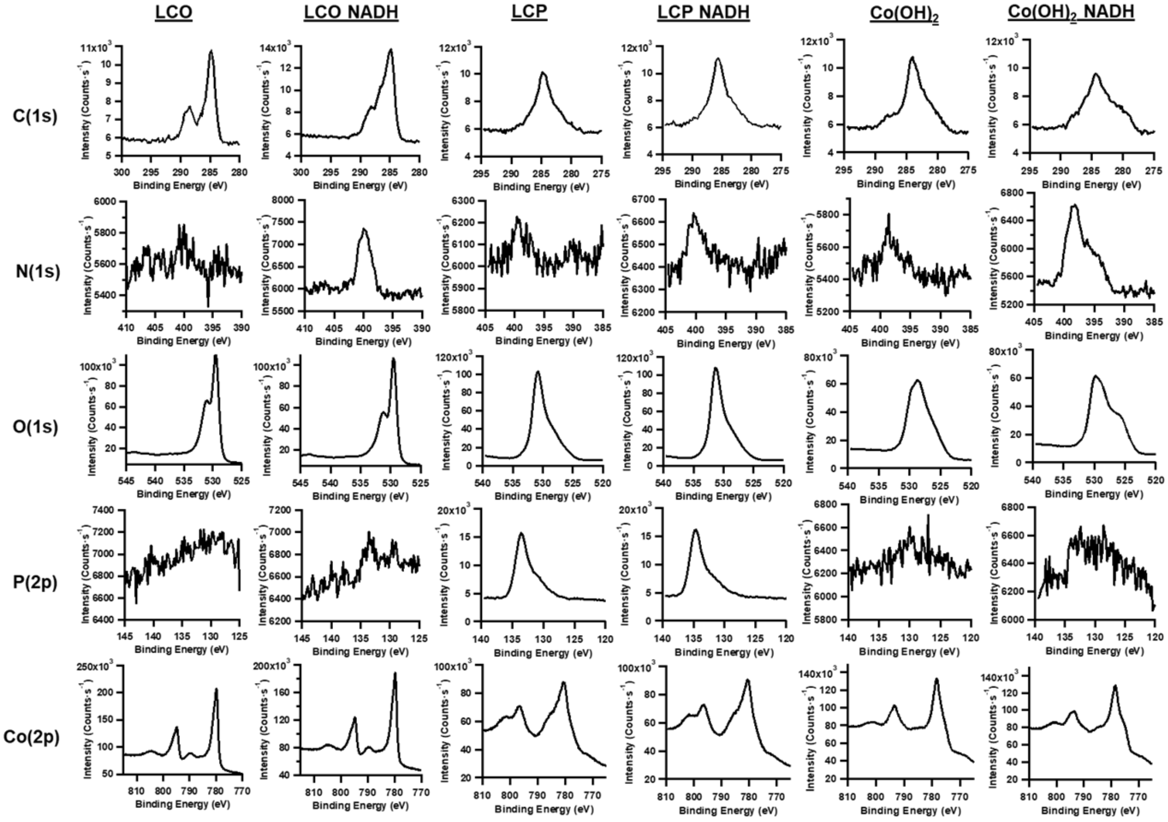

Figure 3.15. Representative XPS spectra for LiCoO$_2$ (LCO), LiCoPO$_4$ (LCP), and Co(OH)$_2$ nanoparticles pressed into indium foil after soaking for 24 hr in aqueous solutions with or without 0.5 mM NADH, arranged by the atomic transition measured. High-resolution spectra were obtained summing 10 (Co(2p)), 20 (O(1s) and C(1s)), or 50 (N(1s) and P(2p)) scans with step size of 0.2 eV and pass energy of 50 eV.

Table 3.6. Experimental[66] ΔG^0_{SHE} values of each aqueous species and their respective ΔG_2 at pH = 7.

Reactants	Product	ΔG^0_{SHE} (eV)	ΔG_2 (eV) at pH = 7
$Li_{(s)}$	Li^+	-3.039	-3.394
$H_{2(g)}$	H^+	0	-0.414
$Co_{(s)}$	Co^{2+}	-0.563	-0.918
½ O_2(g), $2H^+$	H_2O	-2.458	-1.632

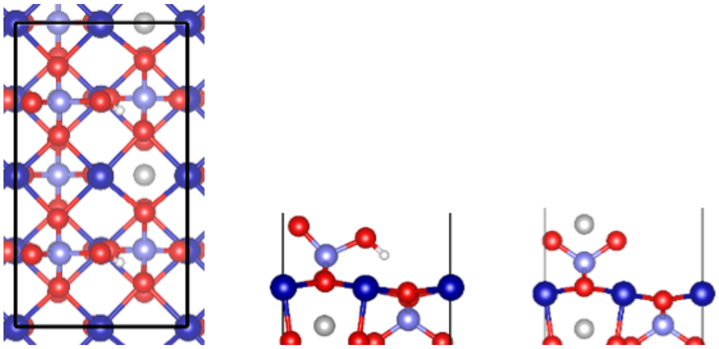

Figure 3.16. Top-view along *c* (left) and side-view along *b* (middle and right) of 1 × 2 supercells of ½ H-terminated (left and middle) and ½ Li-terminated (right) slabs used for surface calculations. Dark blue, light blue, grey, red, and white spheres are Co, P, Li, O and H, respectively.

3.6 References.

1. Hang, M. N.; Gunsolus, I. L.; Wayland, H.; Melby, E. S.; Mensch, A. C.; Hurley, K. R.; Pedersen, J. A.; Haynes, C. L.; Hamers, R. J., Impact of Nanoscale Lithium Nickel Manganese Cobalt Oxide (NMC) on the Bacterium Shewanella oneidensis MR - 1. *Chem.Mater.* **2016**, *28*, 1092-1100.

2. Hang, M. N.; Hudson-Smith, N. V.; Clement, P. L.; Zhang, Y.; Wang, C.; Haynes, C. L.; Hamers, R. J., Influence of Nanoparticle Morphology on Ion Release and Biological Impact of Nickel Manganese Cobalt Oxide (NMC) Complex Oxide Nanomaterials. *Appl. Nano Mater.* **2018**, *1*, 1721-1730.

3. Drever, J. I.; Stillings, L. L., The Role of Organic Acids in Mineral Weathering. *Colloids and Surfaces A: Physicochemical and Engineering Aspects* **1997**, *120*, 167-181.

4. Huang, W. H.; Keller, W. D., Dissolution of Rock-forming Silicate Minerals in Organic Acids: Simulated First-stage Weathering of Fresh Mineral Surfaces. *Am. Mineral.* **1970**, *55*, 2076-2094.

5. Houben, G. J., Iron Oxide Incrustations in Wells. Part 2: Chemical Dissolution and Modelling. *Appl.Geochem.* **2003**, *18*, 941-954.

6. Flynn, E. D.; Catalano, J. G., Reductive Transformations of Layered Manganese Oxides by Small Organic Acids and the Fate of Trace Metals. *Geochimica et Cosmochimica Acta* **2019**, *250*, 149-172.

7. Gu, B.; Dong, W.; Liang, L.; Wall, N. A., Dissolution of Technetium(IV) Oxide by Natural and Synthetic Organic Ligands under both Reducing and Oxidizing Conditions *Environ. Sci. Tech.* **2011**, *45*, 4771-4777.

8. Brown, G. E.; Henrich, V. E.; Casey, W. H.; Clark, D. L.; Eggleston, C.; Felmy, A.; Goodman, D. W.; Gratzel, M.; Maciel, G.; McCarthy, M. I.; Nealson, K. H.; Sverjensky, D. A.; Toney, M. F.; Zachara, J. M., Metal Oxide Surfaces and Their Interactions with Aqueous Solutions and Microbial Organisms *Chem. Rev.* **1999**, *99*, 77-174.

9. Nealson, K. H.; Saffarini, D., Iron and Manganese in Anaerobic Respiration - Environmental Significance, Physiology, and Regulation. *Annu. Rev. Microbiol.* **1994**, *48*, 311-343.

10. Lower, S. K.; Hochella, M. F.; Beveridge, T. J., Bacterial Recognition of Mineral Surfaces: Nanoscale Interactions Between Shewanella and Alpha-FeOOH. *Science* **2001**, *292*, 1360-1363.

11. Zeng, X.; Li J.; Liu, L., Solving Spent Lithium-ion Battery Problems in China: Opportunities and Challenges. *Renew. Sustain. Energy Rev.* **2015**, *52*, 1759-1767.

12. Beyersmann D.; Hartwig, A., Carcinogenic Metal Compounds: Recent Insight into Molecular and Cellular Mechanisms. *Arch. Toxicol.* **2008**, *82*, 493-512.

13. Paustenbach, D. J.; Tvermoes, B. E.; Unice, K. M.; Finley B. L.; Kerger, B. D., A Review of the Health Hazards Posed by Cobalt. *Crit. Rev. Toxicol.* **2013**, *43*, 316-362.

14. Gayer, K. H.; Garrett, A. B., The Solubility of Cobalt Hydroxide, $Co(OH)_2$, in Solutions of Hydrochloric Acid and Sodium Hydroxide at 25 Degrees. *J. Am. Chem. Soc.* **1950**, *72*, 3921-3923.

15. Chivot, J.; Mendoza, L.; Mansour, C.; Pauporte T.; Cassir, M., New Insight in the Behaviour of Co-H_2O System at 25-150 degrees C, Based on Revised Pourbaix Diagrams. *Corrosion Sci.* **2008**, *50*, 62-69.

16. Lin, S.-J.; Guarente, L., Nicotinamide Adenine Dinucleotide, a Metabolic Regulator of Transcription, Longevity and Disease. *Curr. Opin. Cell Biol.* **2003**, *15*, 241-246.

17. Sies, H., Glutathione and its Role in Cellular Functions. *Free Radical Biol. Med.* **1999**, *27*, 916-921.

18. Liu, X.; Sen, S.; Liu, J.; Kulaots, I.; Geohegan, D.; Kane, A.; Puretzky, A. A.; Rouleau, C. M.; More, K. L.; Palmore, G. T. R.; Hurt, R. H., Antioxidant Deactivation on Graphenic Nanocarbon Surfaces. *Small* **2011**, *7*, 2775-2785.

19. Wang, Y.; Basdogan, Y.; Zhang, T.; Lankone, R. S.; Wallace, A. N.; Fairbrother, D. H.; Keith, J. A.; Gilbertson, L. M., Unveiling the Synergistic Role of Oxygen Functional Groups in the Graphene-Mediated Oxidation of Glutathione. *Appl. Mater. Interfaces* **2020**, *12,* 45753-45762.

20. Laudadio, E. D.; Ilani-kashkouli, P.; Green, C. M.; Kabengi, N. J.; Hamers, R. J., Interaction of Phosphate with Lithium Cobalt Oxide Nanoparticles: A Combined Spectroscopic and Calorimetric Study *Langmuir* **2019**, *35*, 16640-16649.

21. Laudadio, E. D.; Bennett, J. W.; Green, C. M.; Mason, S. E.; Hamers, R. J., Impact of Phosphate Adsorption on Complex Cobalt Oxide Nanoparticle Dispersibility in Aqueous Media. *Environ. Sci. Tech.* **2018**, *52*, 10186-10195.

22. Kreder III, K. J.; Assat, G.; Manthiram, A., Microwave-Assisted Solvothermal Synthesis of Three Polymorphs of $LiCoPO_4$ and Their Electrochemical Properties. *Chem. Mater.* **2015**, *27*, 5543-5549.

23. Brunauer, S.; Emmett, P. H.; Teller, E., Adsorption of Gases in Multimolecular Layers. *J. Am. Chem. Soc.* **1938**, *60*, 309-319.

24. Xiao, W.; Wang, R. S.; Handy, D. E.; Loscalzo, J., NAD(H) and NADP(H) Redox Couples and Cellular Energy Metabolism. *Antiox. Redox Signaling* **2018**, *28*, 251-272.

25. Reiss, P. D.; Zuurendonk, P. F.; Veech, R. L., Measurement of Tissue Purine, Pyrimidine, and Other Nucleotides by Radial Compression High-Performance Liquid Chromatography. *Anal. Biochem.* **1984**, *140*, 162-171.

26. Yamada, K.; Hara, N.; Shibata, T.; Osago, H.; Tsuchiya, M., The Simultaneous Measurement of Nicotinamide Adenine Dinucleotide and Related Compounds by Liquid Chromatography / Electrospray Ionization Tandem Mass Spectrometry. *Anal. Biochem.* **2006**, *352*, 282-285.

27. Wu, G.; Fang, Y.-Z.; Yang, S.; Lupton; J. R.; Turner, N. D., Glutathione Metabolism and Its Implications for Health. *J. Nutrition* **2004**, *134*, 489-492.

28. Chance, B.; Schoener, B.; Oshino, R.; Itshak, F.; Nakase, Y., Oxidation-Reduction Ratio Studies of Mitochondria in Freeze-trapped Samples. *J. Biol. Chem* **1979**, *254*, 4764-4771.

29. Rehman, A. U.; Anwer, A. G.; Gosnell, M. E.; Mahbub, S. B.; Liu, G.; Goldys, E. M., Fluorescence Quenching of Free and Bound NADH in HeLa Cells Determined by Hyperspectral Imaging and Unmixing of Cell Autofluorescence. *Biomed. Optics Express* **2017**, *8*, 1488-1498.

30. Shirley, D. A., High-resolution X-ray Photoemission Spectrum of the Valence Bands of Gold. *Phys. Rev. B* **1972**, *5*, 4709-4714.

31. Takahashi, Y.; Kijima, N.; Dokko, K.; Nishizawa, M.; Uchida, I.; Akimoto, J., Structure and Electron Density Analysis of Electrochemically and Chemically Delithiated $LiCoO_2$ Single Crystals. *J. Solid State Chem.* **2007**, *180*, 313-321.

32. Lotmar, W.; Feitknecht, W., Uber Anderungen der Ionenabstande in Hydroxd-Schichtengittern. **1936**, 368-378.

33. Bergerhoff, G.; Brown, I. D., Lithium Cobalt Phosphate. **1987**.

34. Lamas, D. G.; Neto, M. D. O.; Kellermann, G.; Craievich, A. F., Nanocharacterization Techniques. Elsevier Inc., **2017**, 111-182.

35. Wilson, D. F.; Erecinska, M.; Dutton, P. L., Thermodynamic Relationships in Mitochondrial Oxidative Phosphorylation. *Annu. Rev. Biophys. Bioeng.* **1974**, *3*, 203-230.

36. Millis, K. K.; Weaver, K. H.; Rabenstein, D. L., Oxidation / Reduction Potential of Glutathione. *J. Org. Chem.* **1993**, *58*, 4144-4146.

37. Shkrob, I. A.; Gilbert, J. A.; Phillips, P. J.; Klie, R.; Haasch, R. T.; Bareño, J.; Abraham, D. P., Chemical Weathering of Layered Ni-rich Oxide Electrode Materials: Evidence for Cation Exchange. *J. Electrochem. Soc.* **2017**, *164*, A1489-A1498.

38. Blank, L. M.; Ebert, B. E.; Buehler, K.; Bühler, B., Redox Biocatalysis and Metabolism: Molecular Mechanisms and Metabolic Network Analysis. *Antiox. Redox Signaling* **2010**, *13*, 349-394.

39. Johnson III, R. D., Computational Chemistry Comparison and Benchmark Database. *National Institute of Standards and Technology*, 2019.

40. Berner, R. A., Phosphate Removal from Sea Water by Adsorption on Volcanogenic Ferric Oxides. *Earth Planet. Sci. Lett.* **1973**, *18*, 77-86.

41. Wang, M.; Navrotsky, A., Enthalpy of Formation of $LiNiO_2$, $LiCoO_2$ and Their Solid Solution, $LiNi_{1-x}Co_xO_2$. *Solid State Ionics* **2004**, *166*, 167-173.

42. Yokokawa, H.; Sakai, N.; Yamaji, K.; Horita, T.; Ishikawa, M., Thermodynamic Determining Factors of the Positive Electrode Potential of Lithium Batteries. *Solid State Ionics* **1998**, *113*, 1-9.

43. Chen, C. H.; Chen Y. C.; Lin, M. S., Amperometric Determination of NADH with Co_3O_4 Nanosheet Modified Electrode. *Biosens. Bioelectron.* **2013**, *42*, 379-384.

44. Batley, G. E.; Kirby J. K.; McLaughlin, M. J., Fate and Risks of Nanomaterials in Aquatic and Terrestrial Environments. *Acc. Chem. Res.* **2013**, *46*, 854-862.

45. Shaw, W. H. R., Cation Toxicity and the Stability of Transition-Metal Complexes. *Nature* **1961**, *192*, 754-755.

46. Shi, L.; Dong, H.; Reguera, G.; Beyenal, H.; Lu, A.; Liu, J.; Yu, H. Q.; Fredrickson, J. K., Extracellular Electron Transfer Mechanisms between Microorganisms and Minerals. *Nat. Rev. Microbiol.* **2016**, *14*, 651-662.

47. Lloyd, J. R., Microbial Reduction of Metals and Radionuclides. *FEMS Microbiol. Rev.* **2003**, *27*, 411-425.

48. Gorby, Y. A.; Caccavo, F.; Bolton, H., Microbial Reduction of Cobalt(III)EDTA$^-$ in the Presence and Absence of Manganese(IV) Oxide. *Environ. Sci. Tech.* **1998**, *32*, 244-250.

49. Caccavo, F.; Lonergan, D. J.; Lovley, D. R.; Davis, M.; Stolz, J. F.; McInerney, M. J., Geobacter sulfurreducens sp. nov., a Hydrogen- and Acetate-oxidizing Dissimilatory Metal-reducing Microorganism. *Appl. Environ. Microbiol.* **1994**, *60*, 3752-3759.

50. Ying, W., NADH$^+$ and NADH in Cellular Functions and Cell Death. *Frontiers in Bioscience* **2006**, *11*, 3129-3148.

51. Papis, E.; Rossi, F.; Raspanti, M.; Dalle-Donne, I.; Colombo, G.; Milzani, A.; Bernardini, G.; Gornati, R., Engineered Cobalt Oxide Nanoparticles Readily Enter Cells. *Toxicol. Lett.* **2009**, *189*, 253-259.

52. Behl, B.; Papageorgiou, I.; Brown, C.; Hall, R.; Tipper, J. L.; Fisher, J.; Ingham, E., Biological Effects of Cobalt-chromium Nanoparticles and Ions on Dural Fibroblasts and Dural Epithelial Cells. *Biomaterials* **2013**, *34*, 3547-3558.

53. Melby, E. S.; Cui, Y.; Borgatta, J.; Mensch, A. C.; Hang, M. N.; Chrisler, B.; Dohnalkova, A.; Gilder, J. M. V.; Alvarez, C. M.; Smith, J. N.; Hamers, R. J.; Orr, G., Impact of Lithiated Cobalt Oxide and Phosphate Nanoparticles on Rainbow Trout Gill Epithelial Cells. *Nanotox.* **2018**, *12*, 1166-1181.

54. Abbaspour-Tamijani, A.; Bennett, J. W.; Jones, D. T.; Cartagena-Gonzalez, N.; Jones, Z. R.; Laudadio, E. D.; Hamers, R. J.; Santana, J. A.; Mason, S. E., DFT and Thermodynamics Calculations of Surface Cation Release in $LiCoO_2$. *Appl. Surf. Sci.* **2020,** *515*, 145865.

55. Giannozzi, P.; Andreussi, O.; Brumme, T.; Bunau, O.; Nardelli, M. B.; Calandra, M.; Car, R.; Cavazzoni, C.; Ceresoli, D.; Cococcioni, M.; Colonna, N.; Carnimeo, I.; Dal Corso, A.; de Gironcoli, S.; Delugas, P.; DiStasio, R. A.; Ferretti, A.; Floris, A.; Fratesi, G.; Fugallo, G.; Gebauer, R.; Gerstmann, U.; Giustino, F.; Gorni, T.; Jia, J.; Kawamura, M.; Ko, H. Y.; Kokalj, A.; Kucukbenli, E.; Lazzeri, M.; Marsili, M.; Marzari, N.; Mauri, F.; Nguyen, N. L.; Nguyen, H. V.; Otero-de-la-Roza, A.; Paulatto, L.; Ponce, S.; Rocca, D.; Sabatini, R.; Santra, B.; Schlipf, M.; Seitsonen, A. P.; Smogunov, A.; Timrov, I.; Thonhauser, T.; Umari, P.; Vast, N.; Wu, X.; Baroni, S., Advanced Capabilities for Materials Modelling with QUANTUM ESPRESSO. *J. Phys.-Condes. Matter* **2017,** *29*, 30.

56. Giannozzi, P.; Baroni, S.; Bonini, N.; Calandra, M.; Car, R.; Cavazzoni, C.; Ceresoli, D.; Chiarotti, G. L.; Cococcioni, M.; Dabo, I.; Dal Corso, A.; de Gironcoli, S.; Fabris, S.; Fratesi, G.; Gebauer, R.; Gerstmann, U.; Gougoussis, C.; Kokalj, A.; Lazzeri, M.; Martin-Samos, L.; Marzari, N.; Mauri, F.; Mazzarello, R.; Paolini, S.; Pasquarello, A.; Paulatto, L.; Sbraccia, C.; Scandolo, S.; Sclauzero, G.; Seitsonen, A. P.; Smogunov, A.; Umari, P.; Wentzcovitch, R. M., QUANTUM ESPRESSO: a Modular and Open-source Software Project for Quantum Simulations of Materials. *J. Phys.-Condes. Matter* **2009,** *21*, 19.

57. Perdew, J. P.; Burke, K.; Ernzerhof, M., Generalized Gradient Aapproximation Made Simple. *Phys. Rev. Lett.* **1996,** *77*, 3865-3868.

58. Anisimov, V. I.; Solovyev, I. V.; Korotin, M. A.; Czyzyk, M. T.; Sawatzky, G. A., Density-Functional Theory and Nio Photoemission Spectra. *Phys. Rev. B* **1993,** *48*, 16929-16934.

59. Anisimov, V. I.; Zaanen, J.; Andersen, O. K., Band Theory and Mott Insulators - Hubbard-U Instead of Stoner-I. *Phys. Rev. B* **1991,** *44*, 943-954.

60. Liechtenstein, A. I.; Anisimov, V. I.; Zaanen, J., Density-Functional Theory and Strong-Interactions – Orbital Ordering in Mott-Hubbard Insulators. *Phys. Rev. B* **1995,** *52*, R5467-R5470.

61. Garrity, K. F.; Bennett, J. W.; Rabe, K. M.; Vanderbilt, D., Pseudopotentials for High-throughput DFT Calculations. *Comput. Mater. Sci.* **2014,** *81*, 446-452.

62. Niggli, A., Die Raumgruppe von Na_2CrO_4. *Acta Crystallographica* **1954,** *7*, 776-776.

63. Haas, P.; Tran, F.; Blaha, P.; Schwarz, K.; Laskowski, R., Insight into the Performance of GGA Functionals for Solid-state Calculations. *Phys. Rev. B* **2009,** *80*, 13.

64. Corum, K. W.; Tamijani, A. A.; Mason, S. E., Density Functional Theory Study of Arsenate Adsorption onto Alumina Surfaces. *Minerals* **2018,** *8*, 18.

65. Tamijani, A. A.; Salam, A.; de Lara-Castells, M. P., Adsorption of Noble-Gas Atoms on the TiO_2(110) Surface: An Ab Initio-Assisted Study with van der Waals-Corrected DFT. *J. Phys. Chem. C* **2016,** *120*, 18126-18139.

66. Bennett, J. W.; Jones, D.; Huang, X.; Hamers, R. J.; Mason, S. E., Dissolution of Complex Metal Oxides from First-Principles and Thermodynamics: Cation Removal from the (001) Surface of $Li(Ni_{1/3}Mn_{1/3}Co_{1/3})O_2$. *Environ. Sci. Tech.* **2018,** *52,* 5792-5802.

67. Buchman, J. T.; Bennett, E. A.; Wang, C.; Tamijani, A.; Bennett, J. W.; Hudson, B. G.; Green, C. M.; Clement, P. L.; Zhi, B.; Henke, A. H.; Laudadio, E. D.; Mason, S. E.; Hamers, R. J.; Klaper, R. D.; Haynes, C. L., Nickel Enrichment of Next-generation NMC Nanomaterials Alters Material Sstability, Causing Unexpected Dissolution Behavior and Observed Toxicity to S. oneidensis MR-1 and D. magna. *Environ. Sci. Nano* **2020,** *7,* 571-587.

68. Bennett, J. W.; Jones, D. T.; Hamers, R. J.; Mason, S. E., First-Principles and Thermodynamics Study of Compositionally Tuned Complex Metal Oxides: Cation Release from the (001) Surface of Mn-Rich Lithium Nickel Manganese Cobalt Oxide. *Inorg. Chem.* **2018,** *57*, 13300-13311.

69. Wagman, D. D.; Evans, W. H.; Parker, V. B.; Schumm, R. H.; Halo, I.; Balley, S. M.; Churney, K. L.; Nuttal, R. L., NBS Tables of Chemical Thermodynamic Properties: Selected Values for Inorganic and C1 and C2 Organic Substances in SI Units. *J. Phys. Chem. Ref. Data* **1982,** *11*.

70. Huang, X.; Bennett, J. W.; Hang, M. N.; Laudadio, E. D.; Hamers, R. J.; Mason, S. E., Ab Initio Atomistic Thermodynamics Study of the (001) Surface of $LiCoO_2$ in a Water Environment and Implications for Reactivity under Ambient Conditions. *J. Phys. Chem. C* **2017,** *121*, 5069-5080.

Chapter 4. Understanding Reaction Mechanisms of Nicotinamide Adenine Dinucleotide (NADH) with Metal Oxide Nanomaterials

The following chapter is adapted from a manuscript in preparation with the co-authors Katherine Kruszynski, Elizabeth D. Laudadio, and Robert J. Hamers. Additional authors may be added as the work is in-progress. All of the data collection, data analysis, and writing were done by Austin H. Henke under the advisement of Robert J. Hamers except for the following: Katherine Kruszynski and Elizabeth D. Laudadio assisted with nanoparticle synthesis and characterization.

This work was supported by the National Science Foundation (NSF) under the Center for Sustainable Nanotechnology, CHE-2001611. The Center for Sustainable Nanotechnology is part of the NSF Centers for Chemical Innovation Program. The authors gratefully acknowledge use of University of Wisconsin facilities and instrumentation through the Research Science and Engineering Center (partially supported through NSF DMR-1720415) and Water Science and Engineering Laboratory. The authors also acknowledge Dr. Pamela Doolittle for assistance with ICP-MS measurements.

4.1 Introduction.

As discussed in Chapter 3, redox chemistry plays a central role in the transformation of nanomaterials and their potential for environmental toxicity. Metal oxides constitute one of the most widely used class of engineered nanomaterials, such as $LiCoO_2$ and a broader family of "NMC" compositions ($LiNi_xMn_yCo_{1-x-y}O_2$, x,y < 1) used in Li ion batteries. Released Co from $LiCoO_2$ is hazardous to cells on its own,[1] though the dissolution processes poses another threat. The crystal lattice of these materials may stabilize transition metal ions in oxidation states not thermodynamically favored in aqueous conditions. For example, Co exists in the +3 state within solid $LiCoO_2$, whereas Co(II) is by far the dominant species under standard aqueous conditions.[2] Therefore, upon Co release a redox reaction occurs between $LiCoO_2$ and the surrounding media. Several studies have investigated $LiCoO_2$ transformation and the effect of surrounding media to find that the dissolution reactions produce reactive oxygen species (ROS) and degrade surrounding biomolecules (e.g. proteins, DNA, metabolites).[3–8] Since metal oxide compounds absorb ultraviolet and/or visible light, photochemistry warrants consideration as a pathway for nanoparticle transformation and toxicity.[9] Therefore, it is pertinent to consider the exact electronic band structure of a material,[10] not simply the oxidation states of metal ions. Despite the large amount of prior work on metal oxide nanoparticle – biological interactions, no mechanism has been developed for reaction of small, redox-active biomolecules, such as NADH (Figure 4.1), with $LiCoO_2$ nanomaterials. Additionally, even though carbohydrates are frequently attached to metal oxide nanomaterials for various applications,[11–14] studies involving biological effects of high-valence metal oxides typically do not consider interaction with reducing sugars in the media.

We have shown above in sections 3.3 and 3.4 that $LiCoO_2$ and NADH transform one another via reductive Co release and NADH oxidation. Exposure to NADH in $LiCoO_2$ dissolution experiments shows correlated Co release and NADH oxidation. Our XPS binding experiments with NADH (section 3.3.5) suggest that the reaction occurs on the nanoparticle surface, supported by prior studies showing phosphate (a component of NADH) binds strongly to $LiCoO_2$.[15, 16] However, the specific mechanism is unclear. Questions remain, such as: Does coupled transformation of $LiCoO_2$ and NADH occur on the nanoparticle surface, or in solution with solubilized Co(III)? Is the nicotinamide moiety responsible for Co reduction? Is the phosphate moiety responsible for binding to the nanoparticle? Is the ribose moiety inert, or involved in the reaction? Do other components of the matrix (see Table 3.3) influence the reaction? To address these questions, we perform dissolution experiments with $LiCoO_2$ and control compounds exposed to NADH and several of its component molecules (Figure 4.1): D-ribose-5-phosphate ("Ribo") and 1-methyl-1,4-dihydronicotinamide ("Nico"). We hypothesized that if phosphate was responsible for surface attachment, Ribo would reproduce the binding observed from NADH, and that if the nicotinamide group was responsible for redox reaction, Nico would reproduce the enhanced Co release seen with NADH. If both binding and reducing strength are needed in the same molecule to see any effect, these experiments could show that NADH alone reacts with $LiCoO_2$. Furthermore, we tested particles exposed to both Nico and Ribo to see if there were synergistic effects to recapture what is seen with NADH. Our surprising results show that Ribo, not Nico, replicates the enhancement of $LiCoO_2$ dissolution seen by NADH. This suggests that surface attachment via the phosphate group in NADH is critical to $LiCoO_2$ redox dissolution, and that reducing sugars, such as ribose, must be considered when studying nanoparticle transformations in biological media.

We must also consider such nanoparticle-biomolecule interactions for compounds other than $LiCoO_2$. In Chapter 3, $LiCoO_2$ transformation with NADH is compared to the Co(II) compounds of $Co(OH)_2$ and $LiCoPO_4$ to show that a reduction reaction occurs in dissolution, though these are all Co-containing compounds. It is unclear if and how the observed $LiCoO_2$-NADH interaction extends to compounds of other metals, such as Ni, Mn, and Fe. Metal oxide minerals of different transition metals sometimes behave similarly in environmental transformations, such as coordination with small organic acids,[17–20] reduction by bacteria,[21–27] or effects of pH.[28] However, this may not be the case A) on the nanomaterial scale, B) with $LiCoO_2$ being a Li-intercalation compound, or C) since the reaction with NADH is potentially surface-driven (i.e., surface-specific). Here, we see that nano-scale Mn_2O_3 (Mn in +3 state) behaves similarly to $LiCoO_2$ when exposed to NADH in that both show increased ion release and oxidize NADH. On the other hand, nano-scale NiO (Ni in +2 state) behaves similarly to $Co(OH)_2$ when exposed to NADH in that both show little change in ion release and do not oxidize NADH. These observations are consistent not only with metal oxidation state, but also with predictions of Mn_2O_3 and NiO nanomaterial toxicity towards model organisms, or lack thereof, based on band structure.[10] This shows that the coupled transformation of redox-active biomolecules and high-valence metal oxides extends beyond $LiCoO_2$.

4.2 Experimental.

4.2.1 Nanoparticle synthesis and characterization.

We synthesized sheet-like nanoparticles of cobalt hydroxide, $Co(OH)_2$, and $LiCoO_2$ following procedures we described previously.[15, 16] $Co(OH)_2$ nanosheets were prepared via a precipitation method. The Co(OH)2 precursor was converted to Li_xCoO_2 using a molten salt flux of 6:4 molar ratio of $LiNO_3$:LiOH at 200 °C. All solutions in this study were prepared from nanopure water (Barnstead Genpure System, $\rho \geq 18.2$ MΩ·cm). Detailed procedures for nanoparticle syntheses are found in section 3.5.2. Mn_2O_3

(~50 nm diameter) and NiO (~80 nm diameter) nanoparticles were obtained from U.S. Research Nanomaterials. The supplier labeled these materials as MnO_2 and Ni_2O_3, respectively, however XRD analysis revealed the particles to be Mn_2O_3 and NiO, which is what we refer to from this point. CoO (95% powder) was obtained from Alfa Aesar and used along with $Co(OH)_2$ as a control Co(II) compound. Notably, while CoO contains Co in the +2 state, Zhang et al.[10] predicted this compound to display oxidative stress toxicity based on band structure. Therefore, experiments with CoO could determine whether metal oxidation state or band structure influence redox-related toxicity. Unlike the other materials, CoO is not specified as nano-scale. As seen in section 4.3.2, the decreased surface area compared to the other particles does not impede its ability to dissolve.

Powder X-ray diffraction (XRD) patterns were obtained for each sample using a Bruker D8 Advance diffractometer equipped with a copper Kα source and 6 mm slit width. Samples for XRD analysis were prepared by affixing nanoparticle powder onto a B-doped silicon crystal zero-diffraction plate (MTI Corporation) with vacuum grease. Specific surface area measurements of ~0.1 g vacuum-dried samples were determined by nitrogen physisorption (Micromeritics Gemini VII 2390 surface area analyzer) and Brunauer-Emmett-Teller (BET) analysis.[29] Several characterization experiments, namely scanning electron microscopy, dynamic light scattering (DLS), and laser Doppler microelectrophoresis, have not yet been completed but are planned to gain information into particle morphology, size, and surface charge, respectively (see section 4.4).

4.2.2 Dissolution studies with nanoparticles and biomolecules.

A model bacterial growth medium with minimal constituents (“minimal medium” with dextrose) was prepared in nanopure water with various salts, 4-(2-hydroxyethyl)-1-piperazineethanesulfonic acid (HEPES) buffer, and dextrose. See Table 3.2 for chemical information and Table 3.3 for the full composition of minimal medium with dextrose. We recognize that minimal medium used may not fully replicate the complex environment inside cells, perhaps warranting further investigations. However, this medium does provide a relatively simple matrix to investigate the specific interactions of NADH and other molecules with the nanomaterials of interest. Additionally, while NADH is typically unable to transverse membranes, there is evidence that lower concentrations of NADH can exist in extracellular matrices via transmembrane protein transport or other mechanisms.[30] It follows that our conclusions do not rely on nanomaterials entering cells. This is the same matrix used in Chapter 3.

NADH reduced disodium salt (Sigma Aldrich), 1-methyl-1,4-dihydronicotinamide (Cayman Chemical), and D-ribosephosphate disodium salt (Sigma Aldrich) were obtained from commercial sources and used as received. Solutions were prepared for each molecule of interest by dissolving 0.5 mM in minimal medium. This concentration was chosen because it is relevant to concentrations of these molecules found in certain cells[31, 32] and produces suitable fluorescence signals for NADH/Nico solutions. In the case of solutions with Ribo and Nico combined, this was 0.5 mM for each molecule. Nanoparticles were introduced to each solution at 1 $mg \cdot mL^{-1}$ nanoparticle concentration, using vials of approximately 3 mL. The sealed vials were covered from light and shaken for 24 h. The samples were then centrifuged at 13,100·g for 20 min (Eppendorf MiniSpin plus). Finally, the supernatant was collected and filtered through 0.1 μm porosity syringe filter cartridges (Millex VV) to ensure nanoparticle removal (see section 3.2.2 for further justification). All experiments were performed in at least triplicate and error bars represent standard error of the mean.

4.2.3 Quantifying NADH and Nico via fluorescence.

The concentration of NADH in samples was determined via fluorescence using an ISS K2 photon-counting spectrofluorimeter, using measurement conditions similar to those reported previously.[33, 34] Samples were placed in a fused silica cuvette at room temperature, excited at $\lambda_{ex} = 338$ nm, and the emission spectrum was measured between $\lambda_{em} = 400$ and $\lambda_{em} = 550$ nm with a step size $\Delta\lambda = 1$ nm and integration time of 1 s per step. NADH exhibits an emission peak at $\lambda em \approx 455$ nm, whereas the oxidized NAD^+ does not. The intensity was background-subtracted using a blank consisting of minimal medium with dextrose. Spectra were also normalized to the fluorescence of a solid tetraphenylbutadiene (TPB) standard to account for variations in lamp intensity. NADH was quantified by converting the fluorescence intensity to concentration using a calibration curve.

Solutions of Nico were treated in the same manner, except with different excitation/emission wavelengths determined experimentally. 1-Methyl-1,4-dihydronicotinamide contains the same fluorescent nicotinamide moiety as NADH, yet to our knowledge its fluorescence has not been reported previously. Spectral properties of 0.5 mM Nico were determined in an excitation-emission matrix from the range of λ_{ex} = 300 – 400 nm and λ_{em} = 340 – 540 nm (Figure 4.2). From this experiment, we determined optimal analysis conditions of λ_{ex} = 328 nm and λ_{em} = 340 – 440 nm (with maximum around 382 nm). To ensure that the fluorescence of Nico is tied to its redox state (as is with NADH), we performed a positive oxidation control by exposing Nico to 10 mM H_2O_2 and UV light for 30 min. Under those conditions, hydroxyl radicals and other ROS should easily oxidize Nico. One aliquot of 0.5 mM Nico was mixed with 10 mM H_2O_2+UV for 30 min, and another was mixed with an equal volume of water. Figure 4.3 shows that the oxidation control drastically decreases Nico fluorescence, confirming that Nico oxidation would remove fluorescence signal. The spectrum of the H_2O_2+UV Nico solution also suffers some distortion, perhaps from further molecule decomposition. At this time, a Nico calibration curve has not been constructed, but normalized fluorescence intensities can be compared to assess relative amounts of Nico.

4.2.4 Determining dissolved ion concentrations.

We used inductively coupled plasma mass spectrometry (ICP-MS, Shimadzu 2030) to measure dissolved ion concentrations in samples after centrifugation/filtration. Samples were acidified in 2.5% HNO_3 before analysis. Additionally, a 500:1 dilution was required to reduce salt concentrations from the minimal medium. ^{7}Li, ^{59}Co, ^{60}Ni, and ^{55}Mn intensities were measured and referenced to internal standards of ^{9}Be (for Li) and ^{69}Ga (for remaining elements). Each sample was measured in triplicate by ICP-MS and the average intensities were used for quantification. Concentrations were determined using calibration curves. Standard solutions of all four elements combined were prepared by serial dilution from 1 $g \cdot L^{-1}$ certified reference materials. Standards were diluted and acidified in the same manner as the unknowns.

4.2.5 Determining Nico redox potential.

An important property of NADH-NAD$^+$ and Nico-Nico$^+$ is the presence of the redox-active nicotinamide moiety. However, given the two redox couples have different structures otherwise, they likely have different reducing/oxidizing strengths. The reduction potential of NADH has been well studied,[35] but to our knowledge that of 1-methyl-1,4-dihydronicotinamide has not. We performed cyclic voltammetry of 1 mM NADH or Nico in 1 M $NaClO_4$ in a three-electrode sealed glass cell with a 3 M Ag|AgCl reference electrode, glassy carbon working electrode, and platinum mesh counter electrode. The solution was purged with Ar and stirred, with the stirring stopped prior to measurement. Scans were taken from 0 V → +1.5 V → -1.0 V → 0 V vs. reference at a range of scan rates from 20 – 500 $mV \cdot s^{-1}$ (step size 0.005 mV). Electrochemical potentials for each couple at these conditions (pH 7 and 1 mM analyte) were calculated by taking the average of the oxidation and reduction peak potentials. Peak currents were not absolute maxima, as there was significant hydrogen/oxygen evolution background, and had to be estimated from “shoulder” peaks in the more discernable low scan rate voltammograms. Electrochemical experiments were performed on a Metrohm Autolab 302N Potentiostat-Galvanostat and data were analyzed using NOVA 1.6 software.

4.3 Results and discussion.

4.3.1 Nanoparticle characterization.

Powder x-ray diffraction patterns were taken of each material to assess purity and crystallinity and are shown in Figure 4.4. The synthesized compounds $LiCoO_2$ and $Co(OH)_2$ (Figure 3.2) match the expected literature patterns.[36, 37] Commercial CoO matches the expected pattern for CoO. However, interestingly the commercial “Ni_2O_3” and “MnO_2” were in fact NiO and Mn_2O_3, respectively, according to XRD analysis. Each pattern agrees well with reference patterns.[38, 39] Slight broadening of XRD peaks is expected given their nanoscale size.[40] Nitrogen adsorption isotherms were measured to calculate specific surface areas (S) of $S_{LiCoO2} = 114.0 \pm 0.8\ m^2 \cdot g^{-1}$, $S_{Co(OH)2} = 33.39 \pm 0.05\ m^2 \cdot g^{-1}$, $S_{Mn2O3} = 24.42 \pm 0.08\ m^2 \cdot g^{-1}$, and $S_{NiO} = 18.55 \pm 0.7\ m^2 \cdot g^{-1}$. If we assume a spherical shape for Mn_2O_3 and NiO and calculate an expected surface area ('S) given the material density and particle diameter specified by the manufacturer (50 nm for Mn_2O_3 and 80 nm for NiO), we find 'S_{Mn2O3} = 23.9 $m^2 \cdot g^{-1}$ and 'S_{NiO} = 15.5 $m^2 \cdot g^{-1}$. These values agree with the measured specific surfaces with ~20% error, indicating the particles are the expected sizes. While $Co(OH)_2$ and Mn_2O_3 have similar surface areas, the higher surface area of $LiCoO_2$ and lower surface area of NiO could impact our results, as most experiments are normalized by mass. However, this is a geometric factor that could be accounted for in control experiments. $LiCoO_2$ and $Co(OH)_2$ were further characterized in Chapter 3 (e.g., SEM), and similar tests will be performed for Mn_2O_3 and NiO.

4.3.2 Impacts of NADH, Nico, and Ribo on metal oxide dissolution.

Figure 4.5 shows the concentrations of solubilized metals after each nanoparticle type was exposed to solutions of minimal medium, media + NADH, media + Nico, media + Ribo, and media + Ribo + Nico. CoO and $Co(OH)_2$ are separated, as they have a larger scale of dissolution. Comparing the effects of each molecule on ion release for the different nanomaterials reveals several interesting results. First, we examine $LiCoO_2$ and $Co(OH)_2$. NADH increases Co release from $LiCoO_2$, but not $Co(OH)_2$. This confirms our results from Chapter 3, that the Co(III) in $LiCoO_2$ is required to interact with NADH. Next, and perhaps most surprising, is that Ribo, and not Nico, enhances Co release from $LiCoO_2$. This is unexpected since Nico is the primary redox-active component in NADH, which we hypothesized to be responsible for enhanced dissolution of $LiCoO_2$ in Chapter 3. Because the ribose phosphate molecule can influence metal release from these metal oxides in a similar way as NADH, the ribose moiety of NADH may be involved in its reactivity as well (see section 4.4). Additionally, we see from Figures 4.5A-B that the combined Nico + Ribo dissolution samples show approximately double the ion release than for NADH or Ribo alone. While still unclear, we hypothesize there could be a synergistic interaction of Nico and Ribo that not only reproduces the effects of their parent molecule, NADH, but surpasses them. It is unlikely this is an ionic strength effect (from each molecule being 0.5 mM) because this is a relatively small change in total ionic strength given the other solution components. We also rule out the possibilities of a systematic error because 1) the same batches of particles and the same ICP-MS standards were used for every experiment, 2) the

Nico + Ribo experiment was fully repeated with the same results, and 3) the increase in metal concentrations varies across the different compounds (i.e., they do not increase by the same factor).

Now we compare $LiCoO_2$ and $Co(OH)_2$ to the results of Mn_2O_3, NiO, and CoO. The Mn(III) compound Mn_2O_3 behaves similarly to $LiCoO_2$ in that it releases more ions upon exposure to NADH and Ribo and experiences no increase when exposed to Nico. The Ni(II) compound NiO, like $Co(OH)_2$, is relatively unaffected by any of the molecules. However, NiO does not show the large increase in ion release from the combined Nico + Ribo dissolution experiment, making it difficult to draw conclusions on its origin for the other compounds. Overall, these dissolution results for Mn_2O_3 and NiO are interesting in that 1) they confirm our hypothesis that NADH acts as a reducing agent to enhance ion release specifically for high oxidation state metal oxides, and 2) they suggest that our results from Chapter 3 extend to compounds beyond $LiCoO_2$. The Co(II) containing compound CoO is meant to be a similar control as to $Co(OH)_2$. The concentrations of released Co for CoO are consistent across each media type, like $Co(OH)_2$, which is expected if the Co oxidation state is not changing upon dissolution. Yet, Co release from CoO is much higher, potentially plateauing at a solubility limit (beyond that in pure water due to increased ionic strength and chelating agents).[41] Further studies under different conditions (e.g., lower particle loading or shorter time) would need to be performed to learn more about the effect these molecules on CoO dissolution.

4.3.3 Difference in NADH and Nico fluorescence response.

With Nico and its parent molecule NADH having differing effects on the nanomaterials under study, we sought to uncover the extent to which each of these nicotinamides were oxidized by measuring their fluorescence before and after dissolution experiments. Dissolution experiments with NADH show drastically different final concentrations depending on the nanoparticle (Figure 4.6). The +3 oxidation state compounds $LiCoO_2$ and Mn_2O_3 yield severe decreases in NADH concentration. We ascribe this to oxidation of NADH to the non-fluorescent NAD^+, coupled with enhanced metal ion release. The +2 oxidation state compounds $Co(OH)_2$ and NiO yield slight decreases in NADH concentration, likely due to adsorption of NADH on the surface of the particles (which are removed prior to fluorescence analysis). This suggests that NADH is not being oxidized by the materials and NADH is not reducing the metals, which is consistent with their constant ion release regardless of the presence of NADH. These data confirm our results in Chapter 3 and section 4.3.2 that high oxidation state metal oxides alone oxidize NADH, and in the process their ion release is enhanced.

On the other hand, dissolution experiments with Nico or Nico + Ribo show a uniform concentration of Nico remaining after 24 h with any of the particles tested (Figure 4.7). These data show that the metal oxide nanoparticles have no impact on the redox state of Nico, which is consistent with our observation that Nico had no impact on metal ion release (Figure 4.5). This is further evidence pointing toward Ribo as an active component of NADH. Our results suggest that either A) Nico is too weak a reducing agent to transform the nanomaterials, B) direct surface binding with a group such as phosphate, which Nico does not have, is required to react, or C) the ribose sugar and not the nicotinamide is the part of NADH that undergoes the coupled redox transformation with metal oxides (see section 4.3.5). It is possible it is a surface-driven electron-transfer (statement B), as Chapter 3 showed binding of NADH to $LiCoO_2$ via XPS. However, further XPS binding experiments with Nico and Ribo, and the additional nanomaterials (Mn_2O_3 and NiO) are needed to elucidate such a mechanism. Statement A is address below in section 4.3.4.

4.3.4 Redox potentials of Nico and NADH.

To study the electrochemical properties of NADH and Nico, we used cyclic voltammetry in a 3-electrode cell. Solutions were prepared of 1 mM NADH and 1-methyl-1,4-dihydronicotinamide (Nico, the reduced forms of each) in 1 M $NaClO_4$ as an inert electrolyte. An example voltammogram is shown in Figure 4.8. On the positive sweep, positive current peaks are produced for oxidation of both NADH and Nico. On the negative sweep, each molecule displays a small negative current peak corresponding to reduction of NAD+ or oxidized Nico. At extreme potentials in both directions, background current increases from water electrolysis. Since $|I_{Ox}| >> |I_{Red}|$ and the gap between E_{Ox} and E_{Red} is large for NADH (~1.28 V) and Nico (~0.74 V), both redox equilibria are highly irreversible. Reduction potentials for each species under these conditions (1 mM analyte, pH 7, room temperature) were calculated by taking the average of peak potentials to yield E_{NADH} = +0.26$_5$ V vs. SHE and E_{Nico} = +0.10$_7$ V vs. SHE. Our calculated value for E_{NADH} deviates significantly from the literature value of E^0_{NADH} at pH 7 of -0.315 V vs. SHE, with the difference likely being attributed to A) a difference in concentrations (1 mM in this work vs. 1 M in Wilson et al.),[35] and B) error in our measurement arising from the irreversibility of the reactions. However, given that the apparatus and parameters are the same for both NADH and Nico, any errors from concentration differences, electrode overpotential, ohmic potentials, etc. should be the same such that the relative values can be compared accurately.

Comparing the reduction potentials for NADH and Nico, we see that $E_{NADH} > E_{Nico}$ (it is more positive). This means that formation of the reduced form of Nico is less favored than the formation of NADH. When looking from the perspective of oxidation (i.e., acting as a reducing agent), it is easier to oxidize Nico than NADH. This can be seen qualitatively in Figure 4.8 from the order of the oxidation peaks on the positive sweep: it requires more energy to initiate NADH oxidation. Because of this, Nico is considered a stronger reducing agent than NADH. If the weaker reducing agent, NADH, can transform nanomaterials when the stronger reducing agent, Nico, has no effect on the nanomaterials, there must be another explanation for the interaction beyond the nicotinamide reducing strength.

4.3.5 Ribose as a possible reducing agent.

Figures 4.5 and 4.7 suggest that Ribo, and not Nico, is responsible for the reciprocal redox interaction observed of NADH with $LiCoO_2$ and other materials. While, unexpected, it is possible that the ribose itself acts as a reducing agent towards the high valence metal oxides in our experiments. If this is the case, ribose in NADH may even be involved in its reaction with nanoparticles. Any monosaccharide that can tautomerize into an aldehyde straight-chain structure can be oxidized, and thus act as a weak reducing agent. This includes D-ribose-5-phosphate (Figure 4.1B) and would explain why Ribo is able to preferentially enhance metal ion release from high valence oxides $LiCoO_2$ and Mn_2O_3. But what about ribose in NADH? Unlike in Ribo, the ribose sugar of NADH is part of a rigid structure, bound to the nicotinamide on one side and the diphosphate bridge on the other. Since the carbon at position 1 in Figure

4.1A is bonded to N, unfolding the ribose ring yields an amide, not an aldehyde. While studies have shown that tautomerization of select amino acids can occur,[42, 43] this is not possible for NADH because it does not have the necessary -COOH group and the other side of the ribose ring is connected to a bulky -R group. Therefore, ribose in NADH cannot act as the primary reducing agent in a traditional manner. However, since Nico shows no reactivity towards even high valence metal oxides, and since our experiments suggest that NADH attaches to the surface, there could be a connection between ribose sugar and nicotinamide in NADH. We hypothesize that if NADH binds to $LiCoO_2$, etc. via its phosphate groups (which are local to ribose), then there may be an electron transfer event from the nicotinamide to the metal atoms, or from the nicotinamide to the ribose and then to the metal atoms. This is because Nico alone cannot initiate the reaction, whereas Ribo can, and because ribose in NADH cannot act as the primary reducing agent. A model of the proposed mechanism is shown in Figure 4.9. In this model the binding site for NADH is on a metal-terminated surface, given the negative charge of phosphate. Electrons are transferred from the nicotinamide to the ribose, and finally to Co(III) which is reduced to aqueous Co(II). NADH is oxidized and detaches from the surface.

4.4 Conclusions and future directions.

From this investigation we draw several interesting conclusions on the interaction of NADH and its components with metal oxide nanomaterials. First, it is Ribo, not Nico, that can reproduce the reciprocal redox dissolution of metal oxides like its parent molecule, despite nicotinamide being the expected redox-active component of NADH. This is because Ribo (not Nico) enhances metal ion release for high valence oxides, and none of the nanomaterials tested affected Nico redox state. Moreover, from electrochemical measurements we find Nico to be a stronger reducing agent than NADH. This means a simple lack of reducing strength cannot be the reason for absence of reactivity with Nico. We attribute this to the moderate reducing strength of ribose phosphate via tautomerization to its straight-chain aldehyde form and the lack of a binding moiety in Nico. While we can measure the redox state of Nico via fluorescence, we have not performed such experiments with Ribo. If Ribo is acting as a reducing agent, then it is critical in the future to measure the loss of the reduced form and/or increase in concentration of the oxidized product. This could be done by fluorescence/absorbance spectroscopies (though this may lack structural specificity),[44, 45] classic reduced sugar tests (e.g., Benedict's Reagent or Tollen's Reagent), ^{13}C NMR (to avoid H_2O interference in ^{1}H NMR), or HPLC-MS. The lack of activity for Nico suggests that a binding moiety, such as phosphate, is necessary to react with $LiCoO_2$, etc. As mentioned in Chapter 3, Laudadio et al. have shown that phosphates bind strongly to $LiCoO_2$, and that exposure to phosphate did not increase $LiCoO_2$ dissolution (ruling out a complexation effect).[15, 16] By performing nanoparticle dissolution experiments with exposure to ribose instead of ribose phosphate (Ribo), this could show if the phosphate group is required to enhance ion release. If ribose (no phosphate) does not increase ion release from high valence oxides, then this suggests phosphate is required for a surface-driven reaction. This would also explain why Nico is unreactive. If ribose increases ion release from the high valence oxides just like NADH or ribose phosphate, then phosphate binding is not required for the reducing sugars to react with the particles. We have seen NADH binding to nanoparticles via XPS in Chapter 3, however additional XPS binding experiments for Nico and Ribo could prove useful. We would expect to see strong attachment of Ribo (measured via P(2p) signal), and minimal attachment of Nico (measured via N(1s) signal). Regarding characterization of Nico, our fluorescence measurements are promising, but further analysis of the Nico fluorescence spectrum and a calibration curve would be helpful since this molecule is not as well studied as is NADH.

Second, we compared the interaction of NADH etc. with Co compounds $LiCoO_2$ and $Co(OH)_2$ to their interaction with other oxides, namely Mn_2O_3 and NiO. We see in both metal ion release and effect on NADH redox state, these materials behave similarly to $LiCoO_2$ or $Co(OH)_2$ according to metal oxidation state. For example, Mn_2O_3 significantly oxidizes NADH (like $LiCoO_2$), whereas NiO decreases NADH concentration minimally through NADH adsorption to the particle surface (like $Co(OH)_2$). This shows that our conclusions about the reciprocal redox interaction of reducing biomolecules and high valance oxides extends to compounds beyond the Co-containing $LiCoO_2$ and $Co(OH)_2$. Unfortunately, our results with CoO were inconclusive due to experimental errors and the released Co concentrations being too high under our experimental conditions. CoO is an important control because CoO has shown toxicity through oxidative stress[46] and is predicted to have such effects through band structure analysis,[10] despite Co being in the +2 state (like Ni in NiO). Therefore, future experiments must include CoO to discern whether metal oxidation state, band structure, concentration of ions released, or some other factor dictates interaction of the nanomaterial with NADH and other molecules. Additionally, we have yet to perform important characterization of Mn_2O_3, NiO, and CoO particles to identify their size, shape, and surface charge, as these properties could impact reactivity with NADH and its component molecules.

This study both confirms our results of Chapter 3 by reproducing with addition nanomaterials and shows that simple sugars (e.g., Ribo) cannot be ignored in when assessing the mutual interactions of media and nanomaterials. The ribose within NADH may be contributing towards its reactivity, and perhaps more importantly, other reducing sugars present in media could undergo the same reciprocal redox transformation. For example, a major component of the media used in our experiments is dextrose (i.e., glucose). This monosaccharide can act as a weak reducing agent just like ribose and is in the media at an even higher concentration (10 mM) than Ribo or Nico (0.5 mM). Glucose and/or other media components could be either enhancing nanoparticle dissolution by similar mechanisms as NADH and Ribo or restricting dissolution by coating the nanoparticle surface. That is, the presence of glucose or other molecules could either be adding a consistent background of metal ion release to our experiments, or consistently diminishing what would be even greater impact from NADH, etc. on the particles. The media in Table 3.3 was chosen to mimic bacterial growth media, however this may be overly complex for a study aimed to understand the effects of specific molecules on nanoparticle transformation. Therefore, we should simplify the solutions nanoparticles are exposed to and probe the effects of media components (salts, buffers, carbon sources) on metal release.

The mechanism proposed herein for NADH reacting with the metal oxide surface fits with the presented data but is incomplete due to lack of knowledge on the necessity of the phosphate binding group for reactivity and the mechanism of Ribo degradation or identification of its degradation products. This information can be achieved through the experiments described above. Additionally, we have found that reducing sugars, such as ribose or glucose, must be considered when studying how media components transform metal oxide nanomaterials. While the focus of Chapters 3 and 4 has been on metal ion release, this must be coupled with release of oxygen from the metal oxide lattice. This mechanism has been investigated computationally[47,48] but experimental evidence is lacking. We performed experiments seeking to detect if oxygen gas was generated from the dissolution of $LiCoO_2$ and other particles by measuring pressure changes in a sealed container, though results were inconclusive (data not shown). Studying oxygen release, metal release, and transformations to media components, will lead to better understanding the interaction of NADH and other small redox-active biomolecules with high valance metal oxides.

4.5 Figures.

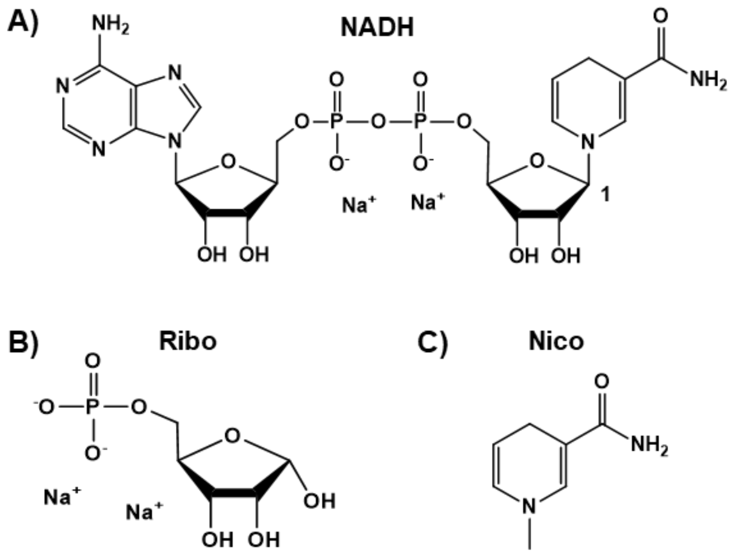

Figure 4.1. Molecular structures of A) NADH, B) D-ribose-5-phosphate (Ribo), and C) 1-methyl-1,4-dihydronicotinamide (Nico).

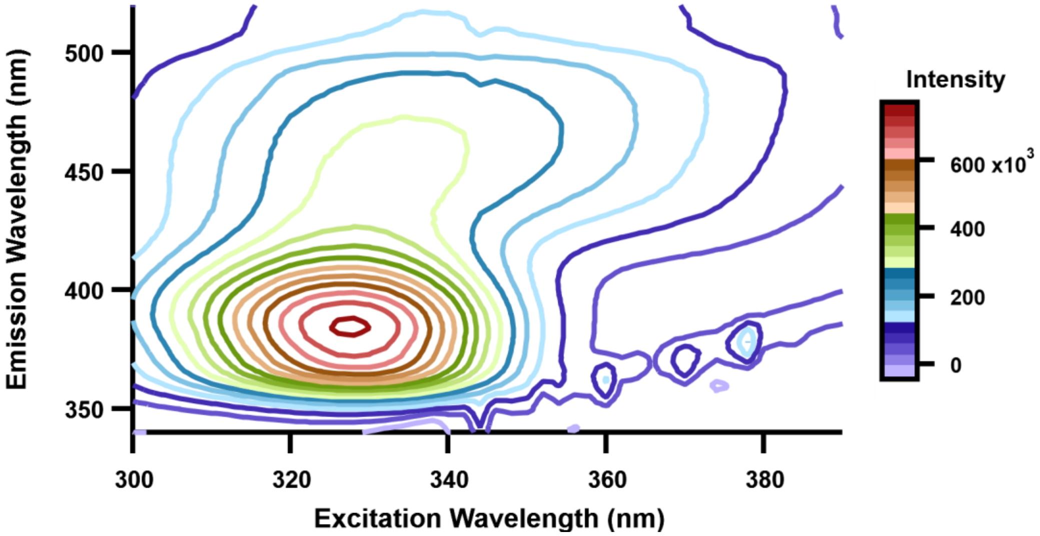

Figure 4.2. Excitation-emission matrix of 0.5 mM 1-methyl-1,4-dihydronicotinamide (Nico) minimal media with dextrose in a 1 cm^2 fused silica cuvette with step size of 2 nm and integration time of 1 s at each point. The background at Y = X (lower right) corresponds to scattering of the excitation light.

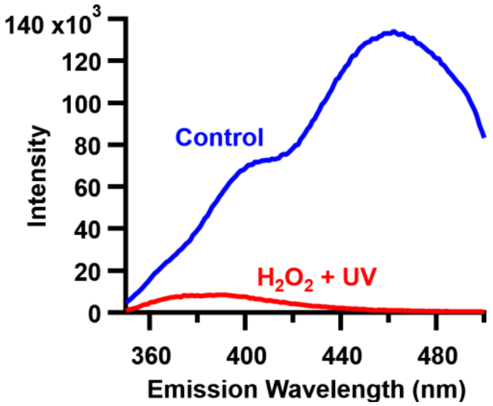

Figure 4.3. Fluorescence spectra of 0.5 mM Nico solution diluted 2:1 in water (blue, control), or 10 mM H_2O_2 with 30 min of UV exposure (red, intentional oxidation).

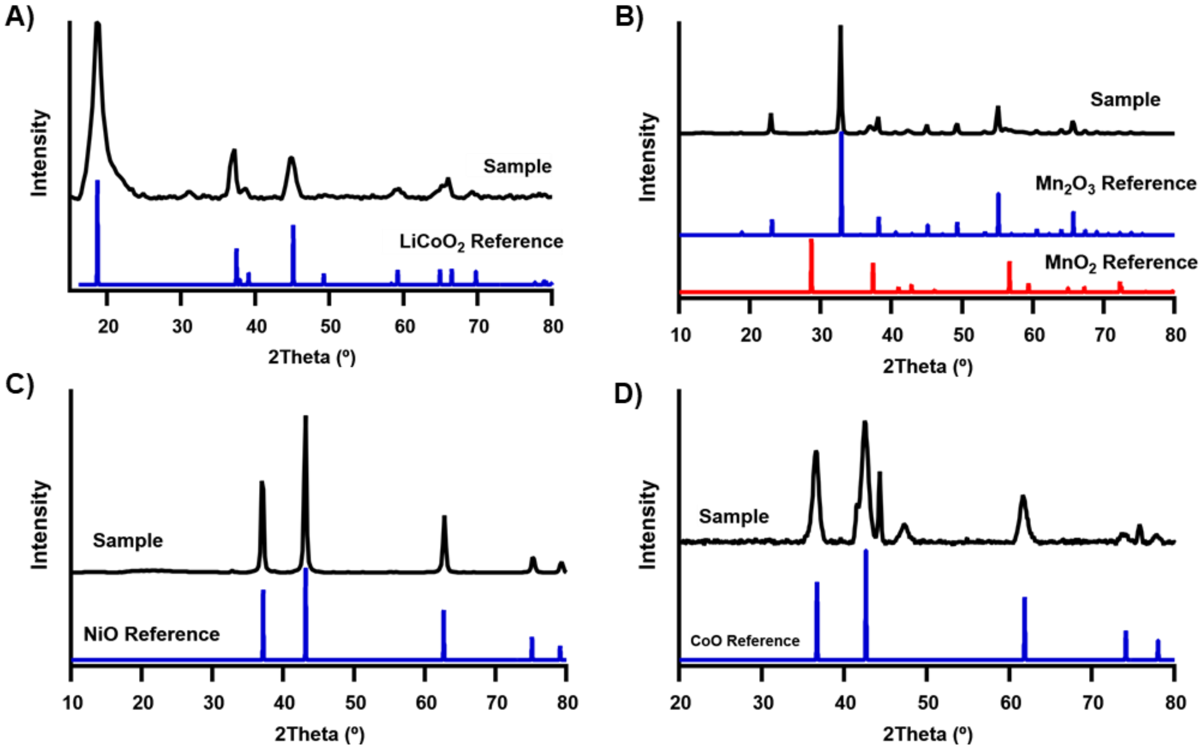

Figure 4.4. Powder x-ray diffraction patterns for A) $LiCoO_2$, B) Mn_2O_3, C) NiO, and D) CoO particles. Reference patterns were taken from the Crystallography Open Database (see text for references). Despite the supplier labeling compounds as Ni_2O_3 and MnO_2, they match reference patterns of NiO and Mn_2O_3, respectively. See Figure 3.2 for $Co(OH)_2$.

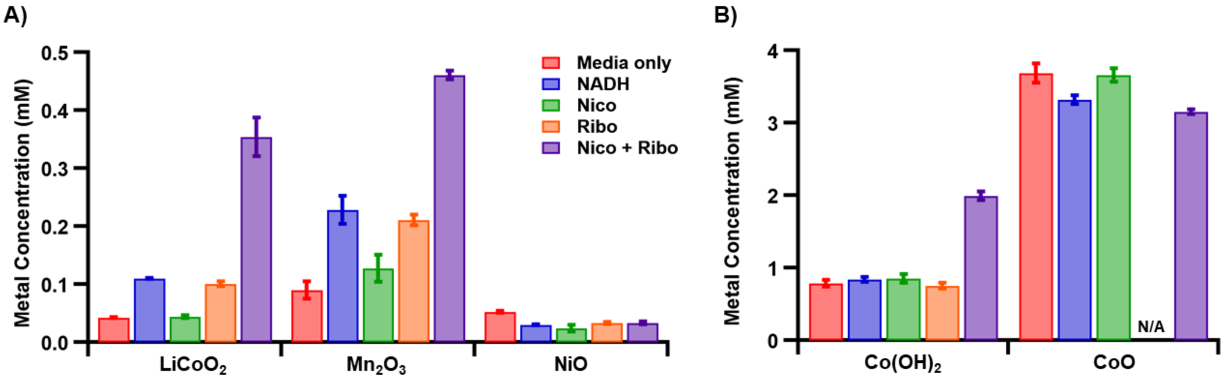

Figure 4.5. Respective transition metal (e.g., Co for $LiCoO_2$ and Mn for Mn_2O_3) concentrations determined by ICP-MS for A) $LiCoO_2$, Mn_2O_3, and NiO, and B) $Co(OH)_2$ and CoO, after 24-h, 1 mg·mL^{-1} exposure to minimal medium with dextrose and the listed molecules. Note the difference in axis scale. Data for CoO with Ribo not available due to experimental error.

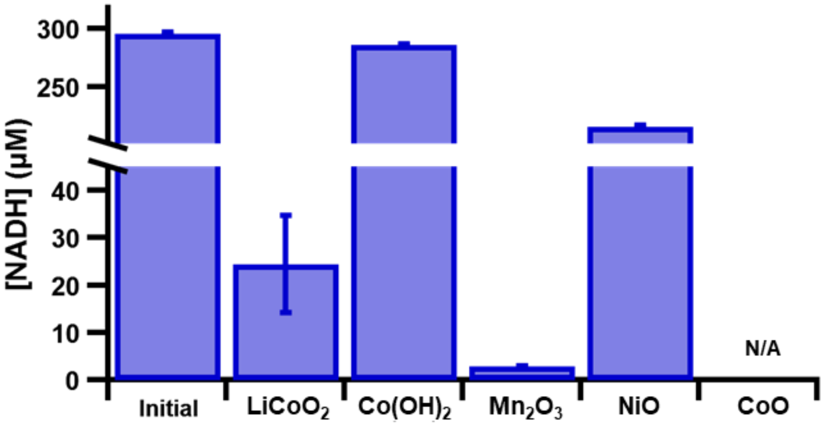

Figure 4.6. Concentrations of NADH determined via fluorescence and a calibration curve after a 24-h dissolution experiment with the listed particles at 1 mg·mL^{-1}. “Initial” indicates the starting NADH solution. Data for CoO not available due to experimental error.

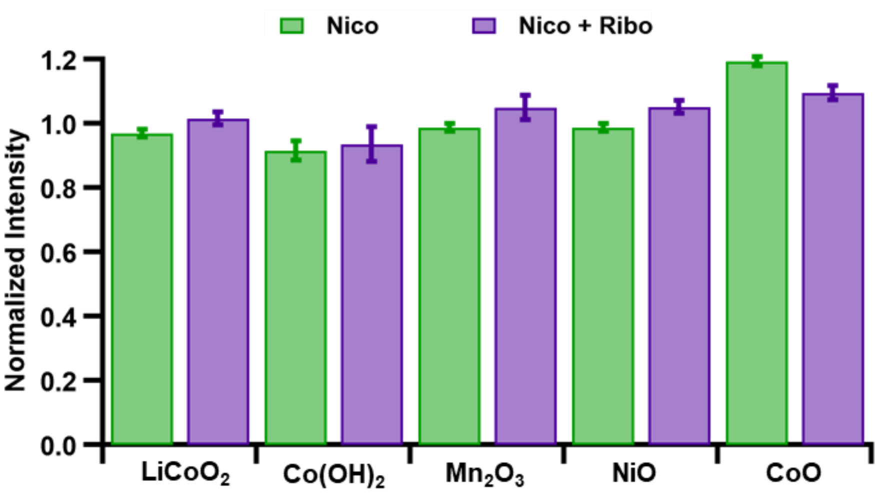

Figure 4.7. Normalized fluorescence intensity for 0.5 mM Nico (green) or 0.5 mM Nico with 0.5 mM Ribo (purple) solutions after a 24-h dissolution experiment with the listed particles at 1 mg·mL-1. Intensities were measured at 382 nm and normalized so that the initial Nico solution has I = 1.00. Because all values are close to unity, none of the Nico solutions had a significant change in fluorescence over the 24 h.

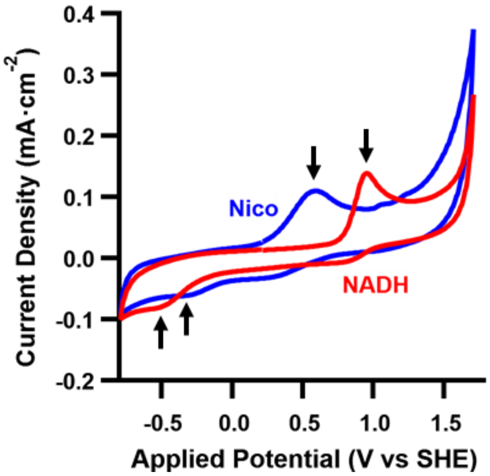

Figure 4.8. Representative cyclic voltammogram for 1 mM NADH (red) and Nico (blue) in 1 M $NaClO_4$ solution. Working electrode was swept 100 mV·s^{-1} from 0 V → +1.5 V → -1.0 V → 0 V vs. 3 M Ag|AgCl. Current density was calculated using the geometric area of the circular working electrode (0.182 cm^2). Arrows indicate the approximate locations of peak potentials.

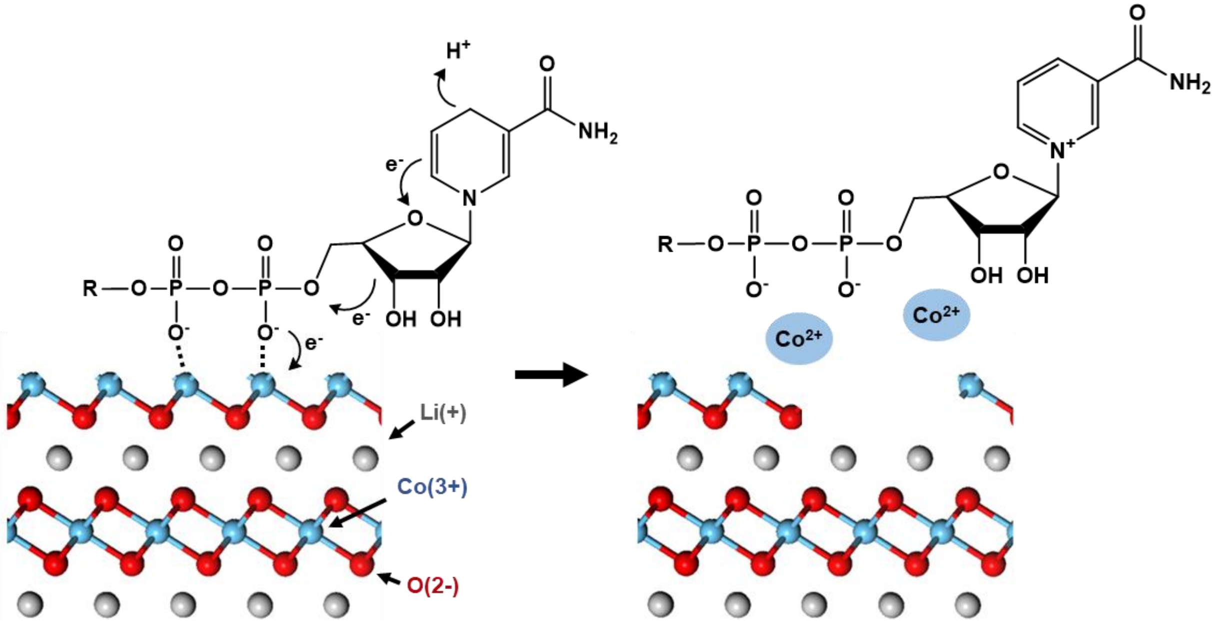

Figure 4.9. Proposed mechanism for the redox reaction of NADH with $LiCoO_2$. NADH binds to $LiCoO_2$ via its phosphate groups, after which Co(III) is reduced by the transfer of electrons from nicotinamide to ribose, to Co(III). The products are solubilized Co(II) and NAD^+. The reaction is not fully balanced to account for release of oxygen atoms from the lattice, which are likely to react with H^+ to form H_2O.

4.6 References.

1. Paustenbach, D. J.; Tvermoes, B. E.; Unice, K. M.; Finley, B. L.; Kerger, B. D., A Review of the Health Hazards Posed by Cobalt. *Crit. Rev. Toxicol.* **2013**, *43*, 316–362.

2. Collins, R. N.; Kinsela, A. S., The Aqueous Phase Speciation and Chemistry of Cobalt in Terrestrial Environments. *Chemosphere* **2010**, *79*, 763–771.

3. Xia, T.; Kovochich, M.; Liong, M.; Mädler, L.; Gilbert, B.; Shi, H.; Yeh, J. I.; Zink, J. I.; Nel, A. E., Comparison of the Mechanism of Toxicity of Zinc Oxide and Cerium Oxide Nanoparticles Based on Dissolution and Oxidative Stress Properties. *ACS Nano* **2008**, *2*, 2121–2134.

4. Papis, E.; Rossi, F.; Raspanti, M.; Dalle-Donne, I.; Colombo, G.; Milzani, A.; Bernardini, G.; Gornati, R., Engineered Cobalt Oxide Nanoparticles Readily Enter Cells. *Toxicol. Lett.* **2009**, *189*, 253–259.

5. Behl, B.; Papageorgiou, I.; Brown, C.; Hall, R.; Tipper, J. L.; Fisher, J.; Ingham, E. Biological Effects of Cobalt-Chromium Nanoparticles and Ions on Dural Fibroblasts and Dural Epithelial Cells. *Biomaterials* **2013**, *34*, 3547–3558.

6. Melby, E. S.; Cui, Y.; Borgatta, J.; Mensch, A. C.; Hang, M. N.; Chrisler, W. B.; Dohnalkova, A.; Van Gilder, J. M.; Alvarez, C. M.; Smith, J. N.; Hamers, R. J.; Orr, G., Impact of Lithiated Cobalt Oxide and Phosphate Nanoparticles on Rainbow Trout Gill Epithelial Cells. *Nanotoxicology* **2018**, *12*, 1166–1181.

7. Buchman, J. T.; Bennett, E. A.; Wang, C.; Tamijani, A.; Bennett, J. W.; Hudson, B. G.; Green, C. M.; Clement, P. L.; Zhi, B.; Henke, A. H.; Laudadio, E. D.; Mason, S. E.; Hamers, R. J.; Klaper, R. D.; Haynes, C. L., Nickel Enrichment of Next-Generation NMC Nanomaterials Alters Material Stability, Causing Unexpected Dissolution Behavior and Observed Toxicity to S. Oneidensis MR-1 and D. Magna. *Environ. Sci. Nano* **2020**, *7*, 571–587.

8. Sironval, V.; Scagliarini, V.; Murugadoss, S.; Tomatis, M.; Yakoub, Y.; Turci, F.; Hoet, P.; Lison, D.; Van Den Brule, S., $LiCoO_2$ Particles Used in Li-Ion Batteries Induce Primary Mutagenicity in Lung Cells via Their Capacity to Generate Hydroxyl Radicals. *Part. Fibre Toxicol.* **2020**, *17*, 1–9.

9. Li, Y.; Zhang, W.; Niu, J.; Chen, Y., Mechanism of Photogenerated Reactive Oxygen Species and Correlation with the Antibacterial Properties of Engineered Metal-Oxide Nanoparticles. *ACS Nano* **2012**, *6*, 5164–5173.

10. Zhang, H.; Ji, Z.; Xia, T.; Meng, H.; Low-kam, C.; Liu, R.; Pokhrel, S., Use of Metal Oxide Nanoparticle Band Gap to Develop a Predictive Paradigm for Oxidative Stress and Acute Pulmonary Inflammation. **2012**, *6*, 4349–4368.

11. Rezaei-Zarchi, S.; Imani, S.; Zand, A.; Saadati, M.; Zaghari, Z., Study of Bactericidal Properties of Carbohydrate-Stabilized Platinum Oxide Nanoparticles. *Int. Nano Lett.* **2012**, *2*, 21.

12. Lartigue, L.; Innocenti, C.; Kalaivani, T.; Awwad, A.; Sanchez Duque, M. D. M.; Guari, Y.; Larionova, J.; Guéirin, C.; Montero, J. L. G.; Barragan-Montero, V.; Arosio, P.; Lascialfari, A.; Gatteshci, D.; Sangregorio, C., Water-Dispersible Sugar-Coated Iron Oxide Nanoparticles. An Evaluation of Their Relaxometric and Magnetic Hyperthermia Properties. *J. Am. Chem. Soc.* **2011**, *133*, 10459–10472.

13. Dhanalakshmi, A.; Palanimurugan, A.; Natarajan, B., Efficacy of Saccharides Bio-Template on Structural, Morphological, Optical and Antibacterial Property of ZnO Nanoparticles. *Mater. Sci. Eng. C* **2018**, *90*, 95–103.

14. Iconaru, S. L.; Prodan, A. M.; Motelica-Heino, M.; Sizaret, S.; Predoi, D., Synthesis and Characterization of Polysaccharide-Maghemite Composite Nanoparticles and Their Antibacterial Properties. *Nanoscale Res. Lett.* **2012**, *7*, 576.

15. Laudadio, E. D.; Bennett, J. W.; Green, C. M.; Mason, S. E.; Hamers, R. J., Impact of Phosphate Adsorption on Complex Cobalt Oxide Nanoparticle Dispersibility in Aqueous Media. *Environ. Sci. Tech.* **2018**, *52*, 10186–10195.

16. Laudadio, E. D.; Ilani-kashkouli, P.; Green, C. M.; Kabengi, N. J.; Hamers, R. J., Interaction of Phosphate with Lithium Cobalt Oxide Nanoparticles: A Combined Spectroscopic and Calorimetric Study. *Langmuir* **2019**, *35*, 16640–16649.

17. Drever, J. I.; Stillings, L. L., The Role of Organic Acids in Mineral Weathering. *Colloids Surfaces A Physicochem. Eng. Asp.* **1997**, *120*, 167–181.

18. Huang, W. H.; Keller, W. D., Dissolution of Rock-Forming Silicate Minerals in Organic Acids: Simulated First-Stage Weathering of Fresh Mineral Surfaces. *Am. Mineral.* **1970**, *55*, 2076–2094.

19. Houben, G. J., Iron Oxide Incrustations in Wells. Part 2: Chemical Dissolution and Modeling. *Appl. Geochem.* **2003**, *18*, 941–954.

20. Flynn, E. D.; Catalano, J. G., Reductive Transformations of Layered Manganese Oxides by Small Organic Acids and the Fate of Trace Metals. *Geochimica et Cosmochimica Acta* **2019**, *250*, 149–172.

21. Dong, H., Mineral-Microbe Interactions: A Review. *Front. Earth Sci. China* **2010**, *4*, 127–147.

22. Kostka, J. E.; Nealson, K. H. Dissolution and Reduction of Magnetite by Bacteria. *Environ. Sci. Tech.* **1995**, *29*, 2535–2540.

23. Smith, S. L.; Grail, B. M.; Johnson, D. B., Reductive Bioprocessing of Cobalt-Bearing Limonitic Laterites. *Miner. Eng.* **2017**, *106*, 86–90.

24. Ouyang, B.; Akob, D. M.; Dunlap, D.; Renock, D., Microbially Mediated Barite Dissolution in Anoxic Brines. *Appl. Geochem.* **2017**, *76*, 51–59.

25. Revesz, E.; Fortin, D.; Paktunc, D., Reductive Dissolution of Scorodite in the Presence of Shewanella Sp. CN32 and Shewanella Sp. ANA-3. *Appl. Geochem.* **2015**, *63*, 347–356.

26. Gorby, Y. A.; Caccavo, F.; Bolton, H., Microbial Reduction of Cobalt(III)EDTA- in the Presence and Absence of Manganese(IV) Oxide. *Environ. Sci. Tech.* **1998**, *32*, 244–250.

27. Shi, L.; Dong, H.; Reguera, G.; Beyenal, H.; Lu, A.; Liu, J.; Yu, H. Q.; Fredrickson, J. K., Extracellular Electron Transfer Mechanisms between Microorganisms and Minerals. *Nat. Rev. Microbiol.* **2016**, *14*, 651–662.

28. Pourbaix, M., trans. Franklin, J. A., Atlas of Electrochemical Equilibria in Aqueous Solutions. *J. Electroanal. Chem. Interfacial Electrochem.* **1967**, *13*, 471.

29. Brunauer, S.; Emmett, P. H.; Teller, E., Adsorption of Gases in Multimolecular Layers. *J. Am. Chem. Soc.* **1938**, *60*, 309–319.

30. Xiao, W.; Wang, R. S.; Handy, D. E.; Loscalzo, J., NAD(H) and NADP(H) Redox Couples and Cellular Energy Metabolism. *Antiox. Redox Signaling* **2018**, *28*, 251–272.

31. Reiss, P. D.; Zuurendonk, P. F.; Veech, R. L., Measurement of Tissue Purine, Pyrimidine, and Other Nucleotides by Radial Compression High-Performance Liquid Chromatography. *Anal. Biochem.* **1984**, *140*, 162–171.

32. Yamada, K.; Hara, N.; Shibata, T.; Osago, H.; Tsuchiya, M., The Simultaneous Measurement of Nicotinamide Adenine Dinucleotide and Related Compounds by Liquid Chromatography / Electrospray Ionization Tandem Mass Spectrometry. *Anal. Biochem.* **2006**, *352*, 282–285.

33. Chance, B.; Schoener, B.; Oshino, R.; Itshak, F.; Nakase, Y., Oxidation-Reduction Ratio Studies of Mitochondria in Freeze-Trapped Samples. *J. Biol. Chem.* **1979**, *254*, 4764–4771.

34. Rehman, A. U.; Anwer, A. G.; Gosnell, M. E.; Mahbub, S. B.; Liu, G.; Goldys, E. M., Fluorescence Quenching of Free and Bound NADH in HeLa Cells Determined by Hyperspectral Imaging and Unmixing of Cell Autofluorescence. *Biomed. Opt. Express* **2017**, *8*, 1488–1498.

35. Wilson, D. F.; Erecinska, M.; Dutton, P. L., Thermodynamic Relationships in Mitochondrial Oxidative Phosphorylation. *Annu. Rev. Biophys. Bioeng.* **1974**, *3*, 203–230.

36. Takahashi, Y.; Kijima, N.; Dokko, K.; Nishizawa, M.; Uchida, I.; Akimoto, J., Structure and Electron Density Analysis of Electrochemically and Chemically Delithiated $LiCoO_2$ Single Crystals. *J. Solid State Chem.* **2007**, *180*, 313–321.

37. Lotmar, W.; Feitknecht, W., Uber Anderungen Der Ionenabstande in Hydroxd-Schichtengittern. *Zeitschrift fuer Kristallographie, Kristallgeometrie, Kristallphysik, Kristallchemie*; 1936; pp 368–378.

38. Hase, W., Neutronographische Bestimmung Der Kristallstrukturparameter von Dy_2O_3, Tm_2O_3 Und α -Mn_2O_3. *Phys. Status Solidi* **1963**, K446–K449.

39. Milligan, W. O.; Watt, L. M., X-Ray Diffraction Studies in the System NiO-Cr_2O_3-ZrO_2. *J. Am. Chem. Soc.* **1947**, 230–235.

40. Lamas, D. G.; Neto, M. D. O.; Kellermann, G.; Craievich, A. F., Nanocharacterization Techniques. Elsevier Inc., **2017**, 111-182.

41. Dinov, K.; Matsuura, C.; Hiroishi, D.; Ishigure, K., Solubility of Nickel and Cobalt Oxides in High-Temperature Water. *Nucl. Sci. Eng.* **1993**, *113*, 207–216.

42. Takahashi, O.; Kirikoshi, R., Intramolecular Cyclization of Aspartic Acid Residues Assisted by Three Water Molecules: A Density Functional Theory Study. *Comput. Sci. Discov.* **2014**, *7*.

43. Robinson, A. B.; McKerrow, J. H.; Cary, P., Racemization of Aspartic Acid in Human Proteins. *Proc. Natl. Acad. Sci.* **1970**, 66, 753-757.

44. Garrett, E. R.; Blanch, J.; Seydel, J. K., Spectrophotometric Analyses of Ribose and 2-Deoxy-D-Ribose Alone and in Mixtures. *J. Pharm. Sci.* **1967**, *56*, 1560–1564.

45. Baunsgaard, D.; Nørgaard, L.; Godshall, M. A., Fluorescence of Raw Cane Sugars Evaluated by Chemometrics. *J. Agric. Food Chem.* **2000**, *48*, 4955–4962.

46. Chattopadhyay, S.; Dash, S. K.; Tripathy, S.; Das, B.; Mandal, D.; Pramanik, P.; Roy, S., Toxicity of Cobalt Oxide Nanoparticles to Normal Cells; An in Vitro and in Vivo Study. *Chem. Biol. Interact.* **2015**, *226*, 58–71.

47. Bennett, J. W.; Jones, D.; Huang, X.; Hamers, R. J.; Mason, S. E., Dissolution of Complex Metal Oxides from First-Principles and Thermodynamics: Cation Removal from the (001) Surface of $Li(Ni_{1/3}Mn_{1/3}Co_{1/3})O_2$. *Environ. Sci. Tech.* **2018**, *52*, 5792–5802.

48. Abbaspour-Tamijani, A.; Bennett, J. W.; Jones, D. T.; Cartagena-Gonzalez, N.; Jones, Z. R.; Laudadio, E. D.; Hamers, R. J.; Santana, J. A.; Mason, S. E., DFT and Thermodynamics Calculations of Surface Cation Release in $LiCoO_2$. *Appl. Surf. Sci.* **2020**, *515*, 145865.

Appendices

Appendix 1. Spatial separation and detection of abiotic H_2O_2 from $LiCoO_2$.

The following is adapted from excerpts of the article in *Environmental Science: Nano* 2021, (recently accepted) with the co-authors Metti K. Gari, Paul Lemke, Kelly H. Lu, Elizabeth D. Laudadio, Curtis M. Green, Thomas Pho, Khoi Nguyen L. Hoang, Catherine J. Murphy, Robert J. Hamers, and Z. Vivian Feng. The bulk of the manuscript was completed by Metti K. Gari under the supervision of Z. Vivian Feng. Austin H. Henke contributed to data collection, data analysis, and manuscript preparation for the sections discussed below, under supervision of Robert J. Hamers and with assistance from Curtis M. Green.

This work was supported by the National Science Foundation (NSF) under the Center for Sustainable Nanotechnology, CHE-2001611. The Center for Sustainable Nanotechnology is part of the NSF Centers for Chemical Innovation Program.

A.1.1 Introduction.

Metal oxide nanoparticles can lead to cytotoxicity through dissolution of metal ions, largely due to their high surface-to-volume ratios. For instance, lithium nickel manganese cobalt oxide has been shown to release toxic levels of nickel, manganese, and cobalt ions that impact bacterial respiration[1, 2] and lifecycle of Daphnia magna.[3] Yet, often, the dissolved ions cannot fully recapitulate the biological impacts. In eukaryotic cells where nanoparticles may be internalized, cytotoxicity has been linked to nanoparticle-induced intracellular reactive oxygen species (ROS) generation and cellular oxidative stress.[4] Metal oxide nanoparticles can induce ROS due to their reactive surfaces, semiconductor electronic properties, or through the release of redox active transition metal ions triggering biomolecule redox reactions.[5] Species such as superoxide, hydroxyl radical, and hydrogen peroxide, once formed intracellularly at levels that overwhelm the antioxidant systems, often result in oxidative stress exhibited by DNA damage or lipid peroxidation.[5-7] Therefore, it is essential to understand abiotic ROS formation from these materials and the cellular response. Lithium cobalt oxide ($LiCoO_2$), an example of nanoscale transition metal oxides, is one of the most widely commercialized cathode materials in lithium ion batteries. Although studies have suggested $LiCoO_2$ can induce oxidative stress and impact growth cycles of model organisms, the detailed toxicity mechanism is still unclear. To better understand how oxidative stress responses are triggered in model bacterium, *B. subtilis*, upon exposure to $LiCoO_2$, we monitored how $LiCoO_2$ released Co ions and generated abiotic reactive oxygen species (ROS) in aqueous medium over time.

Spectroscopic assays were performed using fluorescent probes to react with and indirectly detect H_2O_2, $^1O_2$, $\cdot O_2^-$, and $\cdot OH$. Although the use of fluorescent probes is a common and effective approach to detecting ROS,[8] one of many possible errors that can arise when using such a probe molecule is false-positive detection via the probe reacting at a potentially catalytic surface, such as $LiCoO_2$ nanoparticles.[9] Experiments showed that detection of H_2O_2 using the Amplex Red (AR) assay in $LiCoO_2$-exposed solutions was statistically significant (Figure A.1.1A), indicating that H_2O_2 is the primary ROS generated from $LiCoO_2$ and should be further investigated. In the assay, AR and H_2O_2 react, with a horseradish peroxidase (HRP) catalyst, to produce the fluorescent resorufin. To ensure that positive results of the AR assay were due to the transformation of the AR to resorufin upon reaction with free H_2O_2 and not on the nanoparticle surfaces, we performed diffusion assays with $LiCoO_2$ suspension.

A.1.2 Experimental.

A solution of 100 μM Amplex Red and 0.1 unit·mL^{-1} horseradish peroxidase (AR-HRP) and a standard solution of 1 μM H_2O_2 were each prepared in minimal media with dextrose (the same media as other experiments). These concentrations were chosen based on prior work,[10] to maximize H_2O_2 capture and produce fluorescence within a reasonable range. Experiments were performed with/without $LiCoO_2$ particles, with/without spiked H_2O_2 (as a positive control), and were each performed in at least duplicate. Figure A.1.2 shows the device prepared for each sample to spatially separate the $LiCoO_2$ nanoparticles from the AR-HRP solution using a finely porous hydrophobic filter membrane (MF-Millipore, 25 nm pore size, 13 mm diameter). First, $LiCoO_2$ particles were pressed into indium foil on a copper plate to immobilize them. In the case of no-$LiCoO_2$ controls, indium pressed on copper was used. Next, 10 μL of minimal media with dextrose with/without 1 μM H_2O_2 (no AR-HRP) was added on the particle plate to promote dissolution, and in the case of H_2O_2 to simulate if H_2O_2 were produced by the particles. Then, a filter membrane disk is added on the plate, followed by an o-ring. 100 μL of the AR-HRP solution was added within the o-ring cavity, above the filter membrane. Finally, the o-ring is capped with a glass slide and sealed with a clamp. We allowed the particles to dissolve unstirred for 1 h, disassembled the device, and removed 50 μL from within the o-ring above the membrane. This extracted solution was diluted into 1 mL of minimal media with dextrose and analyzed by fluorescence spectroscopy with conditions similar to those used previously.[10] Intensity at the emission peak maximum (~582 nm) was used for quantification, with the AR-HRP-only negative control serving as a baseline. Approximate quantification of unknown H_2O_2 generated from $LiCoO_2$ samples was possible due to the known quantity of spiked H_2O_2 (i.e., standard addition).

A.1.3 Results and discussion.

We assembled an apparatus (Figure A.1.2) to spatially separate the $LiCoO_2$ nanoparticles from the AR-HRP solution using a finely porous hydrophobic filter membrane. Fluorescence of the resulting solution above the filter membrane (i.e., no direct particle exposure) is used to detect H_2O_2 with 1 μM H_2O_2 below the filter membrane as a standard. Under this experimental design, an increase in fluorescence would be from the reaction of AR with free H_2O_2 and not with the nanoparticle surfaces, assuming 1) H_2O_2 readily diffuses through the membrane, 2) $LiCoO_2$ cannot diffuse through the membrane (25 nm pores are small relative to particle diameter), and 3) HRP does not appreciably diffuse through the membrane within the time scale of the experiment. Although AR may diffuse through the membrane, conversion to the fluorescent product requires the HRP catalyst. Although we expect cobalt ions may also diffuse through the membrane, Co^{2+} alone did not induce fluorescence intensity change with AR in control experiments (data not shown).

Figure A.1.1B shows representative fluorescence spectra of each sample tested with the normalized fluorescence intensity normalized to the background. The presence of $LiCoO_2$ nanoparticles results in an increase in fluorescence compared to the AR-HRP control solution. Addition of 1 μM H_2O_2 spike produces a similar effect, indicating that H_2O_2 diffuses through the membrane over the 1-h period and reacts with

AR-HRP. The presence of $LiCoO_2$ particles alone (no AR-HRP) shows no fluorescence, with small background intensity coming from scattering of the excitation light. These results show that positive detection of H_2O_2 in our Amplex Red experiment (Figure A.1.1A) is indeed due to the presence of abiotic H_2O_2 and not direct interaction of AR with the $LiCoO_2$ nanoparticles. Therefore, we can conclude from the AR experiments that H_2O_2 is the primary abiotic ROS generated from $LiCoO_2$ upon cell exposure. This has implications in nanoparticle toxicity, which are discussed elsewhere in the paper (see cited article).

A.1.4 Figures.

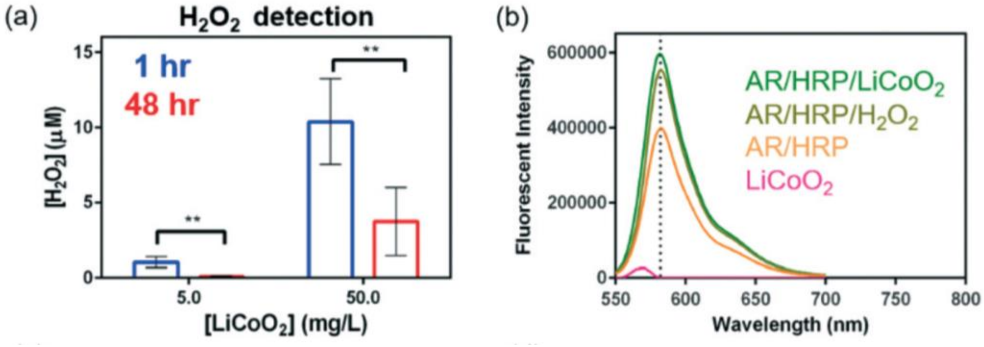

Figure A.1.1. Abiotic H_2O_2 detection in $LiCoO_2$ suspension after 1 h (blue) and 48 h (red) in minimal media with 10 mM dextrose. A) Quantification of H_2O_2 monitored by Amplex Red dye (n = 4, ** for $p < 0.01$ with two-way ANOVA with Sidak's multiple comparison test, and B) representative fluorescence spectra of 100 μM Amplex Red (AR) and 0.1 unit per mL horseradish peroxidase (HRP) solution after 1-h exposure through a filter membrane to $LiCo_2$ nanoparticles and/or 1 μM H_2O_2 standard solution.

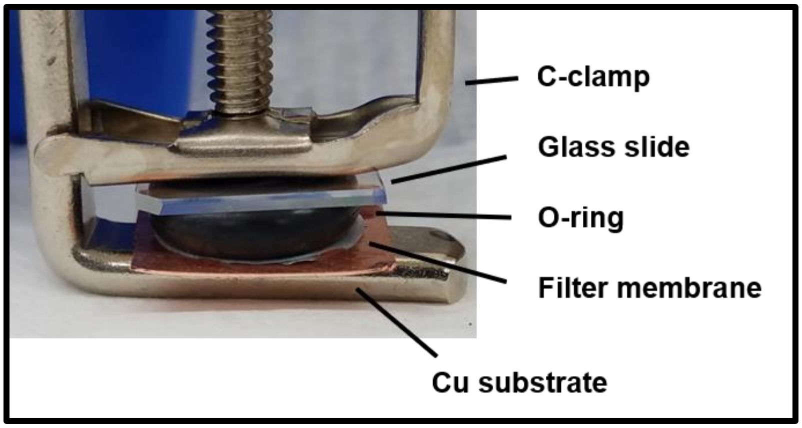

Figure A.1.2. Assembled device for diffusion assay of Amplex Red with $LiCoO_2$ dissolution. $LiCoO_2$ nanoparticles are between the filter membrane and the copper substrate. The AR-HRP solution removed for analysis is housed within the o-ring, above the filter membrane.

A.1.5 References.

1. Hang, M. N.; Gunsolus, I. L.; Wayland, H.; Melby, E. S.; Mensch, A. C.; Hurley, K. R.; Pedersen, J. A.; Haynes, C. L.; Hamers, R. J., Impact of Nanoscale Lithium Nickel Manganese Cobalt Oxide (NMC) on the Bacterium Shewanella Oneidensis MR-1. *Chem. Mater.* **2016**, *28*, 1092-1100.

2. Feng, Z. V.; Miller, B. R.; Linn, T. G.; Pho, T.; Hoang, K. N. L.; Hang, M. N.; Mitchell, S. L.; Hernandez, R. T.; Carlson, E. E.; Hamers, R. J., Biological Impact of Nanoscale Lithium Intercalating Complex Metal Oxides to Model Bacterium B. Subtilis. *Environ. Sci. Nano* **2019**, *6*, 305–314.

3. Bozich, J.; Hang, M.; Hamers, R.; Klaper, R., Core Chemistry Influences the Toxicity of Multicomponent Metal Oxide Nanomaterials, Lithium Nickel Manganese Cobalt Oxide, and Lithium Cobalt Oxide to Daphnia magna. *Environ. Toxicol. Chem.* **2017**, *36*, 9.

4. Yu, Z.; Li, Q.; Wang, J.; Yu, Y.; Wang, Y.; Zhou, Q.; Li, P., Reactive Oxygen Species-Related Nanoparticle Toxicity in the Biomedical Field. *Nanoscale Res. Lett.* **2020**, *15*, 115.

5. Dayem, A. A.; Hossain, M. K.; Lee, S. Bin; Kim, K.; Saha, S. K.; Yang, G. M.; Choi, H. Y.; Cho, S. G. The Role of Reactive Oxygen Species (ROS) in the Biological Activities of Metallic Nanoparticles. *Int. J. Mol. Sci.* **2017**, *18*, 1–21.

6. Qiu, T. A.; Gallagher, M. J.; Hudson-Smith, N. V.; Wu, J.; Krause, M. O. P.; Fortner, J. D.; Haynes, C. L., Research Highlights: Unveiling the Mechanisms Underlying Nanoparticle-Induced ROS Generation and Oxidative Stress. *Environ. Sci. Nano* **2016**, *3*, 940–945.

7. Qiu, T. A.; Clement, P. L.; Haynes, C. L., Linking Nanomaterial Properties to Biological Outcomes: Analytical Chemistry Challenges in Nanotoxicology for the next Decade. *Chem. Comm.* **2018**, *54*, 12787–12803.

8. Fernández-Castro, P.; Vallejo, M.; San Román, M. F.; Ortiz, I. Insight on the Fundamentals of

Advanced Oxidation Processes: Role and Review of the Determination Methods of Reactive Oxygen Species. *J. Chem. Tech. Biotech.* **2015**, *90*, 796–820.

9. Bartosz, G., Use of Spectroscopic Probes for Detection of Reactive Oxygen Species. *Clinica Chimica Acta* **2006**, *368*, 53–76.

10. Zhao, B; Summers F. A; Mason, R. P., Photooxidation of Amplex Red to Resorufin: Implications of Exposing the Amplex Red Assay to Light. *Free Radic. Biol. Med.* **2012**, *53*, 1080–1087.

Appendix 2. Developing a new discovery-based electrochemistry laboratory experiment for general chemistry on batteries and the Voltaic pile.

The following summarizes teaching and professional development work completed by Austin H. Henke under the supervision of Robert J. Hamers with assistance from Sarah L. Guillot and Chad C. Wilkinson. In this collaboration, we developed a laboratory experiment on electrochemistry for a second-semester general chemistry course (CHEM 104). Austin H. Henke, Sarah L. Guillot, and Chad C. Wilkinson equally contributed to experimental design. Austin H. Henke developed course materials (e.g., lab manual and staff notes entries) and analyzed student data. Chad C. Wilkinson and Austin H. Henke worked together to implement on the large class scale. Austin H. Henke had assistance from Devin Wixon within the Delta Program on teaching methodology, data analysis, and manuscript editing. We also acknowledge from Rachel Bain, Stephen B. Block, and Lea Gustin for assistance with experiment implementation and manuscript editing.

This work was supported by the National Science Foundation (NSF) under the Center for Sustainable Nanotechnology, CHE-2001611. The Center for Sustainable Nanotechnology is part of the NSF Centers for Chemical Innovation Program. This work was also supported by the University of Wisconsin – Madison General Chemistry Program.

A.2.1 Introduction.

As I have experience as a student and instructor, electrochemistry is typically taught at the end of the semester for second-semester general chemistry courses. While this fits a flow of concepts from kinetics

→ equilibrium → acids and bases → electrochemistry, it often leads to electrochemistry being rushed or portions of it skipped entirely. Additionally, traditional electrochemistry may be taught in a way that emphasizes memorizing conventions and equations instead of understanding fundamental concepts. Because of this, connections are not always made from abstract ideas (mathematics) to the many applications of electrochemistry in the world today. Restructuring the entire course is not ideal because of the natural synergy of topics presented above. Therefore, a change in electrochemistry curriculum is needed increase student engagement with electrochemistry content and make it more relatable.

Development of a laboratory experiment is an appealing option for improving electrochemistry curriculum. Laboratory experiments are a major form of active learning in most chemistry courses. Lab activities can be effectively employed both in terms of summative (longer research projects) and formative (short demonstrations) assessment.[1] Inquiry-based (or discovery-based) labs are one type in which students are not directly given the tasks they must complete but are given guidelines to ask and answer the right questions.[2] The active learning environment of the laboratory, and especially a discovery-based lab, promotes learning via different learning styles and increases accessibility of the content across diverse students: a key component of effective teaching.[3] An additional benefit of *group*-based laboratory exercise is that it fosters learning community among students, promoting peer-peer learning.[4] Therefore, collaboration should be a key component of new laboratory exercises. The previous general chemistry experiment on electrochemistry at UW-Madison was a “discovery-based exercise”.[5] However, I believe that primarily it was discovery-based in that lectures often fall behind and were not able to teach the content covered in the lab until after the lab. The lab activity itself was focused on the same mathematics, conventions, and equations covered in lecture, though it succeeded in illuminating a few key concepts and promoted group work. The goal of this work is to implement a new, sufficiently self-contained experiment with core inquiry and collaboration components and make it about a tangible topic: batteries. Additionally, students are required to work together not only with their assigned lab partner, but also analyze pooled class data and combine with other student groups to work towards a collective goal.

For hundreds of years scientists have explored the connections between chemical reactions and electricity. Two competing Italian scientists, Luigi Galvani and Alessandro Volta, pioneered this field in the 18th century. Galvani showed for the first time that electricity can be carried through a solution of charged ions, including biological tissue. Volta expanded on this work and invented the "Voltaic pile" (Figure A.2.1), one of the earliest known batteries. What better way to introduce electrochemistry and batteries than to have students recreate this iconic device from scratch? In this experiment, students construct and study Galvanic cells and a Voltaic pile to meet the learning objectives outlined in Table A.2.1.

A.2.2 Experimental.

This project addresses a topic and experiment done in General Chemistry II (CHEM 104) and Advanced General Chemistry (CHEM 109), both of which are 4 credit courses. These are typically composed of first- and second-year students, who are chemistry, biology, biochemistry, pre-med, or engineering (chemical, mechanical, etc.) majors. The experiment was piloted in CHEM 104, which has ~500 students in the fall semester, ~2100 students in the spring semester, and ~100 students in the summer, each split into lectures of ~300 students. Besides lecture, students attend a smaller (~22 students) discussion section twice a week, and lab once a week with the same group of students as their discussion. Because of the large number of students performing the experiment, practical considerations, such as cost and robustness, often influenced decisions of experimental design.

This experiment began as an outreach demonstration for children at local science festivals involving stacks of sanded U.S. pennies and pieces of cardboard soaking in a salty vinegar solution (~1 M NaCl in acetic acid): a common demonstration that has been done previously. In this design, the pennies serve as both cathodes and anodes for a stack of Galvanic cells. For U.S. pennies made on or after 1983, the surface is Cu, while the core is Zn. When the Cu surface is sanded or etched away, there are two metals with differing reduction potentials that can generate a voltage when multiple pennies are put in contact across an electrolyte. Cardboard or other thick paper was a suitable separator to prevent short-circuiting while allowing ions to flow. We use NaCl as the electrolyte, but the addition of acetic acid is needed to dissolve a small amount of each metal ion, such that the corresponding reduction reaction can occur (Eq. A.2).

$$Zn^0 \rightarrow Zn^{2+} + 2e^- \qquad \text{Eq. A.1}$$

$$Cu^{2+} + 2e^- \rightarrow Cu^0 \qquad \text{Eq. A.2}$$

Building a stack of multiple pennies gave the children a hands-on way to experience electrochemistry. The stacks can produce sufficient voltage to light an LED or sound a buzzer.

To expand the experiment to reach the college-level learning objectives in Table A.2.1 and be consistently completable by hundreds of students at low cost, several modifications were made. First, pennies were replaced by metal sheets of various metals (Co, Ni, Fe, Zn, Cu, Ti, Mo, W, V, Mn) cut into hexagons. This is because 1) pennies are limited to only two metals (Cu and Zn) and we wanted students to observe trends across more element combinations, and 2) removal of the Cu surface to expose the Zn core was labor intensive for large quantities of pennies. Metal sheets were cut into hexagons to optimize material usage and maintain a size and shape similar to the circular penny. Second, the separator was changed from cardboard to a hydrogel. Soaked cardboard, filter paper, felt, and other papers allowed sufficient ion flow to measure potential differences, however, they were too resistive to allow sufficient current to drive electrolysis. Additionally, there were problems of the separators drying out or folding over to create a short-circuit by touching another separator or electrode. Hydrogel disks solve all of these problems by providing a robust, conductive, inexpensive, moderately rigid separator that can be soaked in the same electrolytes and reused multiple times. Hydrogel sheets were prepared using previously described procedures[6, 7] and cut into disks of similar size to the metal pieces. Lastly, we needed to change the way the Voltaic pile was packaged to make the experiment robust and allow student groups to move around the lab and combine their Voltaic piles. To do this, we added U.S. penny roles as a scaffold to build and contain a Voltaic pile, and to have metal plates with soldered wires at the top and bottom for easy electrical connection (Figure A.2.2).

Together, these changes transformed a small-scale demonstration into a course-wide experiment. Compared to the previous electrochemical cells experiment,[5] the proposed experiment has significantly reduced long-term cost. The previous electrochemical cells experiment required large quantities (several liters) of 1 M solutions of multiple metal salts, including $AgNO_3$. For the proposed experiment, all reagents and materials are relatively inexpensive (NaCl, vinegar, penny rolls, wires, hydrogel). While the up-front cost of metal plates is significant, these can be reused for many years. Therefore, this experiment benefits the General Chemistry program by greatly (~50%) reducing cost for that lab period.

The experiment was first piloted at University of Wisconsin – Madison in Summer 2019, followed by the first full trial in Fall 2019. A selection of the lab manual entry is shown below describing the procedure and answer sheet questions. Table A.2.2 shows a list of all reagents and materials needed to complete the experiment. Students completed the experiment concurrently with lecture material covering electrochemistry. Since individual lab periods where spread over a week, individual students experienced the lab at different times relative to exposure to the material in lecture. Two surveys ("pre-lab" and "post-lab") were performed using Qualtrics to assess content and affective learning objectives, as well as to find ways to improve the experiment. The optional, ungraded surveys were made available through the course Canvas page for one week leading up to the laboratory period (pre-lab) and for one week following the laboratory period (post-lab). Responses were correlated to quantify changes, while removing personally identifying information to maintain anonymity. Sample size varied across questions and is indicated in each figure when relevant. Survey questions from the post-lab survey are found in section A.2.5 (pre-lab was a subset of these questions). Demographic information was not included in the survey.

Part A. Developing an Electromotive Series from Galvanic Cells

1. Obtain one piece of each available metal. Also obtain one conductive hydrogel disk and gently pat it dry with a paper towel. Your lab instructor will assign you a metal to study.

2. Polish the metals, other than chromium, using a piece of sand cloth.

3. Prepare a cell consisting of a stack formed by sandwiching a conductive hydrogel disk between a piece of your assigned metal and any other metal. Measure the voltage by touching the red (positive) lead to your assigned metal and the black (negative) lead to the other. Record the magnitude and sign of the potential. Switch the connections. What happens to the voltage? Can you use this to identify the anode and cathode?

4. Repeat the procedure above until you have assembled and measured cells consisting of your assigned metal and each of the other metals. Report your findings for the assigned metal at the positive lead to your lab instructor. Record in your notebook the assembled community data. See the report sheet for a convenient way of doing so.

5. Obtain a second piece of your assigned metal and a second piece of any one of the unassigned metals, along with a second hydrogel disk. Prepare two cells consisting of your assigned metal and the chosen unassigned metal. Stack the two cells so that the assigned metal of one cell contacts the unassigned metal of the other cell (an ABCABC pattern, where "B" is the hydrogel and "A" and "C" are each metal). For example, in a copper-iron cell, the copper disk of one cell should directly contact the iron disk of the next. Measure the voltage of the two-cell stack. How does this relate to a single-cell stack?

Part B. Preparing a Voltaic Pile and Lighting LEDs

Your goal is to design and assemble a voltaic pile capable of lighting red and blue LEDs and driving an electrolysis of water. Examine the data the class has collected and choose which metals will comprise your voltaic pile. You do not have to use the metal assigned in Part A. Note that there may not be enough of a given metal for all groups to use the same metal (there may not be enough copper to go around, for example), so have backup plans for alternative cells. You will need to achieve a voltage of at least 5.0 V, with **no more than 10 cells**. Figure A.2.2 illustrates the different steps of the voltaic pile construction. Make sure to polish all metal surfaces, as needed, before assembly.

1. Cut a slit out of the side of a penny roll wide enough for the forceps to easily slide up and down the length of the penny roll (Figure A.2.2A). Place a copper-taped penny (polish the untaped side) at the bottom end of a penny roll (the end with a rolled ring) with copper tape facing out (Figure A.2.2B). This serves as a conductive foundation.

2. Assemble a cell with your chosen metals in the same manner as Step 5 in Part A. Load the metal pieces and hydrogel spacers into the penny roll, using the forceps to aid in the placement of each piece. You may need to gently pat dry the hydrogels. Measure the voltage after the addition of each cell. **For consistency, place the metal with more positive potential in each pair on the bottom**.

3. Stack additional cells **in series** to reach the required voltages below, one cell atop the other (Figures A.2.2C-D), with the stack order following the ABCABC pattern mentioned above (measuring and recording the voltage of the pile upon the addition of each stack).

4. Once you have a cell that measures between 1.8 and 2.4 V, cap the pile with another copper-taped penny (tape facing outward, Figure A.2.2E). Connect the alligator clip connection wires to the copper tape at one end and the LED at the other, paying attention to which end of your pile is the cathode and which is the anode. Attempt to light both the red and blue LEDs. Record your observations.

5. Remove the penny cap and continue adding cells until your pile measures at least 3.0 V. Repeat the above procedure and attempt to light both the red and blue LEDs. Record your observations.

6. Remove the cap and continue adding stacks until the final target voltage of 5 V is achieved. Once the final cell has been placed, cap the stack with the copper-taped penny. Cut a second slit into the penny roll opposite the first one, and only down to the height of the stack. Fold over the paper of the penny roll, squeeze together the voltaic pile, and **tightly** secure in place with a piece of tape (Figure A.2.2). Label the positive (+) and negative (-) sides of your voltaic pile battery.

7. Examine the dissected commercial battery and compare it to the voltaic pile you created.

Part C. Driving an Electrolytic Cell

For Part C, you will be working with up to three other student groups (up to 4 voltaic piles).

1. One for each super-group: fill a 50 mL beaker with ~25 mL 0.1 M Na_2SO_4 (not the vinegar solution used to soak hydrogels). Insert two copper wires into the solution, with the tops exposed to make electrical contact. The wires should be close together but not touching. Secure the wires to the beaker with small pieces of tape. You may need to sand the wires, similarly as with the metal pieces in Part A. Record observations of the assembly before any power supply is connected.

2. Connect a current probe to the LabQuest, configured as a meter. Connect the alligator clips of the current probe to both ends of your voltaic pile. The reading may be unstable but take a current measurement. Disconnect your voltaic pile from the current probe. Using a pair of the alligator clip connection wires, connect the wires of a single voltaic pile to the two copper wires. Record your observations.

3. Disconnect the voltaic pile from the electrolytic cell. Using a second pair of alligator clip connection wires, connect a second voltaic pile from another group, **in parallel**, to yours. When connecting the piles, make sure to connect anode to anode and cathode to cathode. Measure the voltage and current by connecting the corresponding clips to the parallel piles (one measurement after the other, not at the same time), before connecting your piles to the electrolytic cell. Record your observations.

4. Work with other groups to add a third, and then a fourth (if possible) voltaic pile, in parallel. After each addition measure the voltage and current and reconnect to the electrolytic cell. Record your observations.

5. Disconnect the alligator clips of the power supply from the electrolytic cell. If bubbles are present, **gently** tap the beaker against the bench and/or gently shake the copper wires to remove them.

6. Add ~5 drops of universal indicator to the electrolytic cell solution and briefly stir. Once the solution is **homogenous and at rest**, reconnect the 4-stack power supply. Record your observations. Perturb the solution by stirring with a stirring rod or spatula and record your observations.

7. In a separate beaker (one per super-group), assemble a new electrolytic cell consisting of two copper wires dipped in ~25 mL DI water **instead of** 0.1 M Na_2SO_4. Connect the 4-stack power supply and record your observations.

8. Disassemble your voltaic piles. Record your observations regarding the metal disks as you conduct the disassembly. Return all metal and hydrogel disks to their appropriate containers.

Observed Cell Potentials **(with example data filled in)**

Cell Potential (V)		**Positive (Red) Lead**										
		Cu	**Zn**	**Fe**	**Ni**	**Co**	**Ti**	**Mo**	**W**	**Mn**	**Cr**	**V**
Negative (Black) Lead	**Cu**		-0.994	-0.512	+0.007	-0.361	+0.003	+0.036	+0.002	-1.324	+0.528	
	Zn	0.994		+0.452	+0.973	+0.615	+0.984	+1.030	+1.006	-0.334	+0.650	
	Fe	0.512	-0.452		+0.529	+0.193	+0.539	+0.558	+0.552	-0.774	+0.390	
	Ni	-0.007	-0.973	-0.529		-0.345	+0.037	+0.052	+0.005	-1.308	-0.381	
	Co	0.361	-0.615	-0.193	0.345		+0.360	+0.408	+0.360	-0.965	-0.015	
	Ti	-0.003	-0.984	-0.539	-0.037	-0.36		+0.026	-0.018	-1.350	-0.338	
	Mo	-0.036	-1.03	-0.558	-0.052	-0.408	-0.026		-0.015	-1.393	-0.222	
	W	-0.002	-1.006	-0.552	-0.005	-0.36	0.018	0.015		-1.319	-0.316	
	Mn	1.324	0.334	0.774	1.308	0.965	1.35	1.393	1.319		+1.125	
	Cr	-0.528	-0.65	-0.39	0.381	0.015	0.338	0.222	0.316	-1.125		
	V											

Electromotive series (from easiest to oxidize to hardest to oxidize)

_______>_______>_______>_______>_______>_______>_______>_______>_______>_______

Voltaic Pile

Metals chosen: Anode: _________ Cathode: __________

Quantity in the Stack	1	2	3	4	5	6	7	8	9	10
Potential (V)										

Potential to light Red LED: _________________ Potential to light Blue LED: ________________

1. From your observations, how is the potential difference (voltage) of individual voltaic cells affected when the cells are added together in series? In parallel? Use Figure 3 to guide your explanation.

2. Compare the minimum potentials required to light each LED. How does the required potential relate to the energy/wavelength of the emitted light?

3. Explain why DI water connected to the power supply cannot be electrolyzed, even though the reactant (H_2O) is present in abundance and the same power supply is connected as in the case of the Na_2SO_4 electrolysis solution.

4. When electrolyzing the universal indicator solution, what processes are responsible for any color changes you observed? Include a chemical reaction in your explanation.

5. Explain why two copper wires can be used as electrodes for the electrolysis in Part C, and yet in Part A two different metal electrodes are required to produce a measurable potential.

6. What are some similarities and differences between your voltaic pile and the commercial battery? Given that the commercial battery produces a total potential of 12 V, what is the potential of each individual cell?

A.2.3 Results and discussion.

Through constructing Galvanic cells and the Voltaic pile in collaboration, students can measure potential differences, understand how Galvanic cells add in parallel and in series, relate theory of electrochemistry to batteries, and power LEDs and electrolysis with their own devices. The table in the lab manual entry of section A.2.2 shows example potential differences across each metal combination. From these measurements, students can deduce which metals are stronger or weaker reducing agents and create an electromotive series. Each student pair only measures one column of these data (one metal vs. all other metals) to save time, so they must rely on pooled class data. An approximate electromotive series is shown below in Eq. A.3:

$$\text{(most reducing)}\quad \text{Mn} > \text{Zn} > \text{Fe} > \text{Co} > \text{Cr}^* > \text{Ni}^* > \text{W}^* > \text{Cu} > \text{Ti} > \text{Mo} \qquad \text{Eq. A.3}$$

Those shown with * indicate elements that are difficult to distinguish due to having near-zero potential differences when paired (similar reducing strength). This may reflect these metals not sufficiently dissolving in the acetic acid electrolyte to produce ions needed for the reduction half reaction, as mentioned in section A.2.1. Therefore, students recognize that certain metal combinations are preferred to generate a higher voltage and should choose accordingly. For example, Zn, Mn, and Fe are most easily oxidized and so make excellent anodes for the Voltaic pile. This order can be verified by comparing to tabulated standard reduction potentials, though only qualitatively (as this experiment is not under standard conditions). When building the Voltaic pile of two suitable metals (Figure A.2.2), students observe that voltages of Galvanic cells added in series are additive. This is the case for any voltage source in a circuit according to Ohm's Law, which connects to physic curriculum and relates the pile to a battery. Eventually, the pile reachs sufficient voltage to light LEDs and perform electrolysis (Figure A.2.3). The red and blue LEDs used require different onset potentials (Figure A.2.4), which the students estimate given the measured potentials of the stack when they light. Compared to lighting the LED, conducting electrolysis at copper wires in the beaker of electrolyte requires a high current. Because of this, students collaborate and connect multiple Voltaic piles in parallel (Figure A.2.3B). During experiment development, three or four well-made piles was determined sufficient to observe bubble formation. Once the piles are connected to the electrolyte via the copper electrodes, bubbles form on at least one electrode, corresponding to reduction of $H_2O_{(l)}$ to $H_{2(g)}$. The opposing oxidation of $H_2O_{(l)}$ to $O_{2(g)}$ is likely not visible due to kinetic overpotential on most electrode materials.[8, 9] With the addition of universal indicator, or another pH indicator of near-neutral pH sensitivity, students observe increase in pH at the electrode producing $H_{2(g)}$ when the solution is unstirred, corresponding to loss of H^+ in the region near the electrode (Figure A.2.3C). Therefore, in this discovery exercise students are taken from beginning to end of *designing*, *building*, *understanding*, and *using* their own battery.

In experiment development and live observation of students performing the experiment, we note several common problems. First, in construction of the Voltaic pile it is important for the plates and hydrogels to be squeezed tightly together to ensure there is no air gap for one or more of the couples (open circuit). Second, student data from procedure Part A (potential difference measurements) may be incorrect, or students may choose inappropriate metal combinations. The problem is worst if students select a combination of metals mentioned above as having very similar reducing strengths. This can be prevented by lab instructors periodically checking with students on their technique, data, and choices. Third, combined Voltaic piles in procedure Part C may not generate sufficient voltage or current perform electrolysis. This may be due to one or more of the piles being improperly constructed or having a lower voltage and essentially "draining" the connected piles. Solutions to this are to measure each Voltaic pile to identify to problem, switch in Voltaic piles from other student groups, or add additional Voltaic piles in parallel. Lastly, students may use the incorrect metal, either by their own accident or a previous student returning the metal to an incorrect container. Most of the metal pieces are difficult to distinguish since they were all cut into hexagons and have a similar silver-gray color. Cu, Mn, and Cr can be distinguished by their colors or textures. The remaining metals were sorted by staff according to magnetic properties (Co, Ni, and Fe are ferromagnetic) and density. Instructors can convey information on magnetism and density to students, but they may not accurately apply it. Therefore, an identification system is needed. We have proposed implementing a notch system on two sides of the hexagons with sufficient combinations to differentiate every metal. This is advantageous over writing or etching labels onto the flat surfaces of the hexagons because students sand these surfaces to remove any oxide layer or corrosion from previous use. Together, these problems can be addressed by department staff and instructors to improve the student experience.

According the pre- and post-lab survey results, students not only learned about electrochemistry, but gained confidence and appreciation for electrochemistry and group work. The one question in surveys assessing content learning objectives was the multiple-choice question: “In some portable electronic devices, why might there be multiple batteries present?”. The aggregated results in Figure A.2.5 show that before and after the experiment the correct response, “To increase the overall voltage and/or current output”, was most selected. The large number of correct student responses prior to performing the experiment may reflect intuition or knowledge from a prior course. However, after performing the experiment, the percentage of correct responses increases from 49.8% to 80.6%. Such an increase reflects the experiment fulfilling part of learning objectives one and two in Table A.2.1 by showing that the Galvanic cells add voltage in series, and that multiple Voltaic piles are required to reach a current necessary for electrolysis. We cannot draw further conclusions about content learning objectives, as no data was recorded on answer sheet responses, the other source of content assessment. However, other survey questions give plentiful insight into affective learning objectives. Students display marked increased confidence in understanding and explaining how a battery works after completing the experiment, as shown in Figures A.2.6 and A.2.7.

In Figure A.2.6, the bulk of responses classified in the region of “not at all confident” shifts much higher towards “very confident”. Figure A.2.7 also shows that after the lab most students are better able to relate electrochemistry to real-life applications. Since the data in Figure A.2.7 are correlate per student, we can see that increased confidence and appreciation are frequently paired (with the top right quadrant being most populated). These objectives may be fulfilled by the discovery nature of the experiment and connection of Voltaic piles to batteries. Lastly, one question in the pre- and post-lab surveys assess student perceptions of collaboration in chemistry (How much do you agree with: “Collaboration in chemistry labs promotes success?”). Figure A.2.8 shows that both before and after the experiment students value collaboration, with over 4 out of 5 choosing “somewhat agree” or higher. This experiment seems to have had a slight positive effect in that the fraction of responses “slightly disagree” to “strongly disagree” decreases after students have performed the experiment, due to collaboration being necessary to experiment success (by design). We are encouraged to see that students are innately value collaboration in science and that experiments featuring it can improve this further. In the qualitative response portion of the survey, one student said, “More labs should require multiple lab groups collaborating together like this one does.” These positive survey results, reduced cost compared to the previous electrochemistry experiment, and overall success of the experiments execution with students in Fall 2019 show that this experiment is a worthy addition to the University of Wisconsin – Madison General Chemistry curriculum.

A.2.4 Figures.

Figure A.2.1. Historical Voltaic pile (Como, Italy) made by A. Volta circa 1799.

Table A.2.1. Backwards design of activities and assessments from content and affective learning objectives.

Learning Objectives	Assessments	Activities
To assemble galvanic cell, voltaic pile, and electrolytic cell	Report sheet cell potentials, voltaic pile potentials, success in lighting LEDs, etc.	Parts A, B, and C of the lab activity, respectively
To apply galvanic cell models to batteries.	Report sheet questions	Part B of the lab activity and report sheet questions
To design a voltaic pile with a desired voltage to conduct an electrolysis	Report sheet voltaic pile potentials, success in electrolysis	They design a cell in Part B, and use it to conduct electrolysis in Part C.
To explain how a galvanic cell produces electrical energy and how and why an electrolytic cell requires energy.	Pre-lab questions, report sheet questions	In Parts A/B students measure voltages produced by various cells and observe them lighting LEDs, as a function of different metal-metal combinations. In Part C, they examine what cell connections are required to initiate electrolysis.
To collaborate with other student groups and draw conclusions from pooled data	Ability for combined groups to conduct electrolysis together, how well student data matches one another (in cases where there is overlap), pre/post survey questions	The activity is done in pairs. Data for Part A is pooled such that each group is assigned one metal (~9 total) and share data to draw conclusions. In Part C, groups combine their voltaic piles to achieve a common goal.
To increase confidence in electrochemistry content / unit.	Pre/post survey questions	Full activity

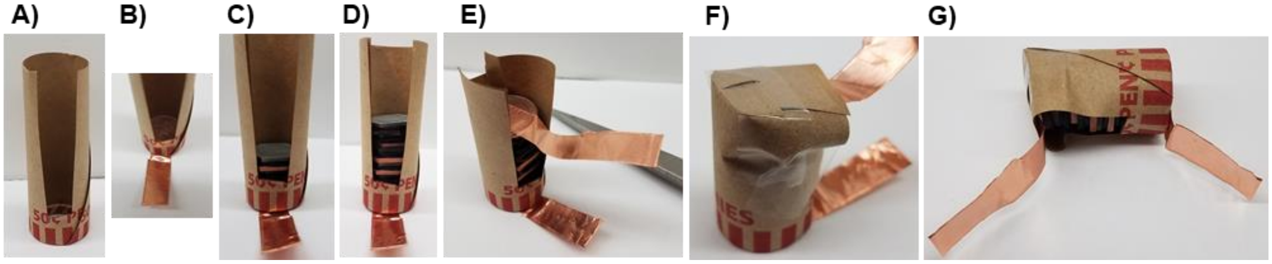

Figure A.2.2. Assembly of the modern Voltaic pile with metal plate electrodes, hydrogel seperators, penny roll scaffold, and Cu tape connections.

Table A.2.2. List of required materials and reagents to perform the Voltaic pile experiment.

Washables	Equipment	Reagents/Consumables
50 mL beaker x 2 (per "super group")	Metal pieces cut into flat hexagons, disks, etc. • zinc • copper • nickel • cobalt • iron • manganese • titanium • molybdenum • tungsten • chromium • vanadium Conductive hydrogel disks Forceps Copper wire Alligator clip connection wire (one red, one black) Voltage probe (LabQuest) Current probe (LabQuest) Blue LED Red LED Pennies with copper tape	0.1 M Na_2SO_4 (aq) 0.1 M Na_2SO_4 in vinegar Universal indicator Penny roll Tape

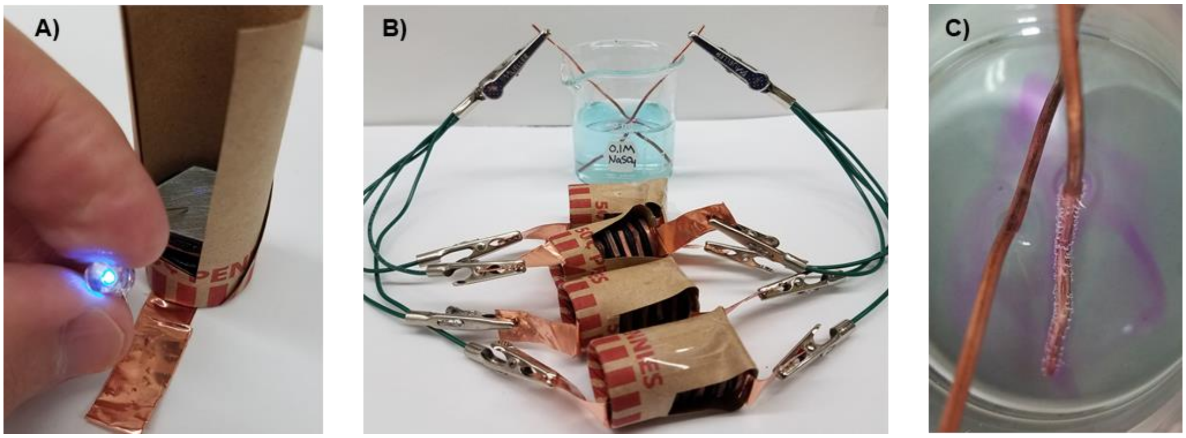

Figure A.2.3. A) Partially completed Voltaic pile of Zn and Cu lighting a blue LED. B) Four Zn/Cu Voltaic piles connected in parallel to copper wires in an unstirred solution containing 0.1 M $NaSO_4$ and universal indicator. C) Enlargement of beaker seen in B after about 20 seconds of electrolysis. On the right wire, there are H_2 bubbles on the right wire, and surrounding it are swirls of purple in the otherwise blue solution, indicating increase in local pH.

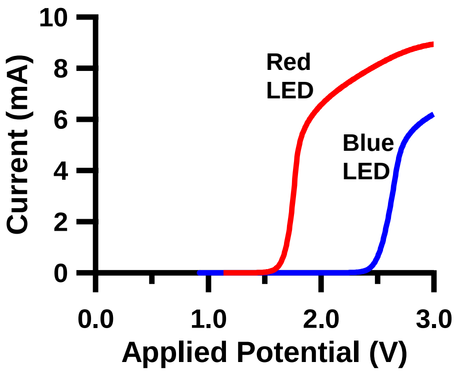

Figure A.2.4. Linear sweep voltammograms of red and blue LEDs, showing the onset potentials for illumination (~1.7 V for red and ~2.5 V for blue).

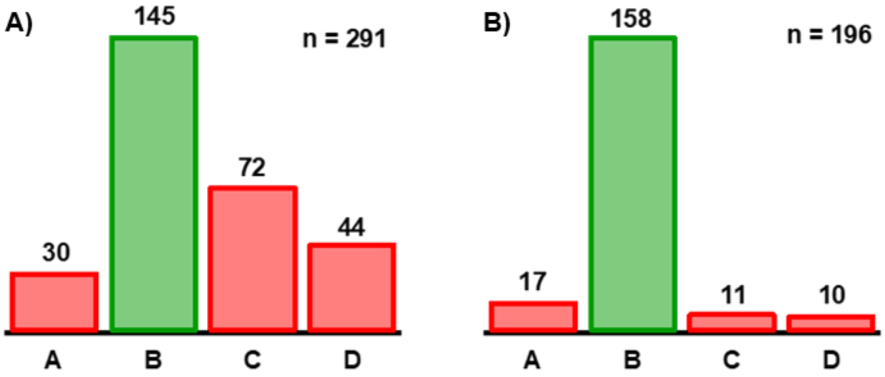

Figure A.2.5. A) Pre-lab and B) post-lab student responses to the survey question: “In some portable electronic devices, why might there be multiple batteries present?” with response options:

A. One or more are extra in case the primary battery fails.
B. To increase the overall voltage and/or current output.
C. One battery is the anode, and one battery is the cathode.
D. They power different components.

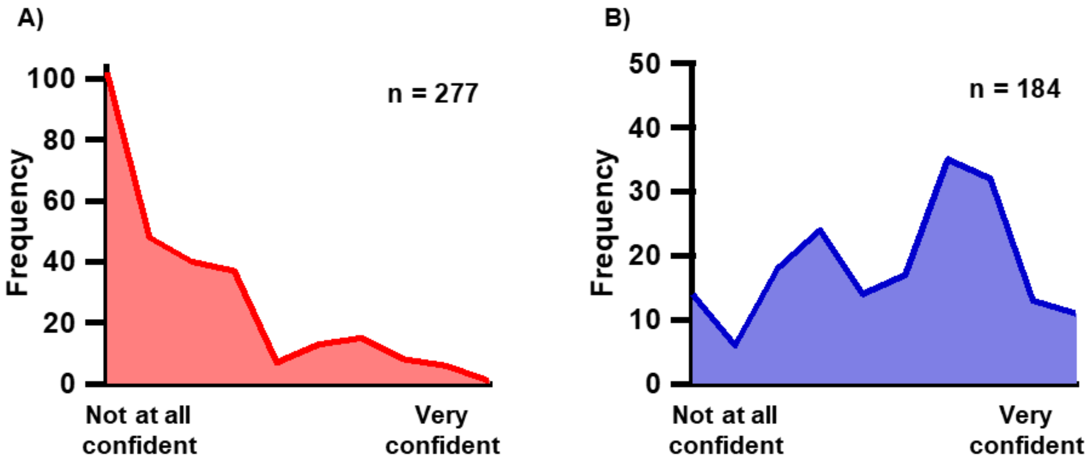

Figure A.2.6. A) Pre-lab and B) post-lab student responses to the survey question: "How confident would you be to explain how a battery works to a family member of friend?" with ten increments ranging from "not at all confident" to "very confident".

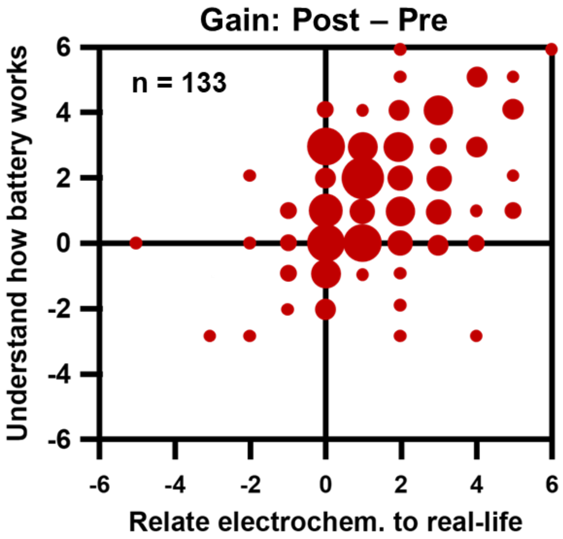

Figure A.2.7. Each axis represents the post-lab – pre-lab ratings (correlated per student) for the following questions. How much do you agree with: "I understand how a battery works" and "I relate what I learn about electrochemistry to real-life applications", respectively. A positive value indicates improvement and zero indicates no change. Each circle reflects the number of students at that coordinate.

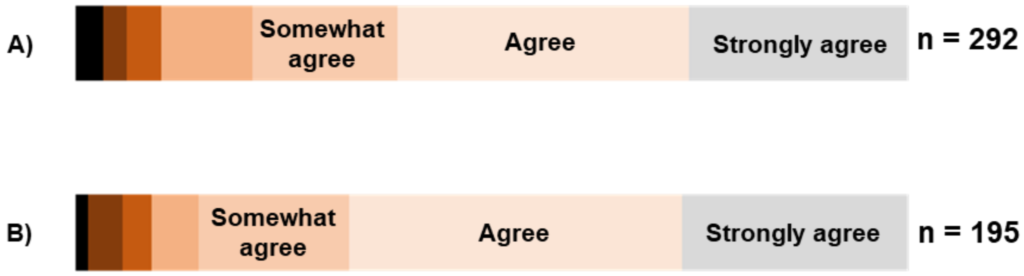

Figure A.2.8. A) Pre-lab and B) post-lab student responses to the survey question: "How much do you agree with: Collaboration in chemistry labs promotes success?" with six options ranging from strongly disagree to strongly agree. "Somewhat agree", "agree", and "strongly agree" are highlighted as those represent the vast majority.

A.2.5 Post-lab survey questions.

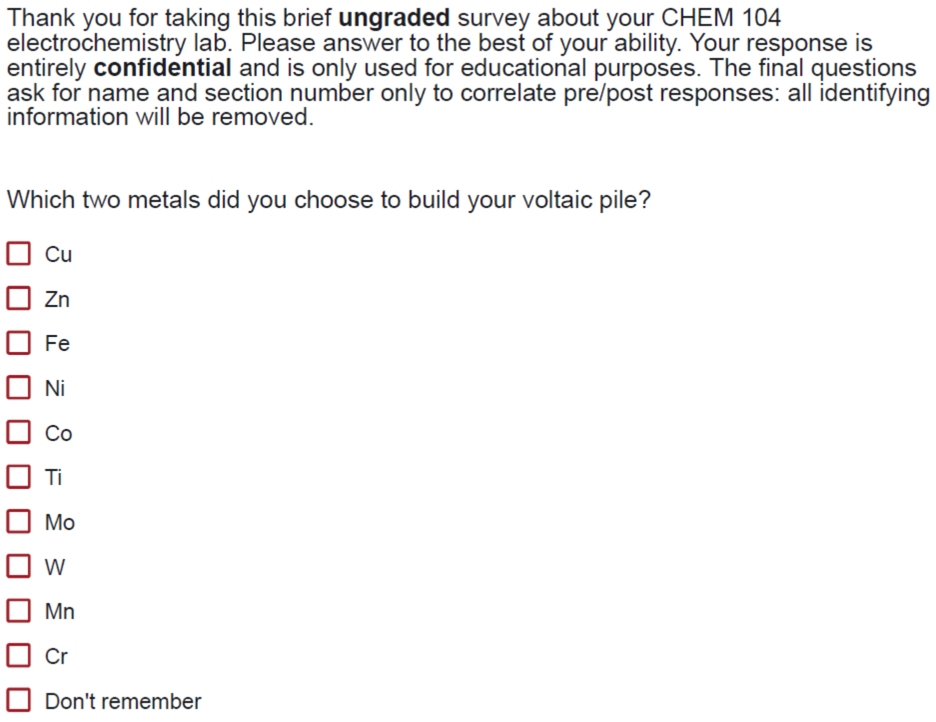

Thank you for taking this brief **ungraded** survey about your CHEM 104 electrochemistry lab. Please answer to the best of your ability. Your response is entirely **confidential** and is only used for educational purposes. The final questions ask for name and section number only to correlate pre/post responses: all identifying information will be removed.

Which two metals did you choose to build your voltaic pile?

☐ Cu
☐ Zn
☐ Fe
☐ Ni
☐ Co
☐ Ti
☐ Mo
☐ W
☐ Mn
☐ Cr
☐ Don't remember

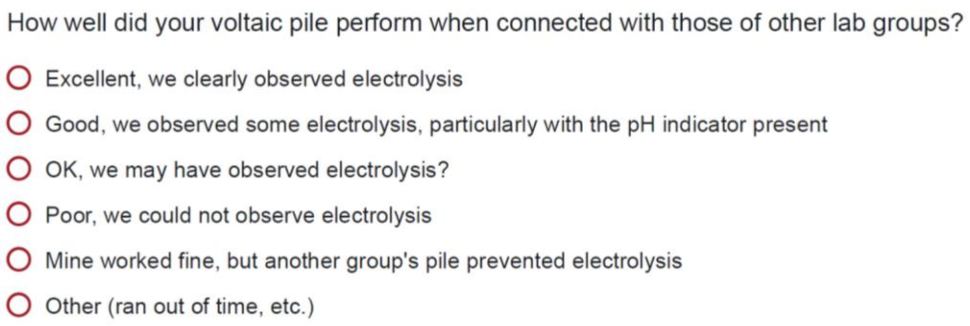

How well did your voltaic pile perform when connected with those of other lab groups?

○ Excellent, we clearly observed electrolysis

○ Good, we observed some electrolysis, particularly with the pH indicator present

○ OK, we may have observed electrolysis?

○ Poor, we could not observe electrolysis

○ Mine worked fine, but another group's pile prevented electrolysis

○ Other (ran out of time, etc.)

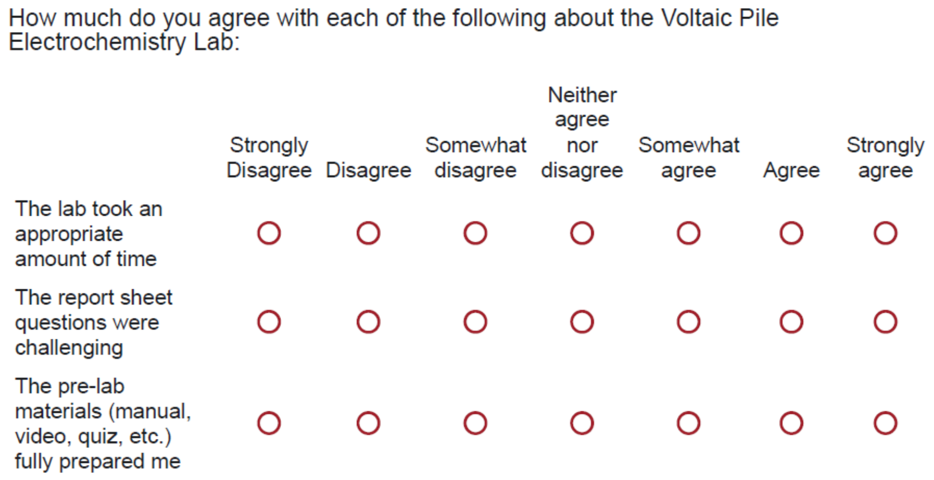

How much do you agree with each of the following about the Voltaic Pile Electrochemistry Lab:

	Strongly Disagree	Disagree	Somewhat disagree	Neither agree nor disagree	Somewhat agree	Agree	Strongly agree
The lab took an appropriate amount of time	○	○	○	○	○	○	○
The report sheet questions were challenging	○	○	○	○	○	○	○
The pre-lab materials (manual, video, quiz, etc.) fully prepared me	○	○	○	○	○	○	○

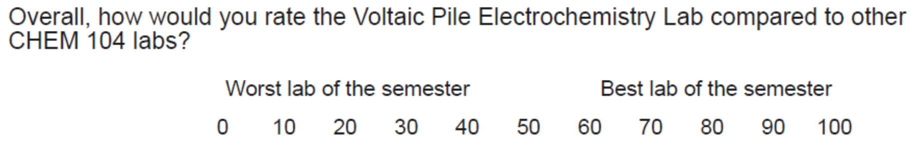

Overall, how would you rate the Voltaic Pile Electrochemistry Lab compared to other CHEM 104 labs?

Worst lab of the semester Best lab of the semester

0 10 20 30 40 50 60 70 80 90 100

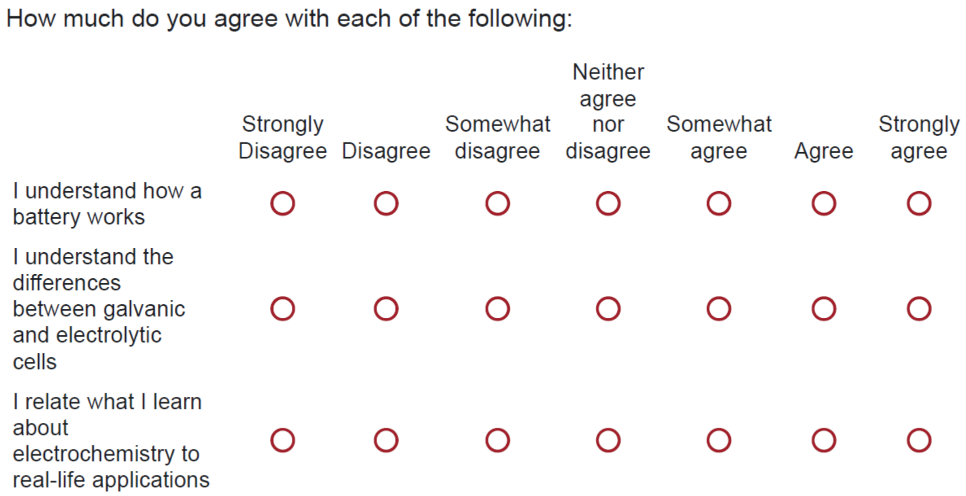

How much do you agree with each of the following:

	Strongly Disagree	Disagree	Somewhat disagree	Neither agree nor disagree	Somewhat agree	Agree	Strongly agree
I understand how a battery works	○	○	○	○	○	○	○
I understand the differences between galvanic and electrolytic cells	○	○	○	○	○	○	○
I relate what I learn about electrochemistry to real-life applications	○	○	○	○	○	○	○

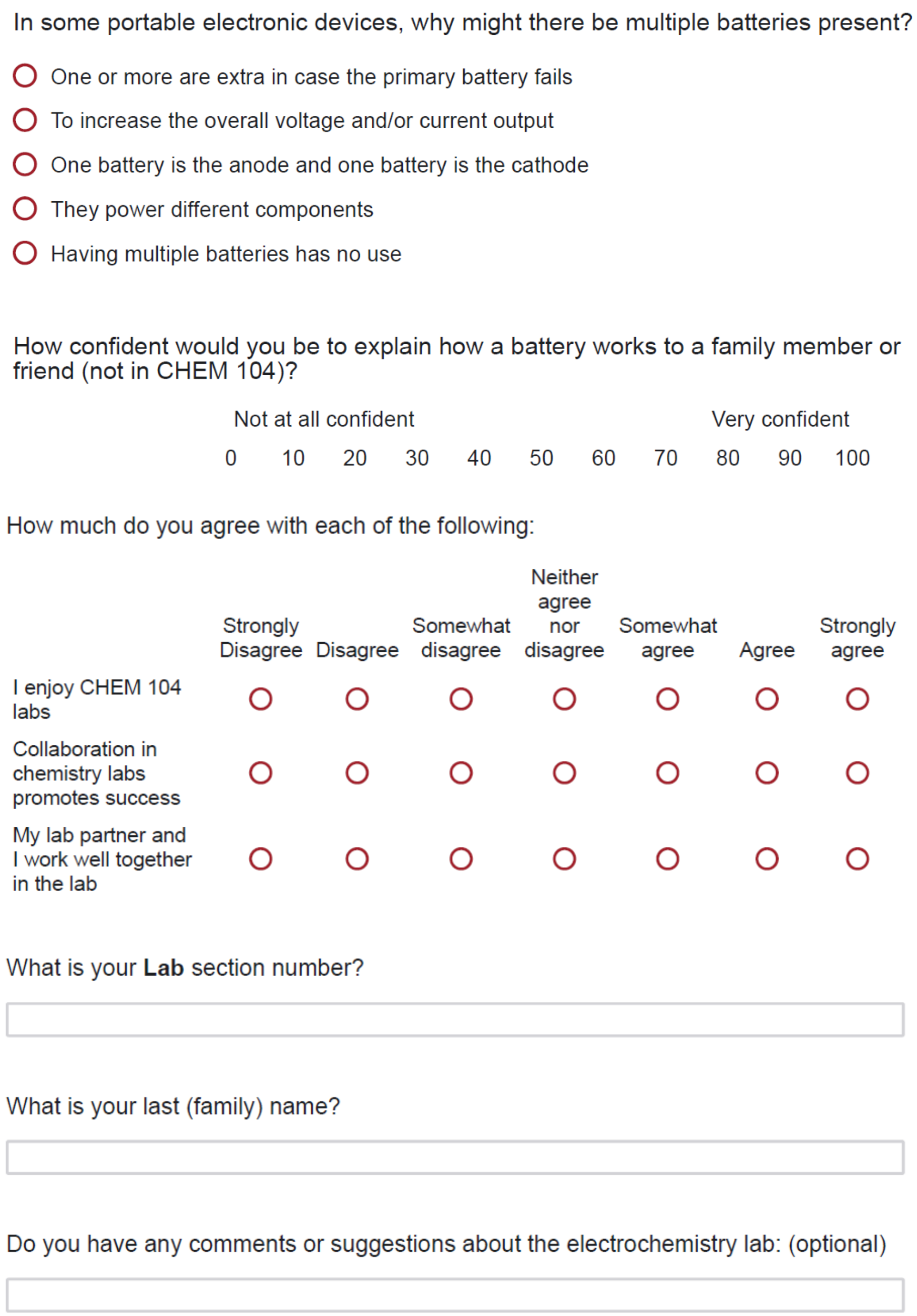

In some portable electronic devices, why might there be multiple batteries present?

○ One or more are extra in case the primary battery fails
○ To increase the overall voltage and/or current output
○ One battery is the anode and one battery is the cathode
○ They power different components
○ Having multiple batteries has no use

How confident would you be to explain how a battery works to a family member or friend (not in CHEM 104)?

Not at all confident — Very confident
0 10 20 30 40 50 60 70 80 90 100

How much do you agree with each of the following:

	Strongly Disagree	Disagree	Somewhat disagree	Neither agree nor disagree	Somewhat agree	Agree	Strongly agree
I enjoy CHEM 104 labs	○	○	○	○	○	○	○
Collaboration in chemistry labs promotes success	○	○	○	○	○	○	○
My lab partner and I work well together in the lab	○	○	○	○	○	○	○

What is your **Lab** section number?

What is your last (family) name?

Do you have any comments or suggestions about the electrochemistry lab: (optional)

A.2.6 References.

1. Branan, D.; Morgan, M., Mini-Lab Activities: Inquiry-Based Lab Activities for Formative Assessment. *J. Chem. Ed.* **2010**, *87*, 69–72.

2. Shiland, T. W., Constructivism: The Implications for Laboratory Work. *J. Chem. Ed.* **1999**, *76*, 107–109.

3. Rose, D. H.; Meyer, A., “Teaching Every Student in the Digital Age: Universal Design for Learning”, Alexandria, VA: ASCD, **2002**.

4. Jones, K. A.; Jones, J. L., Making Cooperative Learning Work in the College Classroom : An Application of the ‘Five Pillars’ of Cooperative Learning to Post-Secondary Instruction. *J. Eff. Teach.* **2008**, 61–76.

5. March, J.; Bain, G.; Wilkinson, C. C.; Moore, J. W. “Electrochemical Cells – A Discovery Exercise”, **2016**.

6. Hu, C.; Zhang, Y.; Wang, X.; Xing, L.; Shi, L.; Ran, R., Stable, Strain-Sensitive Conductive Hydrogel with Antifreezing. *Appl. Mater. Interfaces* **2018**, *10*, 44000–44010.

7. Shi, Y.; Pan, L.; Liu, B.; Wang, Y.; Cui, Y.; Bao, Z.; Yu, G., Nanostructured Conductive Polypyrrole Hydrogels as High-performance, Flexible Supercapacitor Electrodes. *J. Mater. Chem. A* **2014**, *2*, 6086–6091.

8. Bockris, J. O.; Shamshul Huq, A. K. M., The Mechanism of the Electrolytic Evolution of Oxygen on Platinum. *Proc. R. Soc. A* **1956**, *237*, 277–296.

9. Man, I. C.; Su, H. Y.; Calle-Vallejo, F.; Hansen, H. A.; Martínez, J. I.; Inoglu, N. G.; Kitchin, J.; Jaramillo, T. F.; Nørskov, J. K.; Rossmeisl, J., Universality in Oxygen Evolution Electrocatalysis on Oxide Surfaces. *ChemCatChem* **2011**, *3*, 1159–1165.